

ABSTRACT

Title of Dissertation: **MASTER EQUATION FORMULATIONS FOR
CONTINUOUS FEEDBACK IN QUANTUM SYSTEMS**

Guilherme de Sousa
Department of Physics,
Doctor of Philosophy, 2025.

Dissertation Directed by: **Professor Christopher Jarzynski
Department of Chemistry and Biochemistry,
Institute for Physical Science and Technology,
Department of Physics.**

In recent years, quantum experiments have become increasingly precise, fast, and capable of high resolution. Particular interest has been given to quantum control, which aims to prepare, manipulate, and steer quantum states toward desired outcomes. Common applications of quantum control include state preparation for quantum computing algorithms, protocols to implement nanoscale machines, and feedback to guide a system's evolution. Feedback involves collecting information from quantum measurements, then acting on the system based on measurement outcomes. The standard measurement model in quantum mechanics is the projective measurement, which destroys quantum coherence by causing the wave function to collapse to a subspace spanned by the eigenstates of the measured operator.

This thesis explores the theory of weak measurement processes, a class of measurement protocols that extract information from a quantum system while (partially) preserving coherence.

The weak measurement protocol has a tunable parameter that controls the information obtained per measurement cycle and the disturbance (decoherence) introduced into the quantum system. Using this nondestructive form of measurement, one can extract information during the system's evolution and apply real-time feedback to drive the system's evolution to specific target states. A general master equation is derived to describe continuous feedback using weak measurements with general filtering processing. Particular cases of low-pass and band-pass filters are studied in detail and applied to a harmonic oscillator cooling protocol. Results show that ground-state cooling of the quantum harmonic oscillator can be achieved.

Finally, this dissertation discusses an experimental and computational project that uses machine learning to estimate the temperature and the number of atoms of a cold atomic cloud. The goal is to use non-destructive measurements to infer hidden properties of the atomic ensemble without disturbing the atomic trap. Results show that reasonable accuracy can be achieved using various neural network architectures, depending on the complexity of the input data. The accuracy and responsiveness of the trained models make them suitable for real-time estimators that can be used in closed-loop feedback.

MASTER EQUATION FORMULATIONS FOR CONTINUOUS FEEDBACK
IN QUANTUM SYSTEMS

by

Guilherme de Sousa

Dissertation submitted to the Faculty of the Graduate School of the
University of Maryland, College Park in partial fulfillment
of the requirements for the degree of
Doctor of Philosophy
2025

Advisory Committee:

Professor Christopher Jarzynski, Chair/Advisor
Professor Ian Spielman, Co-Advisor
Professor Alicia Kollar
Professor Avik Dutt
Professor Ronald Walsworth, Dean's Representative

© Copyright by
Guilherme de Sousa
2025

Dedication

*Dedicated to my family,
and all my friends from
COTEL,
São Carlos, and
Maryland.*

Acknowledgments

“All we have to decide is what to do with the time that is given to us.” — Gandalf

First and foremost, I’d like to thank my advisor, Prof. Christopher Jarzynski, for giving me the incredible opportunity to work on amazing projects and for his constant support, guidance, and freedom to explore new ideas. After six years in my PhD program, I can say that Chris is one of the best advisors a student can have. Whenever I spoke with Chris or presented my research, he would always ask me a question that would make me learn or think of something new. I appreciate all the academic and career advice I received from him and the fantastic environment he creates in his group.

I would also like to thank my co-advisor, Prof. Ian Spielman. During these past two years working with Ian, I feel that I have been constantly learning something new. Every interaction has been a new opportunity to learn more about physics, statistics, programming, and good research practices. I also thank Dr. Justyna Zwolak for the constant guidance and insights in our computational projects.

A good portion of the projects in this thesis started during my participation in the FQxI Information as Fuel project. Thank you, Chris, for the opportunity to work in this research project. Thanks to my theory collaborators Björn Annby-Andersson, Debankur Bhattacharyya, Daniel Holst, Pharnam Bakhshinezhad, Patrick P. Potts, Peter Samuelsson, and Chris Jarzynski for everything that I learned from this interaction. I also thank the experimental groups of Klaus Ensslin

and Ville Maisi for the productive discussions we had along the way. I also thank all participants of the 2023 Obergurgl meeting for the insightful discussions, and the fruitful conversations I had with Björn during his visit to Maryland.

Next, I would like to thank all the members of the Jarzynski and Spielman groups with whom I have interacted during my PhD; your support has made these years more engaging and productive. Thanks to Debankur Bhattacharyya, Greeshma Oruganti, Long Him Cheung, Joshua Chiel, Natalia Ruiz-Pino, Anthony Munson, Twesh Upadhyaya, Wade Hodson, Sangyun Lee, Carlos Floyd, Saipriya Satyajit, Patrick Kelly, Michael Doris, Dario D'Amato, and Brady Egleston for the amazing discussions. A special thanks to Debankur, Greeshma, Natalia, Seho, Jiyeon, and many others for their friendship and the many meaningful conversations we have shared over the years. Everyone has made a significant contribution to my doctoral journey.

Finally, I acknowledge funding from Foundational Questions Institute, US National Science Foundation, John Templeton Foundation, and Institute for Robust Quantum Simulation, which supported my research during my PhD. I also want to express my gratitude to the University of Maryland for its resources and the excellent professors whose classes enriched my early years in the PhD program. A special thanks to Josiland Chambers, the Physics program coordinator, for her support and administrative guidance throughout my PhD.

I am deeply grateful to my family and friends for their unwavering support. I love you all.

Agradecimentos

“O que fazemos na vida ecoa na eternidade.” — Maximus Decimus Meridius

Em primeiro lugar quero agradecer minha mãe, meu pai e meu irmão por todo apoio. Não somente durante o doutorado, mas em todos os momentos da minha vida. Sempre foram vocês que me incentivaram, me ajudaram e se sacrificaram para que eu pudesse ter as melhores oportunidades. Um agradecimento especial para minha mãe que sempre acreditou em mim e me deu forças para continuar lutando mesmo quando não achei ser possível continuar. Esse título de doutorado não seria possível sem a ajuda de vocês. Amo vocês!

Meus avós, tios, tias, primos e primas também tem um lugar especial no meu coração. Obrigado por sempre acreditarem em mim e por todo carinho que recebo de vocês todas as vezes que nos encontramos. Mesmo longe tenho certeza que sempre estão torcendo por mim. Tenho muita sorte de ter nascido e sido criado numa família tão incrível, tudo que sou hoje vem de vocês.

Agradeço imensamente aos meus amigos que estão sempre ao meu lado e me dão forças pra continuar todos os dias. Um agradecimento especial ao Vítor, Andrei, Lucas e meu primo Gabriel por sempre me apoiarem e me ajudarem em todos os momentos. Seria simplesmente impossível chegar onde cheguei sem as conversas, risadas e momentos que compartilhamos ao longo dessas décadas que nos conhecemos. Agradeço também aos meus amigos do COTEL por todos esses anos de amizade e que possamos continuar compartilhando ótimos momentos

juntos. Meus amigos de São Carlos: Raquel, Rafael, Marcos e Luciano também fazem parte dessa trajetória. Muitas das experiências que vivi nos últimos anos foram com vocês e fico muito feliz por nossa amizade.

Por fim, agradeço por todas as oportunidades que a vida me deu e pela saúde que tenho. Apesar das dificuldades, viver é muito bom!

Table of Contents

Dedication	ii
Acknowledgements	iii
Agradecimientos	v
Table of Contents	vii
List of Publications	x
List of Figures	xi
List of Tables	xiv
List of Abbreviations	xv
Chapter 1: Introduction	1
1.1 History of quantum mechanics	1
1.2 Quantum measurements	4
1.2.1 The measurement problem	6
1.3 Quantum feedback	6
1.4 Evolution of quantum systems	9
1.4.1 Kets and operators	9
1.4.2 Born rule	11
1.4.3 Schrödinger equation	12
1.4.4 Density matrix formalism	13
1.5 Stochastic processes and stochastic calculus	16
1.5.1 Stochastic process	16
1.5.2 Wiener increments	17
1.5.3 Stochastic calculus	20
1.6 Summary of the chapters	21
Chapter 2: Quantum Fokker-Planck Master Equation	23
2.1 Overview	23
2.2 Weak measurements	25
2.3 Continuous measurement and Belavkin equation	29
2.4 Quantum Fokker-Planck Master Equation	32

2.5	Inertial model for a weak measurement	35
2.6	Harmonic model for weak measurement	39
2.6.1	Momentum measurement	42
2.6.2	Position measurement	47
2.7	Discussion and concluding remarks	51
Chapter 3: Continuous feedback protocols for cooling and trapping a quantum harmonic oscillator		53
3.1	Introduction	53
3.2	Model and QFPME	56
3.2.1	Classical model	56
3.2.2	Quantum model - cooling protocols	58
3.2.3	Quantum Fokker-Planck Master Equation	60
3.3	Results	63
3.3.1	Protocol X: position measurement	63
3.3.2	Protocol XP: position and momentum measurements	65
3.3.3	Protocol C: Cross feedback	68
3.3.4	Coupling to a thermal bath	70
3.4	Trajectory simulation	73
3.5	Discussion	77
3.6	Conclusion	78
3A	Feedback cooling in a classical oscillator	80
3A.1	Discrete time feedback	80
3A.2	Continuous feedback	81
3B	QFPME with multiple measurements	82
3C	Protocol X: Position Measurement	84
3D	Protocol XP: Position and Momentum Measurements	86
3E	Protocol C: Cross Feedback	88
3E.1	Position spreading	91
3F	Thermal coupling	92
3G	Trajectory simulation	93
Chapter 4: Quantum Fokker-Planck Master Equation with general filtering		96
4.1	Introduction	96
4.2	QFPME with multiple low-pass filters	97
4.3	QFPME with Band-pass filtering	100
4.4	QFPME with general filtering	102
4.4.1	General analytical filtering	102
4.4.2	General signals	104
4.5	Harmonic oscillator	104
4.5.1	One layer of filtering	105
4.5.2	Two layers of filtering	106
4.5.3	Three layers of filtering	108
4.5.4	Multiple layers of filtering	110
4.5.5	Band-pass filter	111

4.6	Discussion and concluding remarks	113
4A	Deriving the general QFPME	115
4B	Filtering for specific QFPMEs	118
4C	Cooling a quantum harmonic oscillator	120
Chapter 5:	Predicting temperature and atom number using machine learning	126
5.1	Introduction	127
5.2	Methods to estimate the velocity distribution of cold atoms	131
5.2.1	Formal solution using a thermal velocity distribution	133
5.2.2	Velocity kernel using deconvolution	138
5.2.3	Position dependent temperature distribution	141
5.2.4	Discussions and conclusions	144
5.3	Machine learning prediction pipeline	146
5.4	Experiment	148
5.5	Data collection	151
5.5.1	Labeling strategy	151
5.5.2	Data preprocessing	153
5.6	Machine Learning models	154
5.6.1	Optimization and training	156
5.7	Prediction results	157
5.8	Discussions	159
5.9	Conclusions	161
5A	Column density calculation	163
5B	Neural Network architectures	163
5B.1	Matrix Multiplication MM	164
5B.2	Multi-layer perception MLP	164
5B.3	Convolutional Neural Network CNN	164
Chapter 6:	Outlook and future directions	166
	Bibliography	168

List of Publications

[1] Björn Annby-Andersson, Faraj Bakhshinezhad, Debankur Bhattacharyya, **Guilherme De Sousa**, Christopher Jarzynski, Peter Samuelsson, and Patrick P. Potts. Quantum fokker-planck master equation for continuous feedback control. *Phys. Rev. Lett.*, 129:050401, Jul 2022

[2] Björn Annby-Andersson, Debankur Bhattacharyya, Pharnam Bakhshinezhad, Daniel Holst, **Guilherme De Sousa**, Christopher Jarzynski, Peter Samuelsson, and Patrick P. Potts. Maxwell’s demon across the quantum-to-classical transition. *Phys. Rev. Res.*, 6:043216, Nov 2024

[3] **Guilherme De Sousa**, Pharnam Bakhshinezhad, Björn Annby-Andersson, Peter Samuelsson, Patrick P. Potts, and Christopher Jarzynski. Continuous feedback protocols for cooling and trapping a quantum harmonic oscillator. *Phys. Rev. E*, 111:014152, Jan 2025

[4] **Guilherme De Sousa**, Dario D’Amato, Brady Egleston, Michael Doris, Justyna Zwolak, and Ian Spielman. Predicting temperature of an atomic cloud using machine learning. Manuscript in preparation

[5] **Guilherme De Sousa** and Christopher Jarzynski. Quantum fokker-planck master equation with general filter. Manuscript in preparation

[6] Daniel Schug, Sai Yerramreddy, Brady Egleston, **Guilherme De Sousa**, Rich Caruana, I. B. Spielman, Craig Greenberg, and Justyna P. Zwolak. Explainable machine learning for ultracold atoms image data. Manuscript in preparation

List of Figures

2.1	Schematics to represent the simplistic description of the SG experiment. A particle in a superposition state of the spin interacts with the magnetic field. The vertical displacement is proportional to the strength of the interaction and the spin. The detector measures two disjoint distributions representing the spin up and down.	26
2.2	Probability distribution (black dashed curve) of the measurement outcome in Eq. (2.11) for $\alpha = \beta$ and $p_z = 0$. The blue and orange curves correspond to the displacement of individual states $ \uparrow\rangle$ and $ \downarrow\rangle$ — see Fig. 2.1. A small momentum variance makes it easier to distinguish the spin in the post-measurement state. If the momentum variance is large, the distribution resembles a simple Gaussian distribution.	28
3.1	Illustration of Protocol X (defined in the next section). Cooling is achieved by measuring the position continuously and applying feedback by changing the location of the harmonic potential. The measurement outcome is a low-pass filtered version (red line) of the noisy weak measurement (light blue line).	55
3.2	Comparison of analytical formulas (dashed lines) to numerical results (circles). We chose $b = 1$ for Protocols X and XP for simplicity. The average asymptotic energy was calculated using 1000 runs of the stochastic equations for (a) Protocol X for different values of measurement strength. (b) Protocol XP for different values of measurement strength. Here, we can see that the energy only depends on the ratio γ/λ . The non-monotonic energy behavior as a function of γ/λ for both Protocols X and XP can be explained by the competition between the noise sources. See Sec. 3.4 for a detailed discussion. (c) Cross-feedback protocol, where we chose $\mu = 2\lambda/\omega$. Note that this plot illustrates that we need $\gamma \gg \omega \gg \lambda$ to achieve maximum cooling.	66
3.3	Single trajectory simulation for Protocol XP ($b = 1$). Here, we plot 5 trajectories (light blue lines) and the average energy for 2000 trajectories (blue line). The trajectory energy, in general, only converges with the analytical result (dashed line) in the ensemble sense. See Sec. 3.4 for simulation details. (a) Single trajectory simulation for Protocol XP with ground state cooling ($\gamma = 2\lambda$). The energy initially evolves stochastically, but after the variances have decayed to their asymptotic values, the energy evolution becomes deterministic, producing ground-state cooling at the trajectory level. (b) Here, the protocol applied is not at the ground-state condition ($\gamma \neq 2\lambda$). Note that the individual trajectories don't necessarily converge to a fixed energy value, but the ensemble average converges to the analytical result derived in Eq. (3.21).	73

4.1	a) Single-filter feedback scheme: the outcome of the continuous measurement is processed by a single component. The Hamiltonian directly uses the signal $D_1(t)$ to perform feedback $\hat{H} = \hat{H}(D_1(t))$; b) Multiple-filter feedback scheme: multiple components add finite bandwidths to the system, and the final feedback can use all signals to change the Hamiltonian $\hat{H} = \hat{H}(\mathbf{D}'(t))$	99
4.2	Phase diagram indicating which protocol is able to cool down the particle to the lowest energy for a given value of (γ, Ω) . Each region indicates which protocol yields the lowest energy using Eqs. (4.23,4.27,4.34). The vertical dashed lines indicate the transition regions where the second protocol is the coldest for $2\sqrt{2} < \gamma/\lambda < 4$, and where the third protocol is the coldest for $\gamma/\lambda > 4$ [see Eq. (4.37)].	109
4.3	Separation of timescale correction function α_n plotted for various values of γ^2/λ^2 . The mean value of the correction function for $N = 5000$ trajectories agrees with the analytical expressions in Eqs. (4.39,4.40) within statistical error (Standard Error of the Mean).	111
4.4	Asymptotic normalized energy for cooling a quantum harmonic oscillator using a band-pass filtering process. Equation (4.41) is plotted as a function of Ω/γ . For larger values of Ω/γ , the energy diverges and then takes unphysical values (not shown).	112
5.1	Atom absorbing and re-emeting a photon. a) The atom has initial velocity \vec{v} and the photon carries momentum $\hbar\vec{k}$. b) the atom absorbs the photon and goes to an excited state while changing its velocity by $\hbar\vec{k}/m$. c) after a decaying timescale, the atom re-emits the photon in a random direction and gets a new kick in momentum.	128
5.2	Comparison of non-Gaussian and Gaussian shaped clouds. The absorption images are taken after 1 ms – 5 ms of expansion. In the first row, we have the files 2024-02-05 group 0527; in the second row, we have the files 2024-02-04 group 0616. Non-ideal MOTs can expand as two (or more) separate clouds or retain their initial shape for longer times.	133
5.3	Gauss-Hermite fitting of the cloud expansion of the files 2024-02-05 group 0616. The first row contains the original cloud from 1 ms – 5 ms. The second row represents the reconstructed clouds based on the fitted parameters. The first column contains the predicted cloud at $t = 0$ and a heatmap with the absolute values of the Hermite coefficients, as defined in Eq. (5.17).	136
5.4	Gauss-Hermite fitting of the cloud expansion of the files 2024-02-03 group 1201. The first row contains the original cloud from 1 ms – 5 ms. The second row represents the reconstructed clouds based on the fitted parameters. The fitting was done with maximum degree of 5 for Hermite polynomials.	137
5.5	Evolution kernel for the clouds defined by the files 2024-02-05 group 0616. The first row is the input images of the cloud's expansion. The second row contains the kernels calculated using Eq. (5.25), and the third row is the reconstructed image calculated by convolving the initial distribution with the respective kernel.	139

5.6	Evolution kernel for the clouds defined by the files 2024-02-03 group 1201. The first row is the input images of the cloud's expansion. The second row contains the kernels calculated using Eq. (5.25), and the third row is the reconstructed image calculated by convolving the initial distribution with the respective kernel.	140
5.7	Workflow of the work. Data is generated (Sec. 5.4) in the experiment. Labels are calculated, and the images are preprocessed (Sec. 5.5). The models (Sec. 5.6) are trained, and the predictions are compared to the true values (Sec. 5.7).	146
5.8	Experimental apparatus for MOT preparation and image taking at Minilab (NIST Gaithersburg). 1) shows the science cell where the atomic cloud is prepared, 2) shows one of the cameras used for imaging, 3) shows part of the mirrors and lenses used to focus the laser beams on the MOT cell, and 4) shows the optical fibers that conduct the laser into the experiment.	148
5.9	Distribution of total fluorescence counts for e_x - (top) and e_z - (bottom) images. The dashed line represents the threshold used in each axis to determine if a group is assigned MOT = True.	152
5.10	Matrix representation of the weights learned by the MM model multiplied by the average fluorescence image on each set $\{\mathcal{S}_c, \mathcal{S}_f, \mathcal{S}_t\}$. For each set, on top, we have the weights times the e_x -fluorescence image, and on bottom, the weights times the e_z -fluorescence image. For each set, the plot on the left shows the evaluation capable of estimating temperature, and the plot on the right shows the evaluation that can estimate the number of atoms. Blue pixels correspond to positive values, red pixels to negative values, and white to zero.	160

List of Tables

3.1	Performance of different protocols under optimal conditions. The column Regime denotes the hierarchy resulting in optimal conditions. The column Timescale shows the relaxation rate to the asymptotic value. The column Energy represents the asymptotic energy achieved. The column Position Variance shows the variance obtained after trapping the particle. Note the special condition for ground-state cooling that can only be achieved by Protocol XP. The optimal choice for parameters to achieve near ground-state cooling are $b = 2\lambda/\gamma$ and $\mu = 2\lambda/\omega$. . .	75
5.1	Dataset labels. This table contains the labels derived from our classification and fitting processes.	147
5.2	Experimental parameters varied to create diverse MOT conditions.	149
5.3	Imaging parameters. This table describes the relevant information of our three imaging systems.	150
5.4	Summary table for the results of different architectures tested in different datasets. For brevity, we denote $\mathcal{E}_T\%$ as the average fractional error (in percentage) for temperature and $\mathcal{E}_N\%$ as the average fractional error (in percentage) for atom number. The numbers in parentheses show the most significant digit of the standard deviation.	158

List of Abbreviations

POVM	Positive Operator-Valued Measure
CPTP	Completely Positive and Trace Preserving
SG	Stern-Gerlach
OU	Ornstein-Uhlenbeck
QFPME	Quantum Fokker-Planck Master Equation
SDE	Stochastic Differential Equation
NIST	National Institute of Standards and Technology
BEC	Bose-Einstein condensate
MOT	Magneto-optical trap
AI	Artificial intelligence
ML	Machine learning
NN	Neural network
TOF	Time of flight
WD	Wiener deconvolution
SNR	Signal-to-Noise ratio
AOM	Acousto-Optical Modulator
CMOS	Complementary Metal Oxide Semiconductor
MM	Matrix multiplication
MLP	Multi-layer perception
CNN	Convolutional neural network

Chapter 1: Introduction

In this chapter, I introduce the key concepts discussed in this thesis. I start from a historical perspective about the main themes related to the thesis. Later, I discuss in detail the role of measurements in quantum theory and some of the open questions I try to answer in the following chapters. A brief overview of the quantum and stochastic formalisms used throughout the work is presented. Finally, the organization of the thesis is introduced.

1.1 History of quantum mechanics

Quantum mechanics is considered one of the most successful theories of nature. It started in the early 1900s with Planck, Einstein, Bohr, and others [7–9]. The accomplishments of the early quantum theory include understanding black body radiation (and the ultraviolet catastrophe), the explanation of the photoelectric effect, and the quantization of the hydrogen spectrum.

Soon after the early success, a more modern approach to quantum mechanics started to be consolidated by Schrödinger, Born, and Heisenberg [10–12]. At this point, the mathematical language was developed, and part of the notation we still use today was introduced. The solution of the quantized energy levels of the quantum harmonic oscillator was an important milestone in the development of the new theory. Later, a new quantum mechanics revolution started with what is today known as second quantization. This formalism extends quantum mechanics to many-

body systems and includes the role of statistics in the fundamental quantum theory. Researchers including Dirac, Fock, and Bose [13–15] led the way in studying collective phenomena in quantum systems. The inclusion of statistical rules in the quantum theory gave rise to the notion of fermions and bosons.

In the 1960s, important work carried out by Bell and others [16–18] elucidated surprising aspects of quantum probability theory. The idea is that measuring quantum entangled systems can yield results incompatible with the standard notions of classical probabilities. The notions of locality and classicality were solidified, and the Bell inequalities helped debunk the theory of hidden variables, which was developed to explain some of the non-intuitive consequences of quantum probabilities.

The 1980s and 1990s witnessed the emergence of modern atomic and laser physics [19–22]. The increased control and manipulation of atoms allowed experimentalists to trap and cool atoms to previously unimaginable levels. By the end of the 1990s, the first verification of the Bose-Einstein condensation (BEC) was reported in rubidium atoms [23, 24]. Since then, much progress has been made in cold atoms, from the precise measurement of time (which led to the development of atomic clocks) to the study of topology in many-body systems [25–30].

Various other important results in multiple fields of physics were obtained along the way, and this summary is not meant to represent an exhaustive list of accomplishments in the recent history of physics. In particular, special attention has been paid to quantum computation in the past two decades. Significant milestones in the realization of quantum qubits have been reached in recent years, particularly in the control and scaling of quantum systems [31–34]. The theory of quantum algorithms [35–37] also made important achievements, such as showing an exponential upside in performance that quantum computers can have compared to classical analogs. The

typical quantum algorithm runs by preparing a particular initial state, then applying a series of transformations that encode the steps of the computation, and at the end, performing some form of quantum measurements to collect the results. The ability to measure the quantum system and interact with the qubits plays an essential role in developing quantum computation technologies. This is one example of the increased interest in quantum measurements and the skill to interact with quantum systems precisely.

An even more recent field has emerged in the past ten years: quantum thermodynamics [38–40]. The goal in this field is to extend and investigate classical results of thermodynamics to the quantum realm. The main challenge is to connect results derived in the nineteenth century without any concept of microscopic constituents of matter to a modern physics framework that involves particles, wave functions, and operators. Concepts like energy conservation, entropy, trajectories, and the definitions of work and heat are still active research areas and open questions in the field [41–44]. Active research areas include applications such as designing quantum thermal machines and thermodynamic processes to harness quantum phenomena to boost batteries, energy production, computation, and information storage.

All these developments of more than a century made it possible to control quantum systems at the nanoscale or smaller, with temperatures colder than nanokelvin, to study processes that can last fractions of nanoseconds. In this thesis, I aim to present results related to quantum control and feedback. Discussing quantum measurement mechanisms and how to model such processes is necessary to understand quantum feedback and how one can improve the existing protocols to achieve such a level of control.

1.2 Quantum measurements

Much of the focus of quantum mechanics in the last century was on understanding how microscopic phenomena shape emergent classical behavior: the atomic spectral lines, the selection rules, the heat capacity of metals, the properties of superconductors, and many others. A parallel but related aspect of quantum theory is *quantum measurement*. The measurement process doesn't follow from the dynamical evolution described by Schrödinger's equation and enters the quantum theory in the form of Born's postulate [11].

Quantum mechanics is a fundamentally statistical theory. All experiments have measurements typically described by probability distributions rather than single outcomes, which is not due to the experimental uncertainties in the apparatus. Quantum theory predicts that systems can exist in multiple states simultaneously, which is very different from classical mechanics and our physical intuition. Thus, assigning a single value to a system's position, momentum, or energy is ill-defined. This strangeness of quantum theory motivated interpretations based on hidden variables that, in principle, would explain the outcomes deterministically. However, Bell's work showed that this idea would violate local causality [16–18], and experiments confirmed that quantum mechanical measurements are incompatible with this interpretation.

The counterintuitive effects in quantum mechanics came from our poor understanding of the quantum measurement process. The superposition property of quantum states and the consequences of the wave function collapse in Born's measurement framework motivated debates about interpretations of quantum mechanics. The Copenhagen and Many Worlds interpretations are some of the most prominent philosophical explanations of the theory. At the time, even special relativity clashed with quantum mechanics in the form of the famous Einstein–Podolsky–Rosen

(EPR) paradox [45]. The central idea of the question raised by EPR is that the wave function collapse could, in principle, communicate information faster than the speed of light, which would violate one of the fundamental postulates of special relativity.

Although the philosophical aspects of quantum mechanics are still debatable [46], the operational quantum mechanics blindly follows the postulate rules for measurements. Despite our lack of fundamental understanding, quantum measurements have gotten more attention in recent decades as the experiments are more precise and reliable than ever. A particular application that benefits from a deeper understanding of quantum measurements is quantum computing. The goal is to encode a particular task or calculation into the evolution of a quantum system and get the results at the end of the computation by measuring the system on a particular basis. The results are then processed through the measurement statistics.

Following this recent surge in interest in quantum measurements, this thesis aims to discuss some theoretical aspects of quantum measurements. A particular focus is given to weak and continuous measurements. The goal is to expand our theoretical framework by studying both the microscopic models of continuous measurements and applications of feedback. The master equation approach to the study of quantum measurements can help us understand the statistics of measurements and derive nontrivial results by looking at the moments of operators over an ensemble of realizations.

Using a mathematical and physical model written in terms of stochastic processes, I worked on a series of projects to describe generic quantum systems subject to measurements. The goal is not only to measure but also to be able to use the measurement outcomes to design protocols capable of applying feedback to the system. An ensemble master equation was derived in various forms to allow experimentalists to describe their experiments more realistically and have analyt-

ical tools capable of accurately predicting results. In the end, a parallel project is discussed, in which I worked on a real experiment to use information from nondestructive measurements of cold atoms to estimate physical parameters.

1.2.1 The measurement problem

The measurement problem [47, 48] describes the apparent inconsistency between the superposition principle of quantum mechanics and the classical realism of single outcome measurements. The evolution of quantum systems is described by the Schrödinger equation (see Sec. 1.4), while Born’s rule describes measurements [11]. The latter is a postulate and cannot be derived from Schrödinger’s formulation.

The modern interpretation of the measurement problem involves interactions between quantum systems and the surrounding environment (also quantum) [49, 50]. These interactions create apparently random phases between the states of the quantum system. Only a subset of states remains when these phases are summed up, creating classical realism. This process is called “Quantum Darwinism”, and the preferred states are called pointer states [51–53]. Recent work challenges some of the prevailing ideas on the emergence of classicality [54]. Quantum Darwinism is an active area of research, but it is beyond the scope of this dissertation.

1.3 Quantum feedback

Measurements and information are broad concepts that can be used in multiple ways. A measurement can be performed to learn about the properties of an unknown system, or the initial state can be characterized to decide which unitary to apply; a measurement at the end of the

protocol can be used to check the fidelity of the state preparation; intermediate measurements can be used to learn about the path of the system's evolution; or even information can be used in real time to change the system's evolution based on the system's state. The process of using information about the system to change some aspects of its dynamics is called *feedback* because one "feeds" part of the information "back" to the system, closing a loop of information. This section briefly discusses some of the most important advances in quantum feedback and how the present work is placed. This section is based on the reviews [55, 56].

We must first define the difference between *autonomous* and *non-autonomous* feedback. This distinction reflects the level of abstraction and modeling one wants to consider when describing a particular system. In this discussion, non-autonomous feedback is any modification in the system's dynamics controlled by an external agent. Such an agent is not modeled and is considered to follow particular rules defined in the feedback protocol. The details of the implementation of the feedback protocol are not considered, and a clear distinction between the system and the external agent control is made. On the other hand, an autonomous feedback system is a purely physical device capable of implementing a particular protocol based solely on the equations of motion of its constituents. Examples of autonomous feedback systems include the Huygens' governor (1780's), Feynman's ratchet-and-pawl, and memory-tape models [56–60]. In the remainder of the thesis, I focus on non-autonomous feedback with no explicit description or assumptions about the external agent that measures and controls the (quantum) system.

In classical systems, feedback is typically modeled using dynamical systems. Ordinary or stochastic systems of differential equations can describe those systems. A linear system can sometimes be used to model simpler cases. The goal of feedback is, in general, to alter the dynamics of the time evolution to accomplish a particular goal, e.g. to stabilize the state or to

make sure it follows a particular trajectory in state space. Common frameworks include frequency and time domain formulations, with particular emphasis on the Kalman filter [61] — an important algorithm widely used in control theory to estimate the unknown variable based on statistical inference.

Classical control systems also employ signal processing in their frameworks. A widely used model in this context is the PID controller – comprising *proportional* (P), *integral* (I), and *derivative* (D) gains. Here, the controller refers to a mechanism that determines the control signal applied to the system. The controller is the effective signal processing that transforms the output signal (or the error signal for stabilization) into feedback. Each term of the controller provides a different ingredient to the signal processing and can be used individually or altogether, depending on the system’s specific dynamics and performance requirements. The proportional gain responds to the instantaneous error, but can amplify high-frequency noise. The integral gain accumulates past error, offering long-term correction, but can lead to oscillatory or slow behavior. Finally, the derivative gain can be used to predict future error and damp oscillations, but it is sensitive to high-frequency components. In Sec. 4.4, a connection between the signal processing used in the quantum models and the PID controller is presented.

On the quantum side, feedback has also been developed over the years. The general principle is similar: one makes measurements on the quantum system and changes its dynamics based on the outcomes of those measurements. However, measurement generally changes the system’s state by creating decoherence on the measurement basis. This backaction divides quantum feedback protocols into two main categories: stroboscopic measurement and continuous measurements. The former consists of applying projective measurements in the system at specific instants in time [62–65] and, based on the outcomes, to apply feedback to achieve the desired

evolution. The latter, which is the focus of this thesis, consists of measuring the system continuously and applying feedback based on the measurement outcome signal [66–69].

Throughout most of this thesis, I focus on studying systems under continuous measurements and feedback. At the core of these discussions is the signal processing of the weak measurement outcome and conversion to a useful signal. Different processes to convert a physical signal to an experimentally motivated signal are considered and compared in particular toy model tasks.

1.4 Evolution of quantum systems

In the following sections, I describe the key physical and mathematical concepts necessary to understand the work presented in this thesis. In this section, I define the notation used to describe the evolution of quantum systems. It is based on the textbook literature of Refs. [36, 38, 70, 71].

A quantum system is any system that follows the evolution rules of quantum mechanics. At its core, quantum mechanics studies systems that obey “discretization” (quantization) rules. These systems can present complex phenomena such as superposition and entanglement. The quantum theory I focus on in this thesis is non-relativistic and is based on the existence of a state and a generator of the dynamics (time evolution).

1.4.1 Kets and operators

All physical states in quantum mechanics are vector states in a Hilbert space [71]. These vectors are called *kets* and denoted by $|\psi\rangle$. The only requirement for a vector to be a quantum

state is to have a unitary norm

$$\langle\psi|\psi\rangle = 1. \tag{1.1}$$

The vector $\langle\psi|$ is called *bra* state and is the dual of $|\psi\rangle$. Using the linear algebra properties of the Hilbert space, we can always write a quantum state as a linear combination of basis states. What is interesting is to note is that there are an infinite number of different bases that can be used to describe a vector space. Consequently, even if the quantum state is written as a single state on one basis, it will always be in a *superposition* (linear combination) of states on a different basis:

$$|\psi\rangle = \sum_n c_n |\phi_n\rangle = \sum_n d_n |\xi_n\rangle. \tag{1.2}$$

To describe physical quantities (like position, momentum, and energy), one needs to define an operator — here denoted by \hat{A} — that maps ket states to ket states (and bra states to bra states)

$$\hat{A}|\alpha\rangle = |\beta\rangle \longleftrightarrow \langle\alpha|\hat{A}^\dagger = \langle\beta|. \tag{1.3}$$

The notation \hat{A}^\dagger denotes the Hermitian conjugate of the operator. For physical quantities, $\hat{A} = \hat{A}^\dagger$.

Another important property of the physical operators I am interested in is that they all have an eigendecomposition of the form

$$\hat{A}|\alpha\rangle = \alpha|\alpha\rangle \iff \hat{A} = \sum_\alpha \alpha|\alpha\rangle\langle\alpha|. \tag{1.4}$$

Each element in the summation $|\alpha\rangle\langle\alpha|$ is an operator. In particular, it is the projection operator because it projects any state into the particular state $|\alpha\rangle$. Different operators have, in general,

different eigendecompositions in terms of different bases. This will be important later because if two operators don't share a common basis, a quantum state will necessarily be in a superposition in at least one of those operators.

One way to quantify if two operators share the same basis is to calculate their *commutator*

$$[\hat{A}, \hat{B}] \equiv \hat{A}\hat{B} - \hat{B}\hat{A}. \quad (1.5)$$

If the result is the null operator, then \hat{A} and \hat{B} can be diagonalized simultaneously and share a common basis. An important case is the *canonical commutation relation* between position and momentum

$$[\hat{x}, \hat{p}] = i\hbar. \quad (1.6)$$

An important consequence of this result is that a quantum state cannot be simultaneously diagonalized in position and momentum basis.

1.4.2 Born rule

Before introducing the time evolution described by Schrödinger's equation, I describe the measurement procedure defined by Born. First, note that a measurement involves a particular operator. The goal is to find which state of the operator [one of its eigenstates, as defined in Eq. (1.4)] best represents the quantum state.

The linear combination property of the quantum states tells us that our system can be in multiple states of the measured operator at the same time. This implies that the Born measurement protocol has to be a statistical process that maps the quantum state into one of the states of

the measured operator. This process is random, and each measured operator's eigenstate has a particular probability of being selected. This probability, per Born's postulate, is given by the absolute value square of the projection of the quantum state into the basis spanned by the eigenstates of the operator

$$\hat{A} = \sum \alpha_n |\alpha_n\rangle\langle\alpha_n|, \quad (1.7)$$

$$P(\alpha_n) = |\langle\alpha_n|\psi\rangle|^2 = \langle\alpha_n|\psi\rangle\langle\psi|\alpha_n\rangle. \quad (1.8)$$

After the first measurement, subsequent measurements always yield the same result (assuming no time evolution happens). To describe this change in the system's state, we can write the following mapping

$$|\psi\rangle \rightarrow |\psi\rangle_{\text{meas}} = \frac{|\alpha_n\rangle\langle\alpha_n|\psi\rangle}{\sqrt{|\langle\alpha_n|\psi\rangle|^2}} = |\alpha_n\rangle. \quad (1.9)$$

The second equality is true because one can redefine the quantum state by absorbing an overall complex phase.

Using the probability defined in Eq. (1.8), one can calculate any moment of the distribution of measured outcomes, in particular, the average value of the operator \hat{A} is defined as

$$\langle\hat{A}\rangle = \sum_n \alpha_n P(\alpha_n) = \langle\psi|\sum_n \alpha_n |\alpha_n\rangle\langle\alpha_n|\psi\rangle = \langle\psi|\hat{A}|\psi\rangle. \quad (1.10)$$

1.4.3 Schrödinger equation

The Schrödinger equation describes the evolution of isolated quantum systems. The generator of the evolution is the Hamiltonian \hat{H} . Let $|\psi(t)\rangle$ denote the quantum state at time t . The

state of the system obeys

$$\partial_t |\psi(t)\rangle = \frac{-i}{\hbar} \hat{H} |\psi(t)\rangle. \quad (1.11)$$

In the case of a time-independent Hamiltonian, the solution of Schrödinger equation (1.11) is

$$|\psi(t)\rangle = e^{-it\hat{H}/\hbar} |\psi(0)\rangle, \quad (1.12)$$

where $|\psi(0)\rangle$ denotes the initial condition. One can write the same solution on the energy basis, i.e. the basis that diagonalizes the Hamiltonian:

$$\hat{H} |\phi_n\rangle = E_n |\phi_n\rangle, \quad (1.13)$$

$$|\psi(0)\rangle = \sum c_n |\phi_n\rangle, \quad (1.14)$$

$$|\psi(t)\rangle = \sum e^{-itE_n/\hbar} c_n |\phi_n\rangle. \quad (1.15)$$

In the energy basis, the quantum system's state evolves by acquiring complex phases that depend on the energy of the eigenstate.

1.4.4 Density matrix formalism

The final ingredient to describe the quantum system evolution is introducing the density matrix formalism. At first, one can define the density matrix operator using

$$\hat{\rho} \equiv |\psi\rangle\langle\psi|. \quad (1.16)$$

Now, the normalization property in Eq. (1.1) translates to a trace property

$$\text{tr}\{\hat{\rho}\} = 1. \quad (1.17)$$

So far, this operator describes the state of a pure quantum state. But, one can also describe a statistical mixture of different quantum states. Imagine the following density matrix

$$\hat{\rho} = \sum_n p_n |\psi_n\rangle\langle\psi_n|, \quad \sum_n p_n = 1, \quad p_n \geq 0 \forall n, \quad \langle\psi_n|\psi_n\rangle = 1 \forall n. \quad (1.18)$$

This operator still satisfies the normalization condition in Eq. (1.17), but now each quantum state is weighted by a particular probability p_n . This general framework can describe quantum states and probability distributions in the usual statistical sense. The property that can be used to tell if a density matrix describes a statistical ensemble or a single quantum state is called *purity*:

$$\begin{cases} \text{tr}\{\hat{\rho}^2\} = 1 : \text{pure state} \\ \text{tr}\{\hat{\rho}^2\} < 1 : \text{statistical mixture} \end{cases} \quad (1.19)$$

The density matrix version of the Born rule can be written as

$$\hat{\rho} \rightarrow \hat{\rho}_{\text{meas}} = \frac{\Pi_\phi \hat{\rho} \Pi_\phi^\dagger}{\text{tr}\{\Pi_\phi \hat{\rho} \Pi_\phi^\dagger\}}, \quad (1.20)$$

where $\Pi_\phi = |\phi\rangle\langle\phi|$ is a projection operator into the space spanned by the state $|\phi\rangle$ (it is also possible to project a state into a multidimensional subspace). As it will be important in Chapter 2,

one can generalize the Born rule to the case of non-projective measurements:

$$\hat{\rho} \rightarrow \hat{\rho}_{\text{meas}} = \frac{\hat{M}_z \hat{\rho} \hat{M}_z^\dagger}{\text{tr}\{\hat{M}_z^\dagger \hat{M}_z \hat{\rho}\}}, \quad (1.21)$$

that satisfy

$$\sum_z \hat{M}_z^\dagger \hat{M}_z = \hat{1} \quad (\text{identity operator}). \quad (1.22)$$

Here, z represents the measurement outcome, and the summation can be replaced by an integral in the continuous variable case. The set of operators $\{\hat{M}_z\}$ are called Positive Operator-Valued Measure (POVM) [36, 72].

Similarly, one can modify Schrödinger's equation to work in the density matrix formalism

$$\partial_t \hat{\rho} = \frac{-i}{\hbar} [\hat{H}, \hat{\rho}]. \quad (1.23)$$

Using the density matrix, it is possible to generalize the time evolution to account for dissipation due to the interaction with the environment (in the weak-coupling limit). In this case, one has the Lindblad master equation [73, 74]

$$\partial_t \hat{\rho} = \frac{-i}{\hbar} [\hat{H}, \hat{\rho}] + \sum_n \lambda_n \left(\hat{c}_n \hat{\rho} \hat{c}_n^\dagger - \frac{1}{2} \hat{c}_n^\dagger \hat{c}_n \hat{\rho} - \frac{1}{2} \hat{\rho} \hat{c}_n^\dagger \hat{c}_n \right). \quad (1.24)$$

Here, \hat{c}_n represents operators that can model transitions assisted by an external environment or decoherence caused by the interaction with the bath. As the system evolves under the Lindblad master equation, its purity decreases as the system gets more and more mixed.

1.5 Stochastic processes and stochastic calculus

In this section, I introduce the key concepts of classical stochastic processes and stochastic calculus. Using physics rigor and notation, I discuss the essential stochastic variables used in the following chapters. This section is based on Refs. [38, 68, 69, 75, 76].

1.5.1 Stochastic process

Stochastic processes are ubiquitous in mathematical fields. They allow us to describe complicated underlying processes using random variables that obey simple rules. For this discussion, let's denote a stochastic process as a collection (or sequence) of random variables by $\{X_i\} \equiv \{X_1, \dots, X_n\}$. These variables can be drawn from arbitrary distributions that may include correlations. However, for this work, consider that all stochastic random variables are iid (independent and identically distributed), i.e. all variables X_i have the same ensemble statistics.

The individual random variables X_i can be discrete or continuous. A discrete variable can only assume one of countable symbols, e.g. $X_i = \{0, 1, \dots\}$ or $X_i = \{\text{heads}, \text{tails}\}$. To each possible outcome, one can assign an event probability. This probability is, intuitively, a relative frequency of a particular outcome when the number of samples is large. The sum of probabilities of all possible outcomes is normalized

$$P(X) \geq 0, \tag{1.25}$$

$$\sum_X P(X) = 1. \tag{1.26}$$

For a continuous variable, X is drawn from an uncountable set, typically an interval from

the real line. In this case, the meaning of the probability of a particular outcome is less clear, and one usually defines a probability density as the probability of drawing a value in an infinitesimal interval

$$P(x \in [X, X + dX]) = f(X)dX \geq 0, \quad (1.27)$$

$$\int dx f(x) = 1. \quad (1.28)$$

Here, $f(X)$ is the probability density normalized similarly to a probability distribution for discrete variables.

Throughout this thesis, I focus on a particular continuous probability distribution, the Gaussian distribution. Variables drawn from this distribution have statistics that are completely described by two real parameters: mean and variance. The probability density function for the Gaussian (or Normal) distribution is given by

$$f(x) = \frac{1}{\sqrt{2\pi\sigma^2}} e^{-(x-\mu)^2/2\sigma^2}. \quad (1.29)$$

The mean is μ , and the variance (standard deviation) is σ^2 (σ).

1.5.2 Wiener increments

Another important random process that is widely used in this thesis is the Wiener increment. To define it, let's consider the following Gaussian distribution with zero mean and variance equal to the time t ,

$$f(W) = \frac{1}{\sqrt{2\pi t}} e^{-W^2/2t}. \quad (1.30)$$

The variables $W(t)$ drawn from this distribution are called *Wiener process*. Now consider another process, called the *Wiener increment*:

$$\delta W \equiv W(t + \delta t) - W(t). \quad (1.31)$$

The variable $W(t + \delta t)$ have zero mean and variance equal to $t + \delta t$. Using the nice properties of a sum of Gaussian variables, one can verify that the increment of δW is described by the following probability distribution

$$f(\delta W) = \frac{1}{\sqrt{2\pi\delta t}} e^{-\delta W^2/2\delta t} \quad (1.32)$$

Consider the sum of the squares of multiple Wiener increments,

$$S_N = \sum_{n=1}^N \delta W_n^2, \quad (1.33)$$

where $N = t/\delta t$ and δW_n denotes the n 'th Wiener increment. The average and variance of S_N are, respectively,

$$\langle S_N \rangle = N\delta t = t, \quad (1.34)$$

$$\langle S_N^2 \rangle = N \cdot 3\delta t^2 + (N^2 - N)\delta t^2, \quad (1.35)$$

$$\langle S_N^2 \rangle - \langle S_N \rangle^2 = 2N\delta t^2 = \frac{2t^2}{N}. \quad (1.36)$$

In the limit $N \rightarrow \infty$ with t fixed, one gets $\text{var}(S_N) \rightarrow 0$, indicating that S_N behaves like a

deterministic variable. In this limit, one can interpret S_N in the integration sense

$$t = S_N = \int_0^t dt = \int_0^t dW^2, \quad (1.37)$$

from which one gets the result

$$dW^2 = dt. \quad (1.38)$$

The integration of the square of Wiener increments behaves like a deterministic variable. A similar analysis can be done to show that, for independent increments

$$dW_i dW_j = 0. \quad (1.39)$$

From now on, the defining properties of the Wiener increments can be summarized as follows

$$\langle dW_i \rangle = 0, \quad (1.40a)$$

$$dW_i dW_j = \delta_{ij} dt. \quad (1.40b)$$

As will be clearer in the next section, the Wiener increment dW can be intuitively interpreted to be proportional to \sqrt{dt} . Thus, to account for expansions that are correct up to the first order in dt , one needs to keep track of terms dW up to the second order.

1.5.3 Stochastic calculus

The previous section hinted that one can intuitively interpret the Wiener increments as the order of \sqrt{dt} . This idea is useful when considering stochastic differential equations (SDE), i.e., infinitesimal updates describing the evolution of a particular process that can depend on random variables.

Let's consider a physical process that is described by the following SDE:

$$dX = \alpha(X, t) dt + \beta(X, t) dW. \quad (1.41)$$

Particular cases of Eq. (1.41) are used to describe important processes like the Brownian particle and the Ornstein-Uhlenbeck (OU) process [75]. The integral solution for this process is given by

$$X(t) = X_0 + \int_0^t dt' \alpha[X(t'), t'] + \int_0^t dW(t') \beta[X(t'), t'], \quad (1.42)$$

and can be numerically evaluated using the Cauchy-Euler method [75]. Although this solution looks similar to what one would expect from usual calculus, the stochastic updates make it necessary to modify the chain and the change-of-variables rules to include a second-order effect from stochastic updates:

$$d(fg) = (df)g + f(dg) + (df)(dg), \quad (1.43)$$

$$df(x) = f'(X) dX + \frac{1}{2} f''(X) (dX)^2, \quad (1.44)$$

These are Itô formulas that allow us to operationally work with stochastic differential equations.

Most of the results presented in this thesis depend on the use of these rules.

1.6 Summary of the chapters

All chapters of this thesis correspond to work performed in collaboration with others; the people involved in each project are mentioned at the beginning of each chapter. Chapters 2, 3, and 4 are related to various master equation formulations of continuous feedback in quantum systems; Refs. [57, 77, 78] deal with similar topics. Chapter 5 discusses a project developed at the laboratory of Prof. Ian Spielman, whose goal is to use nondestructive measurements to infer the physical properties of cold atoms using machine learning.

Chapter 2: This introductory chapter discusses the weak measurement formulation using Gaussian ancilla states. Continuous measurements are defined in the proper limit of weak but frequent measurements, whose outcomes are described by Gaussian white noise. Continuous measurements are used to reproduce the derivation of the Quantum Fokker-Planck Master Equation (QFPME) found in Ref. [1]. Finally, more general models are derived for continuous stochastic Schrödinger equations using massive and harmonic interaction ancillas.

Chapter 3: This chapter is based on published work [3]. Here, I apply the QFPME to a particular analytically solvable toy model. The goal is to use measurement and feedback to cool and trap a quantum harmonic oscillator. Three protocols are defined, and the QFPME is extended to allow multiple continuous measurements. It is possible to show that trapping and cooling are achievable for a suitable choice of parameters, and ground-state cooling is achievable when measuring position and momentum simultaneously.

Chapter 4: This work is based on unpublished work [5] that extends the results derived in

the previous chapters. The goal is to generalize the filtering operation introduced in Ref. [1] to include other forms of signal processing. Using the harmonic oscillator cooling as a toy model, analytical results are derived and discussed.

Chapter 5: This chapter aims to use machine learning to calculate the temperature and the number of atoms of a trapped atomic cloud using in-situ measurements. The first part of the chapter presents theoretical and numerical methods to estimate the velocity distribution of a sequence of expanding atomic clouds. These clouds experience ballistic expansion and are modeled using a simple convolution rule. Various approaches to calculate the velocity kernel are discussed in order of increasing complexity. The second part of the chapter describes the experiment, the data collection, and the training of various machine learning models with increasing complexity. The results confirm that machine learning can predict the temperature and number of atoms without using information from the release and expansion of the atoms.

Chapter 6: The final chapter presents this thesis's outlook and mentions future work directions.

Chapter 2: Quantum Fokker-Planck Master Equation

This chapter is based primarily on work done with Björn Annby-Andersson, Debankur Bhattacharyya, Pharnam Bakhshinezhad, Christopher Jarzynski, Peter Samuelsson, and Patrick P. Potts, which has been published in the article “Quantum Fokker-Planck Master Equation for Continuous Feedback Control” [1] (Phys. Rev. Lett. **129**, 050401). My contribution to this published work was mainly in deriving the separation of timescale results presented in the Supplemental Material, which I did together with Debankur Bhattacharyya.

In this chapter, I present a physical motivation to introduce the weak measurement POVMs used in deriving the results of Ref. [1]. More general forms of weak measurements are also discussed, particularly a model that can be used to derive the filtered signal from a microscopically starting point.

2.1 Overview

In classical mechanics, measurements are typically taken for granted, and all the properties of the system (like position, momentum, and energy) can be known simultaneously and with absolute precision (in principle). However, in quantum mechanics, systems can be in superposition states, and different operators may not be measured simultaneously. These features cause measurement in quantum mechanics to be a probabilistic process.

The evolution of an isolated quantum state is deterministic, and it is described by the unitary evolution generated by the Hamiltonian (in the Schrödinger picture [71] description). However, a typical quantum state is described by a superposition of different eigenstates of physical operators (like position, momentum, and energy). This superposition creates a situation where the state’s property, like its energy, is not well defined because it has different values simultaneously. In these situations, measurement is not a trivial process in quantum mechanics.

The black box approach to quantum measurement is given by Born’s rule [11], which gives us the statistical interpretation of quantum mechanics [38, 70]. This rule tells us that a measurement has many possible outcomes, and the probability of each outcome is related to the absolute value of the quantum state with respect to a particular eigenstate of the operator being measured. This measurement process is sometimes called “quantum state collapse” and is usually thought to be instantaneous, described in Sec. 1.4.

Generalized measurement schemes can be studied using completely positive and trace preserving (CPTP) maps, Kraus operators and POVMs [36, 38, 72, 79]. These measurement operators and schemes are typically derived from microscopical models in which two quantum systems — a primary system, and an auxiliary system— interact, and a projective measurement is performed on the auxiliary (or pointer) system. In this context, weak measurements were introduced to represent measurements that don’t cause the primary system’s quantum state collapse, and a smaller disturbance is imprinted into that system.

This chapter aims to introduce weak measurements using a physically intuitive model and then generalize to more sophisticated scenarios. Weak measurements are also the foundation of *continuous measurement* and *feedback* [68, 80–83]. The goal is to combine all these ingredients and describe the steps of the derivation of the Quantum Fokker-Planck Master Equation [1].

2.2 Weak measurements

The simplest and most commonly used interaction model for a weak measurement is the *impulsive interaction model* [68, 84]. This model can be discussed in the context of the well-known Stern-Gerlach (SG) experiment [71, 72, 85]. I will describe this model in detail here.

Consider a particle with two degrees of freedom: its position z and its spin degrees of freedom (up and down). Suppose the initial wavefunction of the particle can be described by

$$|\Psi_0\rangle = |\psi_z\rangle |\phi_s\rangle, \quad (2.1)$$

where $|\psi_z\rangle$ describes the wavefunction in position (z) degree of freedom and $|\phi_s\rangle$ describes the spin state of the particle. I omit the tensor product notation between the different degrees of freedom for simplicity. Also, consider the wavefunction in the momentum degree of freedom to be a Gaussian:

$$\langle p|\psi_z\rangle = \psi_z(p) = \left(\frac{k}{\pi}\right)^{1/4} e^{-k(p-p_z)^2/2}. \quad (2.2)$$

Here, $1/k$ controls the momentum variance of the wavefunction, and p_z is the average momentum in the z direction. The state of the spin is arbitrary and denoted by:

$$|\phi_s\rangle = \alpha |\uparrow\rangle + \beta |\downarrow\rangle. \quad (2.3)$$

Our goal is to make a measurement to characterize this arbitrary state. The measurement will be performed in the momentum degrees of freedom. Since the initial state for $|\psi_z\rangle$ is Gaussian, I

will refer to momentum as a Gaussian auxiliary system.

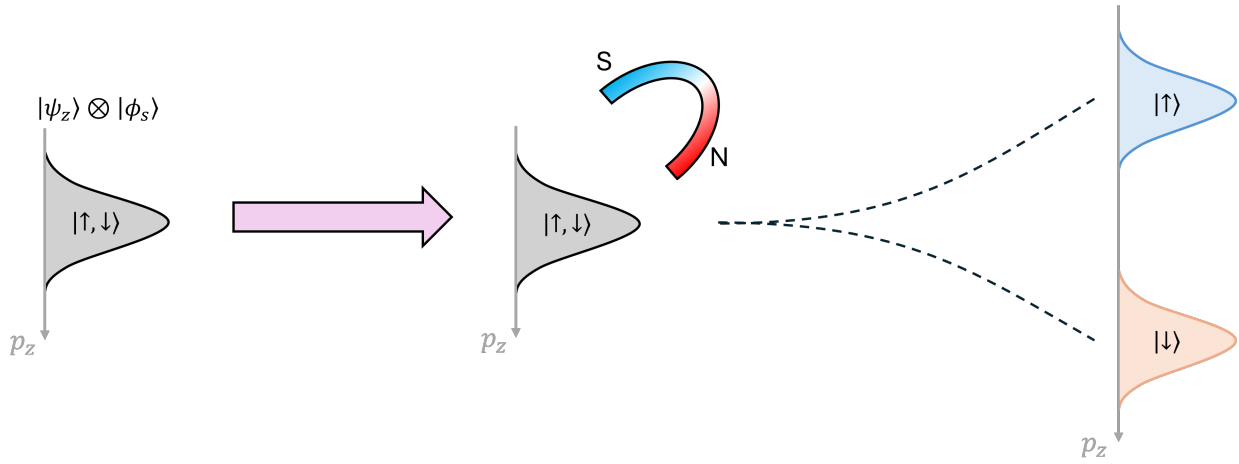


Figure 2.1: Schematics to represent the simplistic description of the SG experiment. A particle in a superposition state of the spin interacts with the magnetic field. The vertical displacement is proportional to the strength of the interaction and the spin. The detector measures two disjoint distributions representing the spin up and down.

The particle is in the presence of a magnetic field, and they interact due to the particle's magnetic moment (the spin). See Fig. 2.1. This interaction can be modeled by the interaction Hamiltonian

$$\hat{H}_I = -\vec{\sigma} \cdot \vec{B}, \quad (2.4)$$

where $\vec{\sigma}$ is the spin operator that acts on the spin degrees of freedom and \vec{B} is the magnetic field.

The magnetic field is created with a constant gradient in the z direction:

$$\vec{B} = \kappa \vec{z}, \quad \kappa = \text{constant}. \quad (2.5)$$

From Maxwell's equations, the magnetic field is divergence-free, $\vec{\nabla} \cdot \vec{B} = 0$. Thus, the magnetic field in Eq. (2.5) is not valid. However, the discussion here focuses on the evolution of the wavefunction and measurement, not the exact physics of the SG experiment.

The total Hamiltonian of this system is given by

$$\hat{H} = \frac{\hat{p}^2}{2m} - \vec{\sigma} \cdot \vec{B}, \quad (2.6)$$

where \hat{p} is the momentum operator of the particle. However, for the present discussion, it is instructive to disconsider the kinetic energy and focus on the interaction Hamiltonian. This simplification can also be thought of as the limit where the particle's mass is very large $m \rightarrow \infty$. In the next section, I will describe in detail the effect of finite inertia in this model.

In this approximation, the evolution of the system can be solved directly using the unitary operator for the interaction Hamiltonian in Eq. (2.4) ($\hbar = 1$):

$$\hat{U}(t) = e^{-i\hat{H}t} = e^{i\kappa\sigma_z\hat{z}t} = e^{i\kappa\hat{z}t} |\uparrow\rangle\langle\uparrow| + e^{-i\kappa\hat{z}t} |\downarrow\rangle\langle\downarrow|. \quad (2.7)$$

The time evolution operator behaves differently for each value of the spin component. This behavior causes the change in the wavefunction to be coupled to the spin degrees of freedom. Thus, by measuring the wavefunction we can get information about the spin. The state of the system at time t is

$$|\Psi_t\rangle = \hat{U}(t) |\Psi_0\rangle = \int dp |p\rangle [\alpha\psi_z(p - \kappa t) |\uparrow\rangle + \beta\psi_z(p + \kappa t) |\downarrow\rangle]. \quad (2.8)$$

Note that the wavefunction in momentum space gets displaced by an amount equal to κt , which is the same term in the exponent of Eq. (2.4).

Once the system interacts with the magnetic field and momentum and spin are coupled, we can measure momentum to get information about the system's state. Using Born's rule, we can

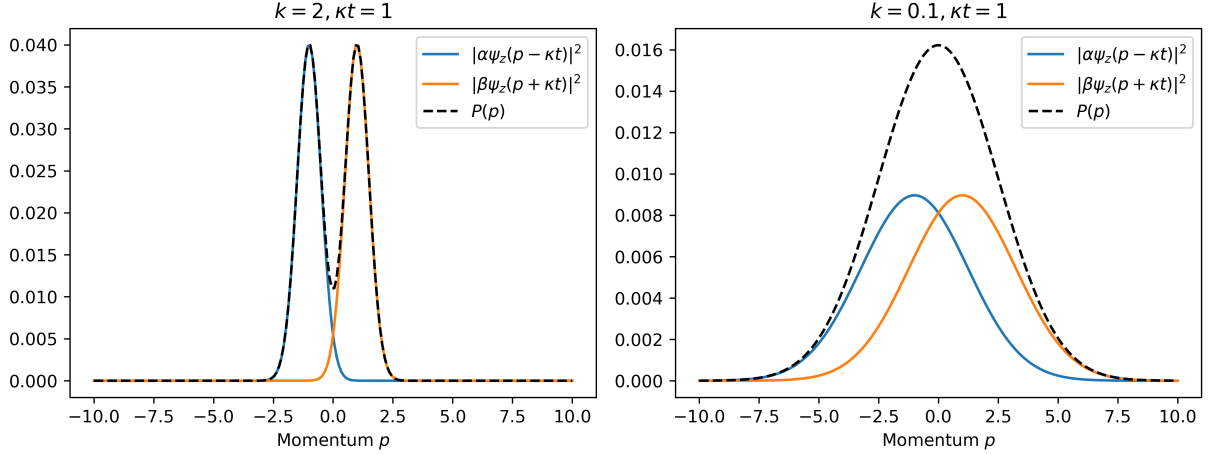


Figure 2.2: Probability distribution (black dashed curve) of the measurement outcome in Eq. (2.11) for $\alpha = \beta$ and $p_z = 0$. The blue and orange curves correspond to the displacement of individual states $|\uparrow\rangle$ and $|\downarrow\rangle$ — see Fig. 2.1. A small momentum variance makes it easier to distinguish the spin in the post-measurement state. If the momentum variance is large, the distribution resembles a simple Gaussian distribution.

calculate the state of the entire system if the momentum gets measured to be in state $|p\rangle$:

$$|\Psi_t\rangle_{\text{meas}} = \frac{|p\rangle \langle p|\Psi_t\rangle}{\sqrt{\langle \Psi_t|p\rangle \langle p|\Psi_t\rangle}}, \quad (2.9)$$

$$|\Psi_t\rangle_{\text{meas}} = |p\rangle \frac{[\alpha\psi_z(p - \kappa t)|\uparrow\rangle + \beta\psi_z(p + \kappa t)|\downarrow\rangle]}{\sqrt{|\alpha\psi_z(p - \kappa t)|^2 + |\beta\psi_z(p + \kappa t)|^2}}. \quad (2.10)$$

The probability distribution of the outcome p is given by

$$P(p) = |\alpha\psi_z(p - \kappa t)|^2 + |\beta\psi_z(p + \kappa t)|^2. \quad (2.11)$$

The framework described here is different from the usual SG experiment. For simplicity, I measure the system in the momentum basis, but a similar discussion can be made by measuring on a position basis (as in the original experiment). One needs to account for the time necessary for the position to be affected by the change in momentum. A related discussion is presented in

Sec. 2.6, where I compare position and momentum measurements.

The measurement outcome distribution is a weighted sum of two Gaussian distributions. The probability of the spin state gives the weights. Figure 2.2 shows the momentum distribution for $\alpha = \beta$ and $p_z = 0$. It is intuitive to see that for

$$\frac{k}{\kappa t} \gg 1, \quad (2.12)$$

the measurement is strong, and the post-selection state given by Eq. (2.10) collapses the state into one of the eigenstates of $\hat{\sigma}_z$. In the other limit ($k/\kappa t \ll 1$), the measurement is weak, the system's state is almost unaffected, and the distribution of p is close to a single Gaussian.

As will be more apparent in the next section, Eq. (2.10) is equivalent to a POVM. One can start the model directly using the POVM. Still, the previous construction can give a physical meaning/intuition as to why a particular model can describe a real-world process.

2.3 Continuous measurement and Belavkin equation

This section focuses on deriving the Belavkin equation [66, 67, 69, 84, 86–88], which is the stochastic master equation for continuous measured systems, and it is based on the review article [69]. The setup is similar to the previous section: the system is measured on the basis of a generic operator $\hat{A} = \sum_a \xi_a |\xi_a\rangle\langle\xi_a|$ using a Gaussian auxiliary system (similar to the previous section). The post-selection on the auxiliary system is equivalent to the Gaussian POVM (see Sec. 1.4.4):

$$\hat{M}(z) = \left(\frac{2\lambda\delta t}{\pi} \right)^{1/4} e^{-\lambda\delta t(z-\hat{A})^2}. \quad (2.13)$$

The parameter λ controls the strength of the measurement, δt is the interaction duration, and z is the measurement outcome. The measurement is fully described by the post-measurement state $\hat{\rho}_{\text{meas}}$ and the probability distribution of the outcome variable z :

$$\hat{\rho}_{\text{meas}} = \frac{\hat{M}(z)\hat{\rho}\hat{M}^\dagger(z)}{\text{Tr}\{\hat{M}(z)\hat{\rho}\hat{M}^\dagger(z)\}}, \quad (2.14)$$

$$P(z) = \left(\frac{2\lambda\delta t}{\pi}\right)^{1/2} \sum_a e^{-2\lambda\delta t(z-\xi_a)^2} \langle \xi_a | \hat{\rho} | \xi_a \rangle. \quad (2.15)$$

Now note that the first two moments of the measurement outcome z can be calculated directly from Eq. (2.15):

$$\langle z^n \rangle = \int dz z^n P(z) \quad (2.16)$$

$$\langle z \rangle = \langle \hat{A} \rangle = \text{Tr}\{\hat{A}\hat{\rho}\} \quad (2.17)$$

$$\langle z^2 \rangle = \langle \hat{A}^2 \rangle + \frac{1}{4\lambda\delta t} \quad (2.18)$$

In the limit of a weak measurement, $\delta t \rightarrow 0$, the distribution in Eq. (2.15) can be approximated by a single Gaussian distribution centered at the average value of the measured operator [69]

$$P(z) = \left(\frac{2\lambda\delta t}{\pi}\right)^{1/2} e^{-2\lambda\delta t(z-\langle \hat{A} \rangle)^2}. \quad (2.19)$$

Consequently, the variable z can be written as a Gaussian variable of the form

$$z = \langle \hat{A} \rangle + \frac{\delta W}{\sqrt{4\lambda\delta t}}, \quad (2.20)$$

where δW is a Gaussian variable satisfying $\langle \delta W \rangle = 0$ and $\text{var}(\delta W) = \delta t$. This is, so far, a single weak measurement; to construct a continuous measurement, one can consider the consecutive interactions of the quantum system with a Gaussian auxiliary ancilla [69]. For simplicity, the state of the auxiliary system is considered to be reset before every new interaction, which is a standard procedure in the study of collision or repeated interaction models [89–92].

The continuous measurement has a finite effect in the limit where small time steps become infinitesimal $\delta t \rightarrow dt$ and the auxiliary system is reset every time step dt (for the remainder, δt is used for small time steps and dt is used for infinitesimal steps). In this limit, the Gaussian variable $\delta W \rightarrow dW$ is mapped to a Weiner increment, which satisfies Eq. (1.40). Because the stochastic variable is effectively at the order of $dW \sim dt^{1/2}$, one needs to keep track of dW up to second order and dt up to first order to account for the stochastic effects in the system correctly (see Sec. 1.5.2).

To account for the underlying time evolution and the continuous measurement, the density matrix is updated using the following equation:

$$\hat{\rho}(t + dt) = e^{\mathcal{L}dt} \frac{\hat{M}(z)\hat{\rho}\hat{M}^\dagger(z)}{\text{Tr}\{\hat{M}(z)\hat{\rho}\hat{M}^\dagger(z)\}}, \quad (2.21)$$

where \mathcal{L} is the Liouville operator that evolves the quantum system in time. The master equation associated with the infinitesimal evolution of Eq. (2.21) can be calculated after expanding it up to first order in dt (second order in dW). The Belavkin equation gives the stochastic master equation that describes a quantum system under continuous measurement [69, 88]:

$$d\hat{\rho} = \mathcal{L}\hat{\rho}dt + \lambda dt \mathcal{D}[\hat{A}]\hat{\rho} + \sqrt{\lambda} dW \left\{ \hat{A} - \langle \hat{A} \rangle, \hat{\rho} \right\}. \quad (2.22)$$

Here $\mathcal{D}[\hat{c}]\hat{\rho} = \hat{c}\hat{\rho}\hat{c}^\dagger - \frac{1}{2}\{\hat{c}^\dagger\hat{c}, \hat{\rho}\}$ is the superoperator that represents the backaction induced in the system by the continuous measurement, and $\{\cdot\}$ is the anti-commutator. The third term in Eq. (2.22) represents the stochastic update of the density matrix based on the knowledge obtained from the measurement outcome. It contains a non-linear term that preserves the density matrix's trace and purity (for a unitary Liouville operator).

2.4 Quantum Fokker-Planck Master Equation

As it will be important later, in this section, I reproduce the derivation of the Quantum Fokker-Planck Master Equation (QFPME) [1, 3, 77] using the stochastic calculus method described in the Supplemental Material of Ref. [1]. The QFPME describes the ensemble evolution of the joint quantum system and the filtered measured outcome in a continuously monitored system modeled by the Gaussian weak measurement described in the previous section.

The starting point of this section is the Belavkin Eq. (2.22) obtained using Gaussian weak measurements. Coupled with the evolution of the quantum system, one has access to the classical noisy signal $z(t)$ described by Eq. (2.20). Based on this signal, it is possible to apply feedback by changing the Hamiltonian using the measurement outcome [80]. However, one is limited to linear feedback of the form

$$\hat{H}(z) = \hat{H}_0 + z\hat{V} \quad (2.23)$$

because the signal $z(t)$ has ill-defined higher moments. Motivated by this limitation and the fact that real-world experiments cannot measure changes with infinite speed, the authors in Ref. [1] introduced a filtered version of the classical signal to model the finite bandwidth of the experi-

ment:

$$D(t) = \gamma \int_{-\infty}^t dt' e^{\gamma(t-t')} z(t'). \quad (2.24)$$

Here, γ represents the detector bandwidth, and it is intuitively related to the delay (or lag) timescale $t_d \sim \gamma^{-1}$ necessary for the experiment to measure changes in the system.

The signal $z(t)$ is not continuous and nowhere differentiable because it is defined in terms of a Gaussian white noise in Eq. (2.20). Conversely, the smoother signal $D(t)$ is continuous and evolves similarly to an Ornstein–Uhlenbeck (OU) process [75]:

$$dD = \gamma(\langle \hat{A} \rangle - D) dt + \frac{\gamma}{\sqrt{4\lambda}} dW. \quad (2.25)$$

The first term generates an exponential decay towards the expected value of the measured operator, while the second term adds noise to the evolution. The diffusive constant of the OU dynamics is given by $\gamma^2/8\lambda$.

Now, it is possible to apply general feedback, here described as a protocol (or a function) $\hat{H}(D)$ based on the filtered measured outcome. The following coupled stochastic equations describe the joint evolution of the quantum system and the measured outcome:

$$d\hat{\rho} = -\frac{i}{\hbar} [\hat{H}(D), \hat{\rho}] dt + \lambda dt \mathcal{D}[\hat{A}]\hat{\rho} + \sqrt{\lambda} dW \left\{ \hat{A} - \langle \hat{A} \rangle, \hat{\rho} \right\}, \quad (2.26)$$

$$dD = \gamma(\langle \hat{A} \rangle - D) dt + \frac{\gamma}{\sqrt{4\lambda}} dW. \quad (2.27)$$

The evolution of this system of equations is non-deterministic, as it depends on the particular realizations of the stochastic Wiener increments. To work with a deterministic description, rather than a stochastic one, the authors of Ref. [1] introduced an ensemble picture by defining a new

object

$$\hat{\rho}(D', t) \equiv \mathbb{E}_W[\hat{\rho}(t)\delta(D' - D(t))], \quad (2.28)$$

where $\mathbb{E}_W[\cdot]$ represents the stochastic average over the noise. This quantity represents a joint “distribution” as it contains information on the quantum state and the distribution of measurement outcomes consistent with the particular measured value $D(t)$ at time t . In Eq. (2.28), we average over all quantum states compatible with the measured outcome $D(t)$ at time t . This reflects that our only source of information is the outcome that one measures and not the quantum state directly.

The evolution of $\hat{\rho}(D', t)$ can be solved by taking the derivative of both sides of Eq. (2.28) and using the properties of stochastic calculus discussed in Sec. 1.5.3. The final step is to use the following identities that are valid for a general smooth function $f(D')$ [68]:

$$\frac{\partial}{\partial D'}\delta(D' - D) = -\frac{\partial}{\partial D}\delta(D' - D), \quad (2.29a)$$

$$\left[\frac{\partial}{\partial D'}\delta(D' - D) \right] f(D') = \frac{\partial}{\partial D'} [\delta(D' - D)f(D)]. \quad (2.29b)$$

Combining these ingredients, we obtain the QFPME for a single measurement [1]:

$$\partial_t \hat{\rho}(D, t) = \frac{-i}{\hbar} [\hat{H}(D), \hat{\rho}(D, t)] + \lambda \mathcal{D}[\hat{A}] \hat{\rho}(D, t) - \frac{\gamma}{2} \partial_D \{ \hat{A} - D, \hat{\rho}(D, t) \} + \frac{\gamma^2}{8\lambda} \partial_D^2 \hat{\rho}(D, t) \quad (2.30)$$

The first term corresponds to unitary evolution with arbitrary feedback protocol $\hat{H}(D)$; the second is the measurement backaction, which causes decoherence on the basis of the measured operator [see Eq. (1.24)]. The last two terms form a Fokker-Planck-like equation, where the third term is a drift of the measured operator towards the operator being measured, and the final term represents

the diffusion in the measurement outcome space. See [1] for a detailed discussion. A classical derivation of Eq. (2.30) using Bayesian inference is found in Ref. [57].

In the next two sections, I introduce variations of the weak measurement model. The aim is to be able to model more realistic experimental situations and gain intuition on the applications of weak measurements and continuous measurements.

2.5 Inertial model for a weak measurement

The starting point for the Belavkin equation and the QFPME is the POVM derived from the linear interaction Hamiltonian in Sec. 2.2. In this section, I will re-derive the weak measurement POVM starting from an “inertial” model that considers the initial pointer’s mass (inertia). After correctly choosing the physical parameters, one can rederive the Belavkin equation with a correction that depends on the pointer’s mass.

One can use the same physical model as in Sec. (2.2) but consider the kinetic energy. The setup is similar; we have two degrees of freedom: a spatial system described by position and momentum and a finite-dimensional internal degree of freedom. The total Hamiltonian for this model is

$$\hat{H} = \frac{\hat{p}^2}{2m} - k\hat{x}\hat{A}. \quad (2.31)$$

The operators \hat{x} and \hat{p} are position and momentum; k controls the intensity of the interaction; and $\hat{A} = \sum_a \xi_a |\xi_a\rangle\langle\xi_a|$ is the operator we are trying to measure. The initial joint quantum state is assumed to be in a product state:

$$|\Psi_0\rangle = |\alpha\rangle |\phi_a\rangle. \quad (2.32)$$

The state $|\alpha\rangle$ refers to the auxiliary system that will be measured (pointer). The pointer is assumed to be in a Gaussian initial state in the momentum representation

$$\langle p|\alpha\rangle = \left(\frac{2\lambda}{\pi}\right) e^{-\lambda p^2}. \quad (2.33)$$

The state $|\phi_a\rangle$ is a generic state of the system that one is interested in measuring.

To solve for the time evolution of the system, we will use the Zassenhaus formula of the exponential operator algebra [93]

$$e^{\hat{X}+\hat{Y}} = e^{\hat{X}}e^{\hat{Y}}e^{-\frac{1}{2}[\hat{X},\hat{Y}]}e^{\frac{1}{6}(2[\hat{Y},[\hat{X},\hat{Y}]]+[\hat{X},[\hat{X},\hat{Y}]])}, \quad (2.34)$$

where \hat{X} and \hat{Y} are well-behaved operators. This formula, in general, contains additional terms, but in the case of $\hat{X} \propto \hat{p}^2$ and $\hat{Y} \propto \hat{x}$, these terms vanish. Using Eq. (2.34), the time unitary operator can be written as ($\hbar = 1$):

$$e^{-i\delta t\hat{H}_I} = e^{-i\delta t\frac{\hat{p}^2}{2m}}e^{i\delta tk\hat{x}\hat{A}}e^{i(\delta t)^2k\hat{A}\hat{p}/2m}e^{i(\delta t)^3k^2\hat{A}^2/m}. \quad (2.35)$$

Here, we choose the interaction time to be small, $\delta t \rightarrow 0$, because we want to define a continuous limit where the interaction (and measurement) is repeated very often. Once the system has interacted with the ancilla (pointer) state, one measures the pointer's momentum. This operation

defines the POVM of the weak measurement:

$$|\Psi_{\mathbf{t}}\rangle = e^{-i\delta t \hat{H}_I} |\alpha\rangle |\phi_a\rangle, \quad (2.36)$$

$$\langle p | \Psi_{\mathbf{t}} \rangle_{\text{meas}} = \sum_a \langle p | e^{-i\delta t \frac{\hat{p}^2}{2m}} e^{i\delta t k \hat{x} \xi_a} e^{i(\delta t)^2 k \xi_a \hat{p}/2m} e^{(\delta t)^3 k^2 \xi_a^2/m} |\xi_a\rangle |\alpha\rangle \langle \xi_a | \phi_a \rangle, \quad (2.37)$$

$$|\phi_a\rangle_{\text{meas}} = \frac{\hat{M}(p) |\phi_a\rangle}{\sqrt{\langle \phi_a | \hat{M}^\dagger(p) \hat{M}(p) | \phi_a \rangle}}, \quad (2.38)$$

$$\hat{M}(p) = \sum_a \langle p | e^{-i\delta t \frac{\hat{p}^2}{2m}} e^{i\delta t k \hat{x} \xi_a} e^{i(\delta t)^2 k \xi_a \hat{p}/2m} e^{(\delta t)^3 k^2 \xi_a^2/m} |\alpha\rangle \langle \xi_a | \langle \xi_a |. \quad (2.39)$$

Using Eq. (2.33), the measurement POVM can be written as

$$\hat{M}(p) = \left(\frac{2\lambda}{\pi} \right)^{1/4} e^{-i\delta t p^2/2m} e^{i\delta t^2 k \hat{A}(p - \delta t k \hat{A})/2m} e^{\frac{i}{3} \delta t^3 k^2 \hat{A}^2/m} e^{-\lambda(p - k\delta t \hat{A})^2}. \quad (2.40)$$

To make the measurement weak and also have a finite effect as one collects multiple POVMs at every time step δt , one needs to consider the following conditions [note that λ is defined by Eq. (2.33)]:

$$k \rightarrow \frac{1}{\delta t}, \quad \lambda \rightarrow \lambda \delta t. \quad (2.41)$$

Thus, the POVM of this inertial weak measurement model can be written as:

$$\hat{M}(p) = \left(\frac{2\lambda}{\pi} \right)^{1/4} e^{i\delta t \hat{A}(p - \hat{A})/2m} e^{\frac{i}{3} \delta t \hat{A}^2/m} e^{-\lambda \delta t (p - \hat{A})^2}. \quad (2.42)$$

Note that we can neglect the phase factor related to the kinetic energy because that only adds a complex phase to the quantum state.

Under these assumptions, the probability distribution of the measured outcome

$$P(p) = \langle \phi_a | \hat{M}^\dagger(p) \hat{M}(p) | \phi_a \rangle \quad (2.43)$$

is approximately Gaussian. The measurement outcome can be described as a white Gaussian noise of the form

$$p = \langle \hat{A} \rangle + \frac{\delta W}{\sqrt{4\lambda\delta t}}, \quad (2.44)$$

similar to Eq. (2.20). Finally, to derive the equivalent of a Belavkin equation for the inertial model, let's write the update of a generic quantum state by the POVM

$$\hat{\rho}_{t+\delta t} = e^{-i\delta t \hat{H}} \frac{\hat{M}(p) \hat{\rho}_t \hat{M}^\dagger(p)}{\text{Tr} \left\{ \hat{M}(p) \hat{\rho}_t \hat{M}^\dagger(p) \right\}} e^{i\delta t \hat{H}}. \quad (2.45)$$

Here, \hat{H} denotes the underlying quantum dynamics over the system of interest. Expanding all terms up to first order in δt and second order in δW (because $\delta W^2 = \delta t$), we get:

$$\begin{aligned} d\hat{\rho} = -i \left[\hat{H} - \frac{\hat{A}}{4m} \left(\frac{\hat{A}}{3} + \langle \hat{A} \rangle + \frac{1}{\sqrt{\lambda}} \frac{dW}{dt} \right), \hat{\rho} \right] dt + \\ \left(\lambda + \frac{1}{16\lambda m^2} \right) \mathcal{D}[\hat{A}] \hat{\rho} dt + \sqrt{\lambda} \{ \hat{A} - \langle \hat{A} \rangle, \hat{\rho} \} dW. \end{aligned} \quad (2.46)$$

In the limit $m \rightarrow \infty$, we recover Eq. (2.22), which was derived in Sec. 2.3 starting from a model without kinetic energy. A pointer with infinite mass doesn't feel any change in momentum caused by the interaction with the quantum system. It is interesting to note the contribution of the finite mass to the Hamiltonian and the backaction. The Hamiltonian gets a quadratic, a nonlinear, and a stochastic term in the operator \hat{A} . In particular, the stochastic term enters as

a white noise contribution, similar to the linear feedback quantum master equation [80]. The backaction is increased by a term that is proportional to $1/\lambda$. This fact creates a situation where neither small nor big values of λ decrease the backaction as in the usual Belavkin equation, but rather an intermediate value.

2.6 Harmonic model for weak measurement

Similar to the setup in Sec. 2.5, in this section, I will re-derive the weak measurement POVM starting from a “harmonic” model with a bounded Hamiltonian. The measurement signal evolves similarly to an OU particle without the assumption of low-pass filtering introduced in Eq. (2.24).

The starting point for this model is to consider a system with two degrees of freedom: a spatial degree described by position and momentum and a finite-dimensional internal degree of freedom. The interaction Hamiltonian for this model is

$$\hat{H}_I = \frac{\hat{p}^2}{2m} + \frac{m\Omega^2}{2}(\hat{x} - \hat{A})^2. \quad (2.47)$$

The operators \hat{x} and \hat{p} are position and momentum; Ω is the frequency of the interaction harmonic oscillator; and $\hat{A} = \sum_a \xi_a |\xi_a\rangle\langle\xi_a|$ is the operator we are trying to measure, that acts in the internal degrees of freedom. The initial joint quantum state is assumed to be in a product state:

$$|\Psi_0\rangle = |\alpha\rangle |\phi_a\rangle, \quad (2.48)$$

where $|\alpha\rangle$ describes the wavefunction auxiliary system to be measured and $|\phi_a\rangle$ describes the

internal state of the particle. The state $|\phi_a\rangle$ is arbitrary, and we aim to find the value corresponding to the measure of operator \hat{A} . To solve for the time evolution, we need to calculate how the unitary time operator acts on the initial wavefunction

$$|\Psi_t\rangle = e^{-i\hat{H}_I t/\hbar} |\Psi_0\rangle = \sum_a e^{-i\hat{H}_a t/\hbar} |\alpha\rangle |\xi_a\rangle \langle \xi_a | \phi_a \rangle, \quad (2.49)$$

where we define the “component” of the total Hamiltonian that lives in a particular eigenstate of the operator \hat{A} :

$$\hat{H}_a = \frac{\hat{p}^2}{2m} + \frac{m\Omega^2}{2} (\hat{x} - \xi_a)^2. \quad (2.50)$$

Once we define the Hamiltonian (2.50), the evolution of the wavefunction in Eq. (2.49) reduces to solving the time evolution of a displaced quantum harmonic oscillator. In addition, let’s define the “bare” Hamiltonian

$$\hat{H}_0 = \frac{\hat{p}^2}{2m} + \frac{m\Omega^2}{2} \hat{x}^2, \quad (2.51)$$

and the canonical lowering (raising) \hat{a} (\hat{a}^\dagger) operator:

$$\hat{a} = \sqrt{\frac{m\Omega}{2\hbar}} \left(\hat{x} + \frac{i}{m\Omega} \hat{p} \right). \quad (2.52)$$

To solve for the evolution of a displaced quantum harmonic oscillator, I use the following

properties of the displacement operator:

$$\hat{D}(\alpha) |0\rangle = |\alpha\rangle, \quad (2.53)$$

$$\hat{D}^\dagger(\alpha)\hat{D}(\alpha) = \hat{D}(\alpha)\hat{D}^\dagger(\alpha) = \hat{1}, \quad (2.54)$$

$$\hat{D}^\dagger(\alpha) = \hat{D}(-\alpha), \quad (2.55)$$

$$\hat{D}(\alpha)\hat{a}\hat{D}^\dagger(\alpha) = \hat{a} - \alpha, \quad (2.56)$$

$$\hat{D}(\alpha)\hat{a}^\dagger\hat{D}^\dagger(\alpha) = \hat{a}^\dagger - \alpha^*, \quad (2.57)$$

$$\hat{D}(\alpha)\hat{D}(\beta) = e^{(\alpha\beta^* - \alpha^*\beta)/2}\hat{D}(\alpha + \beta), \quad (2.58)$$

and the evolution of a coherent state by the bare Hamiltonian

$$e^{-it\hat{H}_0/\hbar} |\alpha\rangle = e^{-i\Omega t/2} |\alpha e^{-i\Omega t}\rangle. \quad (2.59)$$

First, note that we can displace the evolution of the bare Hamiltonian (2.51) into the evolution of any component Hamiltonian (2.50) using Eqs. (2.54-2.57):

$$\hat{D}\left(\sqrt{\frac{m\Omega}{2\hbar}}\xi_a\right) e^{-it\hat{H}_0/\hbar} \hat{D}^\dagger\left(\sqrt{\frac{m\Omega}{2\hbar}}\xi_a\right) = e^{-it\hat{H}_a/\hbar}. \quad (2.60)$$

The next step is to consider that the initial state of the auxiliary system is a coherent (displaced) state in Eq. (2.48):

$$|\alpha\rangle = \left| \sqrt{\frac{m\Omega}{2\hbar}} y \right\rangle. \quad (2.61)$$

Using these equations, one can calculate the evolution of the initial coherent state by the

component Hamiltonian:

$$e^{-it\hat{H}_a/\hbar} \left| \sqrt{\frac{m\Omega}{2\hbar}} y \right\rangle = \hat{D} \left(\sqrt{\frac{m\Omega}{2\hbar}} \xi_a \right) e^{-it\hat{H}_0/\hbar} \hat{D}^\dagger \left(\sqrt{\frac{m\Omega}{2\hbar}} \xi_a \right) \hat{D} \left(\sqrt{\frac{m\Omega}{2\hbar}} y \right) |0\rangle \quad (2.62)$$

$$= \hat{D} \left(\sqrt{\frac{m\Omega}{2\hbar}} \xi_a \right) e^{-it\hat{H}_0/\hbar} \left| \sqrt{\frac{m\Omega}{2\hbar}} (y - \xi_a) \right\rangle \quad (2.63)$$

$$= \hat{D} \left(\sqrt{\frac{m\Omega}{2\hbar}} \xi_a \right) e^{-i\Omega t/2} \left| \sqrt{\frac{m\Omega}{2\hbar}} (y - \xi_a) e^{-i\Omega t} \right\rangle \quad (2.64)$$

$$= e^{-i\Omega t/2} e^{i\frac{m\Omega}{2\hbar} \xi_a (y - \xi_a) \sin \Omega t} \left| \sqrt{\frac{m\Omega}{2\hbar}} [\xi_a + (y - \xi_a) e^{-i\Omega t}] \right\rangle \quad (2.65)$$

Finally, one can express the final state of the total quantum system after the interaction as

$$|\Psi_t\rangle = e^{-i\Omega t/2} \sum_a e^{i\frac{m\Omega}{2\hbar} \xi_a (y - \xi_a) \sin \Omega t} \left| \sqrt{\frac{m\Omega}{2\hbar}} [\xi_a + (y - \xi_a) e^{-i\Omega t}] \right\rangle |\xi_a\rangle \langle \xi_a | \phi_a \rangle. \quad (2.66)$$

Once the state has evolved, one can apply a position or a momentum measurement. I'll discuss both cases in detail.

2.6.1 Momentum measurement

Let's consider measurement in the momentum basis. The post-measurement state and the probability distribution of the measurement outcomes are

$$\langle p | \Psi_t \rangle_{\text{meas}} = \frac{e^{-i\Omega t/2} \sum_a e^{i\frac{m\Omega}{2\hbar} \xi_a (y - \xi_a) \sin \Omega t} \left\langle p \left| \sqrt{\frac{m\Omega}{2\hbar}} [\xi_a + (y - \xi_a) e^{-i\Omega t}] \right\rangle |\xi_a\rangle \langle \xi_a | \phi_a \rangle}{\sqrt{P(p)}}, \quad (2.67)$$

$$P(p) = \sum_a \left| \left\langle p \left| \sqrt{\frac{m\Omega}{2\hbar}} [\xi_a + (y - \xi_a) e^{-i\Omega t}] \right\rangle \right|^2 |\langle \xi_a | \phi_a \rangle|^2. \quad (2.68)$$

The coherent states $|\alpha\rangle$ have Gaussian profiles in position and momentum space; thus, the overall probability distribution in Eq. (2.68) is a sum of Gaussians with relative probability given by the projection of the internal state into the eigenstates of the operator \hat{A} .

The average momentum and momentum variance of a single coherent state are given by:

$$\langle \hat{p} \rangle_\alpha = \langle \alpha | \hat{p} | \alpha \rangle = \sqrt{2\hbar m \Omega} \operatorname{Im}(\alpha), \quad (2.69)$$

$$\sigma_{p,\alpha} = \sqrt{\langle \alpha | \hat{p}^2 | \alpha \rangle - \langle \alpha | \hat{p} | \alpha \rangle^2} = \sqrt{\frac{\hbar m \Omega}{2}}. \quad (2.70)$$

Thus, the average value and variance of the measurement outcome p are given by:

$$\langle p \rangle = \int dp p P(p) = m\Omega(\langle \hat{A} \rangle - y) \sin \Omega t, \quad (2.71)$$

$$\sigma_p^2 = \int dp (p - \langle p \rangle)^2 P(p) = \frac{\hbar m \Omega}{2} + \sigma_A^2 m^2 \Omega^2 \sin^2 \Omega t \quad (2.72)$$

Now, assume the interaction time is small $t \rightarrow \delta t$. In this condition, the average value and measurement variance read:

$$\langle p \rangle = (\langle \hat{A} \rangle - y) m \Omega^2 \delta t + \mathcal{O}(\delta t^3), \quad (2.73)$$

$$\sigma_p^2 = \frac{\hbar m \Omega}{2} + \mathcal{O}(\delta t^2). \quad (2.74)$$

Because in the limit $\delta t \rightarrow 0$, the variance of the Gaussians is much larger than the separation between them, we can consider that the distribution in Eq. (2.68) coalesces into a single Gaussian distribution whose first two moments are given by Eqs. (2.73,2.74). This approximation in the

probability distribution allow us to write the measurement outcome as a stochastic variable:

$$p_s = (\langle \hat{A} \rangle - y)m\Omega^2\delta t + \sqrt{\frac{\hbar m \Omega}{2}}W. \quad (2.75)$$

Here, $W \sim \mathcal{N}(0, 1)$ is a Gaussian random variable distributed with zero mean and unitary variance. Despite the interaction time being small, consider that the stiffness of the harmonic potential is large, such that the product

$$\Omega^2\delta t \equiv \gamma \quad \Rightarrow \quad \Omega = \sqrt{\frac{\gamma}{\delta t}} \quad (2.76)$$

is finite. The stochastic variable can be rewritten as

$$p_s = (\langle \hat{A} \rangle - y)m\gamma + \left(\frac{\hbar^2 m^2}{4}\gamma\delta t\right)^{1/4} \frac{\delta W}{\delta t}, \quad (2.77)$$

where $\delta W \sim \mathcal{N}(0, \delta t)$ is a Wiener increment.

The measurement scheme I have introduced here is meant to model a continuous process, meaning that it will be applied to the quantum system every time step δt . In a given time t , consider the auxiliary system is initialized to the state in Eq. (2.48) with a particular value y_t that can be controlled.

The value of the measured momentum in Eq. (2.77) is similar to the momentum of a Brownian particle being “kicked” by the surrounding environment. Consider that the experimentalist updates the value of the parameter y_t to mimic the “position” of the auxiliary system

$$y_{t+1} = y_t + \frac{p_s}{m}\delta t. \quad (2.78)$$

The signal y_t evolves similarly to an OU particle

$$y_{t+1} - y_t = dy = \gamma(\langle \hat{A} \rangle - y_t)\delta t + \frac{\gamma}{\sqrt{4\lambda}}\delta W, \quad (2.79)$$

where we define

$$\left(\frac{\hbar^2}{4m^2}\gamma\delta t\right)^{1/4} \equiv \frac{\gamma}{\sqrt{4\lambda}} \Rightarrow \lambda = \frac{m}{2\hbar}\sqrt{\frac{\gamma^3}{\delta t}}. \quad (2.80)$$

to control the amount of noise in the system. Note the similarity with Eq. (2.25) without the explicit assumption of a low-pass filter on the weak measurement signal.

We can rewrite the evolution of the quantum state in Eq. (2.67) in terms of the new variables. Let's redefine the variables m, Ω in terms of $\lambda, \gamma, \delta t$:

$$\Omega = \sqrt{\frac{\gamma}{\delta t}}, \quad \frac{m}{\hbar} = 2\lambda\sqrt{\frac{\delta t}{\gamma^3}}. \quad (2.81)$$

Then, the post-measurement state in Eq. (2.67) is equivalent to the action of the following POVM into the generic quantum state ρ :

$$\hat{M}(p|y_t) = e^{-i\Omega t/2} \sum_a e^{i\frac{m\Omega}{2\hbar}\xi_a(y_t - \xi_a) \sin \Omega \delta t} \left\langle p \left| \sqrt{\frac{m\Omega}{2\hbar}} [\xi_a + (y_t - \xi_a)e^{-i\Omega \delta t}] \right. \right\rangle |\xi_a\rangle \langle \xi_a|, \quad (2.82)$$

$$\hat{\rho}_{t+1} = e^{\mathcal{L}\delta t} \frac{\hat{M}(p|y_t)\hat{\rho}_t\hat{M}^\dagger(p|y_t)}{\text{Tr}\{\hat{M}(p|y_t)\hat{\rho}_t\hat{M}^\dagger(p|y_t)\}}. \quad (2.83)$$

To calculate the exact form of the POVM, it is useful to consider the coherent state in momentum

representation:

$$\left\langle p \left| \sqrt{\frac{m\Omega}{2\hbar}} [\xi_a + (y_t - \xi_a)e^{-i\Omega\delta t}] \right\rangle = \left(\frac{1}{\pi\hbar m\Omega} \right)^{1/4} e^{-\frac{ip\langle x \rangle}{\hbar}} e^{\frac{i\langle p \rangle \langle x \rangle}{2\hbar}} e^{-\frac{1}{2\hbar m\Omega} (p - \langle p \rangle)^2}, \quad (2.84)$$

$$\langle x \rangle = \sqrt{\frac{2\hbar}{m\Omega}} \operatorname{Re} \left(\sqrt{\frac{m\Omega}{2\hbar}} [\xi_a + (y_t - \xi_a)e^{-i\Omega\delta t}] \right) = y_t + (\xi_a - y_t)\gamma\delta t/2, \quad (2.85)$$

$$\langle p \rangle = \sqrt{\frac{\hbar m\Omega}{2}} \operatorname{Im} \left(\sqrt{\frac{m\Omega}{2\hbar}} [\xi_a + (y_t - \xi_a)e^{-i\Omega\delta t}] \right) = m\gamma(\xi_a - y_t). \quad (2.86)$$

The POVM can be written as:

$$\begin{aligned} \hat{M}(p|y_t) = & \left(\frac{1}{\pi\hbar m\Omega} \right)^{1/4} e^{-\frac{2i\lambda}{\gamma} \hat{A}(\hat{A}-y_t)\sqrt{\gamma\delta t}} e^{-\frac{2i\lambda}{\gamma} \sqrt{\gamma\delta t}(y_t + (\hat{A}-y_t)\gamma\delta t/2)} \left[(\langle \hat{A} \rangle - y_t) + \frac{1}{\sqrt{4\lambda}} \frac{\delta W}{\delta t} - (\hat{A}-y_t)/2 \right] \\ & \times e^{-\lambda\delta t \left[(\langle \hat{A} \rangle - \hat{A}) + \frac{1}{\sqrt{4\lambda}} \frac{\delta W}{\delta t} \right]^2}, \end{aligned} \quad (2.87)$$

where I used the fact that p is given by Eq. (2.77). Note that the phase terms in Eq. (2.87) have a term that depends on $\sqrt{\delta t}$, which would lead to inconsistencies in the master equation expansion of the POVM. One possible solution would be to consider that the protocol works by applying a unitary evolution to cancel out the phase factor present in the definition of the coherent state.

In the end, the POVM that evolves the quantum state is written as:

$$\hat{M}(p|y_t) \rightarrow \left(\frac{2\lambda}{\pi\gamma^2\delta t} \right)^{1/4} e^{-\lambda\delta t \left[(\langle \hat{A} \rangle - \hat{A}) + \frac{1}{\sqrt{4\lambda}} \frac{\delta W}{\delta t} \right]^2}. \quad (2.88)$$

Equation (2.88) is equivalent to use Eqs. (2.13) and (2.20). The update of the quantum state based on the POVM (2.88) leads to the Belavkin equation (2.22) [1, 69]. Then, combining the Belavkin equation with the continuous signal in Eq. (2.78), one can derive the QFPME (2.30) using the

stochastic steps of Ref. [1], reproduced in Sec. 2.4.

2.6.2 Position measurement

A similar filtered signal can be derived using the harmonic model if one measures the total system in the position basis rather than momentum. The steps are similar: once the state has evolved, one applies a measurement on the position basis. The post-measurement state and the probability distribution of the measurement outcomes are

$$\langle x | \Psi_t \rangle_{\text{meas}} = \frac{e^{-i\Omega t/2} \sum_a e^{i\frac{m\Omega}{2\hbar} \xi_a (y - \xi_a) \sin \Omega t} \left\langle x \left| \sqrt{\frac{m\Omega}{2\hbar}} [\xi_a + (y - \xi_a)e^{-i\Omega t}] \right\rangle |\xi_a\rangle \langle \xi_a | \phi_a \right\rangle}{\sqrt{P(x)}}, \quad (2.89)$$

$$P(x) = \sum_a \left| \left\langle x \left| \sqrt{\frac{m\Omega}{2\hbar}} [\xi_a + (y - \xi_a)e^{-i\Omega t}] \right\rangle \right|^2 |\langle \xi_a | \phi_a \rangle|^2. \quad (2.90)$$

The average position and position variance of a single coherent state are given by:

$$\langle \hat{x} \rangle_\alpha = \langle \alpha | \hat{x} | \alpha \rangle = \sqrt{\frac{2\hbar}{m\Omega}} \text{Re}(\alpha), \quad (2.91)$$

$$\sigma_{x,\alpha} = \sqrt{\langle \alpha | \hat{x}^2 | \alpha \rangle - \langle \alpha | \hat{x} | \alpha \rangle^2} = \sqrt{\frac{\hbar}{2m\Omega}}. \quad (2.92)$$

Thus, the average value and variance of the measurement outcome x are given by:

$$\langle x \rangle = \int dx x P(x) = \langle \hat{A} \rangle + (y - \langle \hat{A} \rangle) \cos \Omega t, \quad (2.93)$$

$$\sigma_x^2 = \int dx (x - \langle x \rangle)^2 P(x) = \frac{\hbar}{2m\Omega} + \sigma_A^2 (1 - \cos \Omega t)^2 \quad (2.94)$$

Now, consider that the interaction time is small $t \rightarrow \delta t$. In this situation, the average value

and measurement variance read:

$$\langle x \rangle = y + (\langle \hat{A} \rangle - y) \frac{\Omega^2 (\delta t)^2}{2} + \mathcal{O}(\delta t^4), \quad (2.95)$$

$$\sigma_x^2 = \frac{\hbar}{2m\Omega} + \mathcal{O}(\delta t^4). \quad (2.96)$$

Because in the limit $\delta t \rightarrow 0$, the variance of the Gaussians is much larger than the separation between them, we can consider that the distribution in Eq. (2.90) coalesces into a single Gaussian distribution whose first two moments are given by Eqs. (2.95,2.96). This approximation in the probability distribution allows us to write the measurement outcome as a stochastic variable:

$$x_s = y + (\langle \hat{A} \rangle - y) \frac{\Omega^2 \delta t^2}{2} + \sqrt{\frac{\hbar}{2m\Omega}} W. \quad (2.97)$$

Despite the interaction time being small, consider that the stiffness of the harmonic potential is large, such that the product

$$\Omega^2 \delta t / 2 \equiv \gamma \quad \Rightarrow \quad \Omega = \sqrt{\frac{2\gamma}{\delta t}} \quad (2.98)$$

is finite. The stochastic variable can be rewritten as

$$x_s = y + (\langle \hat{A} \rangle - y) \gamma \delta t + \left(\frac{\hbar^2}{4m^2} \frac{1}{2\gamma \delta t} \right)^{1/4} \sqrt{\delta t} W, \quad (2.99)$$

$$x_s = y + (\langle \hat{A} \rangle - y) \gamma \delta t + \frac{\gamma}{\sqrt{4\lambda}} \delta W, \quad (2.100)$$

with λ controlling the amount of noise in the stochastic variable:

$$\left(\frac{\hbar^2}{4m^2} \frac{1}{2\gamma \delta t} \right)^{1/4} \equiv \frac{\gamma}{\sqrt{4\lambda}} \quad \Rightarrow \quad \lambda = \frac{m}{\hbar} \sqrt{\frac{\gamma^5 \delta t}{2}}. \quad (2.101)$$

The measurement outcome x_s should be understood as the measurement outcome at a given time. Also, imagine that the experimental setup can prepare the initial auxiliary system based on the measurement outcome of the previous step.

$$x_s \sim D_t, \quad (2.102)$$

$$y \sim D_{t-1}. \quad (2.103)$$

This setup creates a time trace D_t that describes the measurement outcome in time. The evolution of the signal D_t is described by:

$$D_t - D_{t-1} \equiv dD = (\langle \hat{A} \rangle - D_{t-1})\gamma\delta t + \frac{\gamma}{\sqrt{4\lambda}}\delta W. \quad (2.104)$$

Note the similarity with Eq. (2.25) without the explicit assumption of a low-pass filter on the weak measurement signal.

To solve for the evolution of the quantum state in Eq. (2.89) let's redefine the variables m, Ω in terms of $\lambda, \gamma, \delta t$:

$$\Omega = \sqrt{\frac{2\gamma}{\delta t}}, \quad \frac{m}{\hbar} = \lambda\sqrt{\frac{2}{\gamma^5\delta t}}. \quad (2.105)$$

The post-measurement state in Eq. (2.89) can be solved using the position representation of the

coherent states:

$$\left\langle x \left| \sqrt{\frac{m\Omega}{2\hbar}} [\xi_a + (D_t - \xi_a)e^{-i\Omega\delta t}] \right. \right\rangle = \left(\frac{1}{\pi\hbar m\Omega} \right)^{1/4} e^{\frac{i\langle p \rangle x}{\hbar}} e^{-\frac{i\langle p \rangle \langle x \rangle}{2\hbar}} e^{-\frac{m\Omega}{2\hbar}(x - \langle x \rangle)^2}, \quad (2.106)$$

$$\langle x \rangle = \sqrt{\frac{2\hbar}{m\Omega}} \operatorname{Re} \left(\sqrt{\frac{m\Omega}{2\hbar}} [\xi_a + (D_t - \xi_a)e^{-i\Omega\delta t}] \right) = D_t + (\xi_a - D_t)\gamma\delta t, \quad (2.107)$$

$$\langle p \rangle = \sqrt{\frac{\hbar m\Omega}{2}} \operatorname{Im} \left(\sqrt{\frac{m\Omega}{2\hbar}} [\xi_a + (D_t - \xi_a)e^{-i\Omega\delta t}] \right) = 2m\gamma(\xi_a - D_t). \quad (2.108)$$

The POVM equivalent to Eq. (2.89) can be written as:

$$\begin{aligned} \hat{M}(x|D_t) = & \left(\frac{m\Omega}{\pi} \right)^{1/4} e^{-\frac{2i\lambda}{\gamma} \hat{A}(D_t - \hat{A})} \sqrt{\frac{1}{\gamma\delta t}} \left[\frac{1}{2}(D_t - \hat{A}) + (\langle \hat{A} \rangle - \hat{A}/2 - D_t/2)\gamma\delta t + \frac{\gamma}{\sqrt{4\lambda}}\delta W \right] \\ & \times e^{-\left(\frac{\lambda}{\gamma^2\delta t}\right) \left[(\langle \hat{A} \rangle - \hat{A})\gamma\delta t + \frac{\gamma}{\sqrt{4\lambda}}\delta W \right]^2}. \end{aligned} \quad (2.109)$$

Similar to what happens with Eq. (2.88), here there is a problematic $\sqrt{1/\delta t}$ in the phase factor.

A possible solution is to consider that the true POVM consists of an additional unitary evolution to cancel out the phase factor in Eq. (2.109). In that situation, the evolution of the quantum state is given by:

$$\hat{M}(D_{t+1}|D_t) \rightarrow \left(\frac{2\lambda}{\pi\gamma^2\delta t} \right)^{1/4} e^{-\left(\frac{\lambda}{\gamma^2\delta t}\right) \left[(D_{t+1} - D_t) - (\hat{A} - D_t)\gamma\delta t \right]^2}, \quad (2.110)$$

$$\hat{\rho}_{t+1} = e^{\mathcal{L}\delta t} \frac{\hat{M}(D_{t+1}|D_t)\hat{\rho}_t\hat{M}^\dagger(D_{t+1}|D_t)}{\operatorname{Tr} \left\{ \hat{M}(D_{t+1}|D_t)\hat{\rho}_t\hat{M}^\dagger(D_{t+1}|D_t) \right\}} \quad (2.111)$$

Expanding this operator up to the second order in δW (and first order in δt), one can derive the Belavkin equation. Then, combining with the continuous signal in Eq. (2.104), one can derive the QFPME (2.30) using the stochastic steps of Ref. [1].

2.7 Discussion and concluding remarks

All weak measurement models presented here were studied with the goal of modeling systems under continuous monitoring. The impulsive model for weak measurement is the simplest as it doesn't consider the detector's inertia and assumes an initial state with a diverging variance that scales in the order of $1/\delta t$. The second model presented can generalize the Belavkin equation by considering the finite mass of the auxiliary system. A correction in the measurement backaction and the Hamiltonian is obtained. The new Hamiltonian has a term that resembles the linear feedback Hamiltonian used in early continuous feedback protocols. In contrast, the backaction has a new term that scales inversely with the so-called measurement strength, yielding a non-monotonic relation between the measurement backaction and the measurement strength.

Finally, I introduced the harmonic model for measurements. The model uses a bounded Hamiltonian with inertia and potential strength as free parameters for the auxiliary system. I showed that analytical results can be obtained using the algebra of displacement operators and coherent states. By separating the components of the total Hamiltonian that live in different eigenstates of the measured operator, one can find how the interesting degrees of freedom couple to the motional degrees of freedom of the pointer. This analytical model can also be used with both momentum and position measurements. This new feature is not present in the impulsive model, which only considers a linear interaction between the measured operator and the auxiliary system. Both the position and momentum measurement variations of the harmonic model yield naturally to a signal that evolves like an OU process — a critical ingredient that is included by hand in the modeling of QFPME [1]. In particular, the momentum measurement variation is connected to the classical picture of a Brownian particle attached to a spring in a stochastic environment. The

filtered signal evolves as a classical trajectory for the particle's position. However, the parameters in Eq. (2.81) or Eq. (2.105) give ill-defined POVMs that have either $\sqrt{\delta t}$ for $\sqrt{1/\delta t}$ dependencies in the phase factor. To correct these problems, I need to assume that a unitary evolution is added to balance the complex phases that are introduced by the position/momentum representation of the coherent state.

This chapter summarizes some developments in more general measurement models, particularly continuous measurements. The goal is to broaden the range of possibilities and options for experimentalists to model their experiments with stochastic master equations. For the following two chapters, I'll focus on the QFPME derived using the standard weak measurement protocol discussed in Sec. 2.3.

Chapter 3: Continuous feedback protocols for cooling and trapping a quantum harmonic oscillator

This chapter is based primarily on work done with Pharnam Bakhshinezhad, Björn Annby-Andersson, Patrick P. Potts, Peter Samuelsson, and Christopher Jarzynski, which has been published in the article "Continuous feedback protocols for cooling and trapping a quantum harmonic oscillator" [3] (Phys. Rev. E **111**, 014152). I contributed to this project by deriving analytical formulas for all protocols and organizing most of the results in the current presentation form. I also contributed to generalizing the QFPME for multiple measurements.

In this chapter, I apply the formalism of the Quantum Fokker-Planck Master Equation (see Chapter 2) to study the cooling and trapping of a harmonic oscillator for several protocols based on position and/or momentum measurements. Protocols can cool the oscillator down to, or close to, the ground state for suitable choices of parameters. This analysis provides an analytically solvable case study of quantum measurement and feedback and illustrates the application of the QFPME to continuous quantum systems.

3.1 Introduction

Technologies and techniques to manipulate individual quantum systems have advanced rapidly in recent years. Applications such as quantum computing [32, 94, 95] and sensing [96, 97]

rely on fine measurements and precise control, along with the ability to prepare systems in desired states. There is particular interest in cooling systems to near-zero temperatures, that is, near the ground state, where quantum phenomena typically become enhanced.

Standard techniques for cooling quantum systems include laser cooling [19, 98–100], evaporative cooling [101–104] and cavity cooling [105–107]. Alternatively, systems can be cooled through measurement and feedback [55, 82, 83, 108–112, 112–118], in a manner reminiscent of the Maxwell’s demon thought experiment. Fundamental costs and bounds associated with cooling quantum systems are subjects of active investigation [119–122].

Recently, Annby-Andersson et. al. [1] introduced a theoretical framework for modeling continuous, Markovian measurement and feedback of quantum systems. In this framework, an external agent continuously monitors a system observable \hat{A} using weak measurements [56, 68, 69, 123–131]. The noisy measurement outcome $D(t)$, supplied by a detector of finite bandwidth, enters as a parameter of the system’s Hamiltonian (or Liouvillean for an open system). In this manner, feedback is applied to the system, as seen in Fig. 3.1. The central result of this work is the QFPME, which is discussed in Sec. 2.4, describing the coupled dynamics of the quantum system and detector outcome at the ensemble level.

Here, we apply the framework of QFPME to study the cooling of a quantum harmonic oscillator under various feedback protocols. We imagine that an external agent continuously performs weak measurements of the system’s position, x , or momentum, p , or both, and manipulates the location of the harmonic well based on the measurement outcomes. The agent aims to bring the system to the harmonic oscillator ground state, centered at the origin, $x = 0$. We will see that the goals of cooling (to the ground state) and trapping (at the origin) compete with one another. This system is simple enough to obtain analytical results, allowing us to compare the asymptotic

energy under different protocols and to investigate quantitatively how the rate and degree of cooling depend on parameters such as the detector bandwidth, the oscillator’s natural frequency, and the measurement strength.

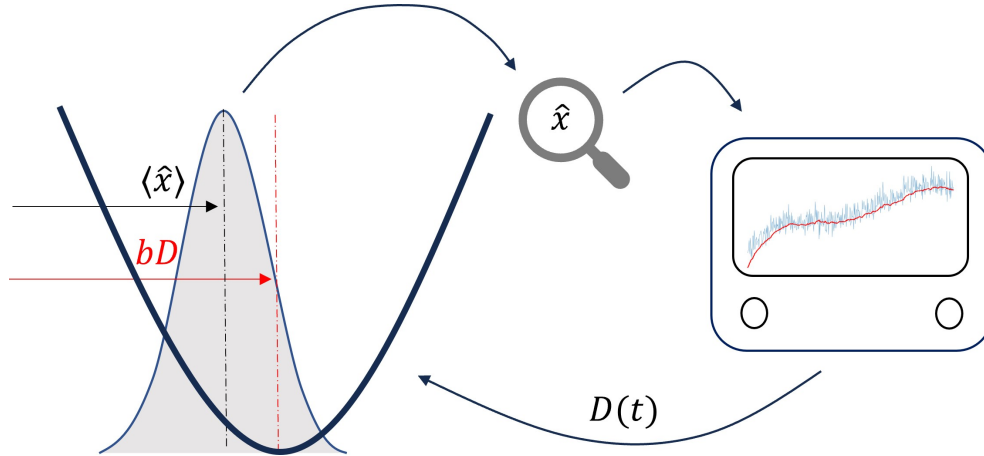


Figure 3.1: Illustration of Protocol X (defined in the next section). Cooling is achieved by measuring the position continuously and applying feedback by changing the location of the harmonic potential. The measurement outcome is a low-pass filtered version (red line) of the noisy weak measurement (light blue line).

At the same time, the cooling of a quantum harmonic oscillator is experimentally relevant and has been proposed and/or implemented in trapped ions, nano- and micro-mechanical resonators, levitated nanoparticles and optomechanical cavities [82, 106, 108, 109, 112, 114, 132–140]. The results presented in this work differ from previous studies of continuous feedback in harmonic oscillators [131, 141–144] due to the presence of finite bandwidth. This built-in feature of the QFPME [1] allows for feeding back non-linear functions of the measurement outcome.

Using the Markovianity of the QFPME and the system’s symmetries, we derive closed formulas for the asymptotic energy of a quantum harmonic oscillator under continuous feedback cooling. We show that by tuning the protocol, one can obtain either a cooling-focused protocol or a trapping-focused protocol. If the system is weakly coupled to a thermal bath, its final energy is an average of the asymptotic feedback energy and the thermal energy, weighted by the cooling

and thermal relaxation rates.

This chapter is structured as follows. In Sec. 3.2, we introduce the harmonic oscillator model and cooling protocols. Section 3.3 describes the cooling and trapping results achieved using these protocols. Section 3.4 presents numerical simulations and compares them with analytical results. Finally, we compare protocols in Sec. 3.5 and conclude in Sec. 3.6.

3.2 Model and QFPME

We consider a system that is continuously measured in one or more observables. Based on the outcomes of these measurements, which are generally noisy, an external agent implements a time-dependent Hamiltonian with the goal of decreasing the system's internal energy. We will refer to this process as a *cooling protocol*. As described above, a secondary aim is to trap the particle at or near the origin, in the long time limit.

3.2.1 Classical model

Although this chapter focuses on quantum feedback control, it is useful to gain intuition by first analyzing a classical cooling protocol. Consider a classical harmonic oscillator described by the Hamiltonian

$$H = \frac{p^2}{2m} + \frac{m\omega^2}{2}(x - bD_x)^2. \quad (3.1)$$

Here, D_x represents a recent measurement of the particle's position, and $b > 0$ is a fixed parameter that tunes how the external agent manipulates the harmonic well's location in response to this measurement. In the following, we describe the behavior of this system under both discrete and continuous cooling protocols. Details of the analyses of these protocols are found in

Appendix 3A.

We first consider a cooling protocol that proceeds in discrete time steps Δt , where Δt is not an integer multiple of π/ω . At each step, the agent measures the particle's current position (i.e. $D_x = x$) and instantaneously moves the trap's location to bD_x . Between measurements the particle evolves under the Hamiltonian H , with D_x fixed. If $b = 1$, the particle loses all of its potential energy at each step, as the minimum of the harmonic potential is moved to the particle's current location. At long times, the particle comes to rest at the minimum of the harmonic well, at a location $D_{x,\infty} \neq 0$ that depends on the initial position and momentum (x_0, p_0) (see Eq. (3.A2), and note that $D_{x,\infty} = x_\infty$). Thus the particle is cooled but is not trapped at the origin. By contrast, if $b < 1$ then at each time step the trap is placed between the particle's current location and the origin, and the particle relaxes asymptotically to rest at the origin ($D_{x,\infty} = 0$), hence both trapping and cooling are achieved. If $b > 1$ then these discrete dynamics become unstable and produce neither cooling nor trapping, as the trap is repeatedly placed further from the origin than the particle's current location.

To model the continuous version of this protocol and account for the fact that a real experimental apparatus does not respond instantaneously, we treat $D_x(t)$ as a dynamical variable that decays exponentially towards $x(t)$. Specifically, the system (x, p) and parameter D_x obey the equations of motion,

$$\begin{aligned} \dot{x} &= \frac{p}{m}, \\ \dot{p} &= -m\omega^2 (x - bD_x), \\ \dot{D}_x &= \gamma (x - D_x), \end{aligned} \tag{3.2}$$

where $\gamma > 0$ is a decay rate that characterizes the intrinsic lag of the experimental apparatus. The

value γ^{-1} roughly corresponds to Δt in the discrete case.

For $b < 1$, the dynamics generated by Eq. (3.2) relax to a stable fixed point at $p_\infty = x_\infty = D_{x,\infty} = 0$, thereby achieving both trapping and cooling. For $b > 1$, Eq. (3.2) produces unstable solutions in which both D_x and x accelerate at an exponential rate away from the origin. At the critical value $b = 1$, the system relaxes to a solution given by $p_\infty = 0$ and $x_\infty = D_{x,\infty} = D_{x0} + \gamma p_0/m\omega^2$ (Eq. (3.A7)); in this situation the particle is cooled but not trapped at the origin.

When $b = 1$, the relaxation timescale can be divided into two different regimes: a) if $\gamma < 2\omega$ the system is underdamped, and the relaxation rate is proportional to γ ; and b) if $\gamma > 2\omega$ the system is overdamped, and when $\gamma \gg \omega$ the relaxation rate is given by ω^2/γ , thus cooling occurs slowly.

We see that the discrete and the continuous protocols produce similar behavior for $b < 1$, $b = 1$ and $b > 1$. In the quantum case that we consider below, we use protocols analogous to the continuous protocol just presented, and the intuition on how to cool the system by manipulating the potential energy is similar. However, two additional ingredients appear in the quantum model: measurement backaction and measurement noise.

3.2.2 Quantum model - cooling protocols

Consider a quantum harmonic oscillator of mass m and characteristic frequency ω undergoing continuous measurement and feedback. Introducing dimensionless operators $\hat{p} \rightarrow \hat{p}\sqrt{\hbar m\omega}$ and $\hat{x} \rightarrow \hat{x}\sqrt{\hbar/m\omega}$, the Hamiltonian in the absence of feedback becomes

$$\hat{H}_0 = \frac{\hbar\omega}{2} (\hat{p}^2 + \hat{x}^2). \quad (3.3)$$

To implement feedback, we study three protocols similar to the one considered in the classical example. We imagine that position and/or momentum are continuously measured, and cooling is achieved by implementing a time-dependent Hamiltonian based on these measurements. The measurements correspond to Hermitian operators $\hat{A}_i \in \{\hat{x}, \hat{p}\}$, and feedback is applied through parameters $D_i \in \{D_x, D_p\}$, see Eqs. (3.4)-(3.6). These parameters correspond to the continuous measurement outcome and will be discussed in greater detail in the next section. They evolve similarly to D_x in Eq. (3.2).

Our first quantum protocol mimics the classical example. The position $\hat{A}_x = \hat{x}$ is measured, and feedback is applied through the parameter D_x of the Hamiltonian

$$\hat{H}_x(D_x) = \frac{\hbar\omega}{2} [\hat{p}^2 + (\hat{x} - bD_x)^2]. \quad (3.4)$$

We will refer to this situation as Protocol X, which is illustrated in Fig. 3.1. As in the classical model of Sec. 3.2.1, the parameter b controls how we move the minimum of the potential in response to the particle's measured location. We will see that b plays an important role in the trapping condition.

The second protocol generalizes the first by allowing both position and momentum measurements $\hat{A}_x = \hat{x}$ and $\hat{A}_p = \hat{p}$. Here the feedback Hamiltonian is

$$\hat{H}_{xp}(\mathbf{D}) = \frac{\hbar\omega}{2} [(\hat{p} - bD_p)^2 + (\hat{x} - bD_x)^2], \quad (3.5)$$

where $\mathbf{D} = (D_x, D_p)$. We will refer to this protocol as Protocol XP.

Our third protocol is inspired by the cold damping protocol [109, 145–151] that is widely

used for cooling and trapping experiments. In the cold damping protocol, measurements are performed in the position basis $\hat{A}_x = \hat{x}$ and feedback is applied to create a force to oppose the direction of the movement $H_{\text{feedback}} \propto \dot{D}_x \hat{x}$. However, the QFPME described in Sec. 2.4 requires a protocol that depends on D_x and not on its time-derivative \dot{D}_x . Hence, we introduce a feedback Hamiltonian with a term proportional to $-\hat{p}D_x$:

$$\hat{H}_c(D_x) = \frac{\hbar\omega}{2} [(\hat{p} - \mu D_x)^2 + \hat{x}^2]. \quad (3.6)$$

A quadratic term $(\hbar\omega/2)\mu^2 D_x^2$ term was added to give the feedback Hamiltonian a ground state energy of $\hbar\omega/2$, as with the other protocols. Even though this shift is feedback-dependent, it does not change the physical behavior of the system. We will refer to this strategy as Protocol C, cross-feedback, to differentiate it from the usual cold damping scheme. The dimensionless constant μ regulates the force exerted on the particle.

3.2.3 Quantum Fokker-Planck Master Equation

We now describe how we model these protocols. Many studies of continuous measurement and feedback have focused on quantum Brownian models and stochastic equations [83, 116, 142, 144, 152–157], and these usually start with the Belavkin equation [66, 67, 84, 86–88, 131] for a continuous monitored system:

$$d\hat{\rho} = -\frac{i}{\hbar}[\hat{H}, \hat{\rho}]dt + \sum_j \lambda_j \mathcal{D}[\hat{A}_j]\hat{\rho}dt + \sqrt{\lambda_j} dW_j \{\hat{A}_j - \langle \hat{A}_j \rangle, \hat{\rho}\}. \quad (3.7)$$

The index j runs over the measured observables $(\hat{A}_1, \hat{A}_2, \dots)$. And the variables λ_j correspond to the strength of the j 'th measurement. The variables dW_j are Wiener increments and satisfy $dW_i dW_j = \delta_{ij} dt$ [75]. In this chapter, we consider that the evolution of Eq. (3.7) is coupled to a finite bandwidth measurement signal that evolves similarly to D_x in Eq. (3.2):

$$dD_j = \gamma_j (\langle \hat{A}_j \rangle - D_j) dt + \frac{\gamma_j}{\sqrt{4\lambda_j}} dW_j. \quad (3.8)$$

The variables $\mathbf{D} = (D_1, D_2, \dots)$ were introduced in Ref. [1] to model a finite bandwidth measurement detector. These variables relax to the expected value of the measured operator, where γ_j is the bandwidth of the j 'th detector and $\gamma_j/\sqrt{4\lambda_j}$ determines the size of the noise in the detector. The finite bandwidth in the measurement signal is experimentally motivated, and it allows for nonlinear feedback to be applied by varying the Hamiltonian based on the measurement outcome $\hat{H} = \hat{H}(\mathbf{D})$. We note that without the filtering, only linear feedback can be considered due to the white noise in the unfiltered measurement outcome [80]. While the nonlinear term in our feedback protocols is a fluctuating constant, it is necessary to describe the cooling protocols in terms of moving the potential.

Here, we are interested in deriving analytical results. To this end, we employ the recently derived Quantum Fokker-Planck Master Equation [1] (see Sec. 2.4), which is obtained by averaging the Belavkin equation (3.7) over all possible realizations of dW_j , singling out the latest observed measurement outcome (3.8) - for a derivation for multiple measurements, see Appendix 3B. This formalism is similar to the hybrid quantum-classical master equations derived in [158, 159].

The Quantum Fokker-Planck master equation [1], extended here to measurements of mul-

tuple observables is:

$$\begin{aligned} \partial_t \hat{\rho}(\mathbf{D}, t) = & \\ & - \frac{i}{\hbar} \left[\hat{H}(\mathbf{D}), \hat{\rho}(\mathbf{D}, t) \right] + \sum_j \lambda_j \mathcal{D}[\hat{A}_j] \hat{\rho}(\mathbf{D}, t) + \sum_j \left[-\gamma_j \partial_{D_j} \mathcal{A}_j \hat{\rho}(\mathbf{D}, t) + \frac{\gamma_j^2}{8\lambda_j} \partial_{D_j}^2 \hat{\rho}(\mathbf{D}, t) \right], \end{aligned} \quad (3.9)$$

The index j runs over the measured observables $(\hat{A}_1, \hat{A}_2, \dots)$ and associated detector variables $\mathbf{D} = (D_1, D_2, \dots)$, and $\hat{\rho}(\mathbf{D}, t)$ is the joint state for the quantum system and the classical detector variables \mathbf{D} .

The first term on the right side of Eq. (3.9) generates unitary evolution under $\hat{H}(\mathbf{D})$. The second term represents the measurement backaction, and λ_j denotes the strength of the j 'th measurement. The superoperator $\mathcal{D}[\hat{c}] \hat{\rho} \equiv \hat{c} \hat{\rho} \hat{c}^\dagger - \frac{1}{2} \hat{c}^\dagger \hat{c} \hat{\rho} - \frac{1}{2} \hat{\rho} \hat{c}^\dagger \hat{c}$ is the dissipator, where \hat{c} is an arbitrary operator. The third term, representing the system-detector coupling, describes the drift of each measurement outcome D_j toward a value determined by the system state and the measured operator \hat{A}_j . Here, $\mathcal{A}_j \hat{\rho} \equiv \frac{1}{2} \{ \hat{A}_j - D_j, \hat{\rho} \}$, where $\{ \cdot, \cdot \}$ denotes the anti-commutator. The fourth term represents the diffusion of D_j due to measurement noise, where $\gamma_j/8\lambda_j$ determines the magnitude of the noise. The constant γ_j represents the j 'th detector bandwidth, hence γ_j^{-1} is the detector delay. See Chapter 2 for the derivation and a more detailed discussion of the QFPME.

Since $\hat{\rho}(\mathbf{D}, t)$ is a hybrid distribution over the combined spaces of the quantum system and the classical detector, expectation values are calculated jointly over these spaces:

$$\langle \hat{f}(\mathbf{D}) \rangle(t) = \int d\mathbf{D} \text{Tr} \left[\hat{f}(\mathbf{D}) \hat{\rho}(\mathbf{D}, t) \right], \quad (3.10)$$

where $\hat{f}(\mathbf{D})$ is a \mathbf{D} -dependent operator representing an observable of interest. We will focus on

the evolution of such expectation values rather than attempting to solve Eq. (3.9) for $\hat{\rho}(\mathbf{D}, t)$.

3.3 Results

In the following sections, we apply Eq. (3.9) to the protocols described by Eqs. (3.4-3.6).

In order to focus on the cooling and trapping produced by these protocols, we present the main results below, leaving technical details of their derivations to Appendices.

3.3.1 Protocol X: position measurement

Protocol X, defined by Eq. (3.4) for $\hat{H}_x(D_x)$, involves continuous measurement of position.

The joint state $\hat{\rho}(D_x, t)$ obeys (see Eq. (3.9))

$$\partial_t \hat{\rho} = -\frac{i}{\hbar} [\hat{H}_x, \hat{\rho}] + \lambda \mathcal{D}[\hat{x}] \hat{\rho} - \frac{\gamma}{2} \partial_{D_x} \{ \hat{x} - D_x, \hat{\rho} \} + \frac{\gamma^2}{8\lambda} \partial_{D_x}^2 \hat{\rho}. \quad (3.11)$$

For simplicity, we omit the subscript x in the parameters γ and λ . This protocol is the quantum analog of the protocol discussed in Sec. 3.2.1. Derivations of the results presented here are found in Appendix 3C.

3.3.1.1 Energy and trapping

Using Eqs. (3.10) and (3.11), we find that to solve for the expectation value of the feedback Hamiltonian $\hat{H}_x(D_x)$ we must solve a system of six coupled linear differential equations. The system can be simplified to three coupled equations in the case $b = 1$, as discussed in Appendix

3C. From the fixed point of this set of equations, we find that the energy relaxes to

$$\langle \hat{H}_x \rangle_\infty = \frac{\hbar\omega}{2} \left[\frac{\lambda}{b\gamma} + \frac{b\gamma}{4\lambda} + \frac{(2-b)\gamma\lambda}{2b\omega^2} \right]. \quad (3.12)$$

A numerical verification of Eq. (3.12) for $b = 1$ is shown in Fig. 3.2a. We also find, from the same fixed point, that the position variance $\sigma_x^2 \equiv \langle \hat{x}^2 \rangle - \langle \hat{x} \rangle^2$ relaxes to

$$\sigma_{x,\infty}^2 = \frac{1}{2} \left[\frac{\lambda}{b\gamma} + \frac{b\gamma}{4(1-b)\lambda} + \frac{\gamma\lambda}{b(1-b)\omega^2} \right]. \quad (3.13)$$

This variance diverges when $b \rightarrow 1$, indicating that the protocol does not trap the particle at the origin. Intuitively, when $b = 1$ there is no restoring force pushing the values of $\langle x \rangle$ and $\langle D_x \rangle$ toward the origin. Rather, due to the underlying measurement noise, the particle and the detector together perform unbiased Brownian motion.

The timescale for the system to relax to its asymptotic state is determined from the eigenvalues of the matrix in Eq. (3.A11). While we do not have a general, analytical expression for these eigenvalues, in two specific regimes the relaxation rate χ simplifies considerably:

$$b = 1, \gamma < 2\omega \quad \Rightarrow \quad \chi = \gamma, \quad (3.14)$$

$$\omega \gg \gamma \quad \Rightarrow \quad \chi = \gamma b. \quad (3.15)$$

If b is small, the protocol is being applied weakly, and the relaxation is slow.

3.3.1.2 Optimal regime and fine-tuning

To optimize the protocol, we can choose values of b that minimize either the energy or the position variance, depending on whether we prioritize cooling or trapping.

We minimize the asymptotic energy by setting

$$b = b_e = 2\lambda \sqrt{\frac{1}{\omega^2} + \frac{1}{\gamma^2}}. \quad (3.16)$$

Note that this solution is valid only when $b_e < 1$.

The position variance is minimized by setting

$$b = b_v = \left(1 + \frac{\gamma}{2\lambda} \sqrt{\frac{4\lambda^2 + \omega^2}{\gamma^2 + \omega^2}}\right)^{-1}. \quad (3.17)$$

For $\omega \gg \gamma \gg \lambda$ and $b = b_v$ (note that in this regime $b_v \simeq b_e$), we obtain

$$\sigma_{x,\infty}^2 = \frac{1}{2} \left(1 + \frac{\lambda}{\gamma} + \frac{\gamma^2}{2\omega^2}\right) + \mathcal{O}(\gamma\lambda/\omega^2) \quad (3.18)$$

$$\langle \hat{H}_x \rangle_\infty = \frac{\hbar\omega}{2} \left(1 + \frac{2\lambda^2}{\gamma^2} + \frac{\gamma^2}{2\omega^2}\right) + \mathcal{O}(\gamma\lambda/\omega^2). \quad (3.19)$$

This result shows that trapping and cooling can be achieved simultaneously, to arbitrary accuracy.

In this regime, the feedback is weak ($b \ll 1$) and the relaxation occurs slowly.

3.3.2 Protocol XP: position and momentum measurements

In Protocol XP, the feedback uses weak measurements of both position and momentum.

The feedback Hamiltonian is thus parametrized by D_x and D_p (see Eq. (3.5)).

For this protocol the QFPME for $\hat{\rho}(\mathbf{D}, t)$ is

$$\partial_t \hat{\rho} = -\frac{i}{\hbar} \left[\hat{H}_{xp}, \hat{\rho} \right] + \lambda_x \mathcal{D}[\hat{x}] \hat{\rho} + \lambda_p \mathcal{D}[\hat{p}] \hat{\rho} + \gamma_x \mathcal{F}_x \hat{\rho} + \gamma_p \mathcal{F}_p \hat{\rho}, \quad (3.20)$$

where $\mathcal{F}_i \hat{\rho} = -(1/2) \partial_{D_i} \{ \hat{i} - D_i, \hat{\rho} \} + (\gamma_i / 8 \lambda_i) \partial_{D_i}^2 \hat{\rho}$ and $i = x, p$. The detector bandwidths γ_i and measurement strengths λ_i characterize the measurement devices. For simplicity, we set $\lambda_x = \lambda_p = \lambda$ and $\gamma_x = \gamma_p = \gamma$.

3.3.2.1 Energy and trapping

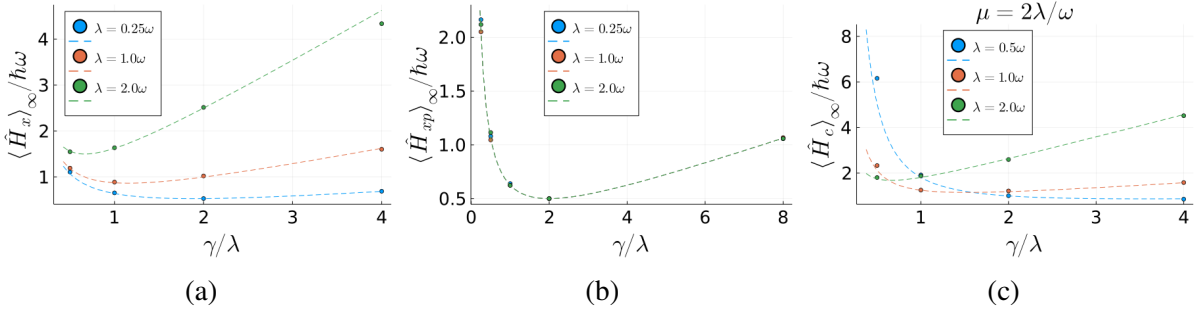


Figure 3.2: Comparison of analytical formulas (dashed lines) to numerical results (circles). We chose $b = 1$ for Protocols X and XP for simplicity. The average asymptotic energy was calculated using 1000 runs of the stochastic equations for (a) Protocol X for different values of measurement strength. (b) Protocol XP for different values of measurement strength. Here, we can see that the energy only depends on the ratio γ/λ . The non-monotonic energy behavior as a function of γ/λ for both Protocols X and XP can be explained by the competition between the noise sources. See Sec. 3.4 for a detailed discussion. (c) Cross-feedback protocol, where we chose $\mu = 2\lambda/\omega$. Note that this plot illustrates that we need $\gamma \gg \omega \gg \lambda$ to achieve maximum cooling.

As in Sec. (3.3.1), we derive asymptotic solutions for the average energy $\langle \hat{H}_{xp} \rangle_\infty$ and po-

sition variance $\sigma_{x,\infty}^2$ (see Appendix 3D for details):

$$\langle \hat{H}_{xp} \rangle_{\infty} = \frac{\hbar\omega}{2} \left[\frac{\lambda}{b\gamma} + \frac{b\gamma}{4\lambda} + \frac{(1-b)\gamma\lambda}{2\omega^2} \right] \quad (3.21)$$

$$\sigma_{x,\infty}^2 = \frac{1}{2} \left[\frac{\lambda}{b\gamma} + \frac{b\gamma}{4(1-b)\lambda} + \frac{\gamma\lambda}{b(1-b)\omega^2} \right]. \quad (3.22)$$

These solutions were derived from the fixed point of a system of four coupled differential equations. Note that the position variance is the same for Protocols X and XP.

As with Protocol X, the variance in position diverges when $b \rightarrow 1$. This occurs because $\langle \hat{x} \rangle_{\infty} = 0 = \langle D_x \rangle_{\infty}$ is no longer a stable fixed point, and the particle diffuses in space much like a Brownian particle. Figure 3.2b presents a numerical verification of Eq. (3.21) for $b = 1$.

The relaxation rate to asymptotic values in Eqs. (3.21) and (3.22) is given by the smallest eigenvalue of the 4×4 matrix in Eq. (3.A17):

$$\chi = \min \Re \left(\gamma \pm \frac{\Delta_{\pm}}{\sqrt{2}} \right), \quad (3.23)$$

with

$$\Delta_{\pm} = \sqrt{-\omega^2 + \gamma^2 \pm \Omega} \quad (3.24)$$

$$\Omega = \sqrt{\omega^4 + 2(1 - 8b + 8b^2)\omega^2\gamma^2 + \gamma^4}.$$

In two regimes, the relaxation rate χ simplifies as follows:

$$b = 1 \quad \Rightarrow \quad \chi = 2\gamma, \quad (3.25)$$

$$\omega \gg \gamma \quad \Rightarrow \quad \chi = 2\gamma b. \quad (3.26)$$

Compare with Eqs. (3.14) and (3.15). As with Protocol X, this protocol becomes slow as the feedback weakens in the limit $b \rightarrow 0$. Note that, using two measurements, the relaxation timescale is twice as fast as Protocol X.

3.3.2.2 Optimal protocol

Because the energy and variance solutions for Protocol XP (Eqs. (3.21), (3.22)) are similar to the ones found in Protocol X (Eqs. (3.12), (3.13)), the optimal parameter choices and the associated asymptotic position variance and energy values are the same for both protocols, up to $\mathcal{O}(\gamma\lambda/\omega^2)$.

The asymptotic energy for Protocol XP is smaller than the one achieved by Protocol X by a term $\hbar\omega\gamma\lambda/4\omega^2$. This is important because if one is not interested in trapping the particle, then the choices $b = 1$ and $\gamma = 2\lambda$ achieve ground-state cooling arbitrarily fast (see Appendix 3D):

$$\langle \hat{H}_{xp} \rangle_{\infty} = \frac{\hbar\omega}{2}. \quad (3.27)$$

This protocol is able to cool down the particle to the ground state because the symmetric measurement of position and momentum can saturate the uncertainty relation. The presence of a low-pass filter can rectify the noisy signal and keep the particle at the bottom of the harmonic potential if $\gamma = 2\lambda$; see Sec.3.4 for a detailed discussion.

3.3.3 Protocol C: Cross feedback

Next, we consider the third protocol, with $\hat{H}_c(D_x)$ defined by Eq. (3.6). Here, measurements performed on the particle's position are translated into feedback applied to its momentum,

and the QFPME is

$$\partial_t \hat{\rho} = -\frac{i}{\hbar} [\hat{H}_c, \hat{\rho}] + \lambda \mathcal{D}[\hat{x}] \hat{\rho} + \gamma \mathcal{F}_x \hat{\rho} \quad (3.28)$$

3.3.3.1 Energy and trapping

The relevant quantities to solve for the asymptotic energy using the QFPME are determined by six coupled linear ODEs, see Appendix 3E.

Because of the lack of symmetries in the problem, we could not solve for the eigenvalues of the matrix in Eq. (3.A24). As a result, for an arbitrary choice of parameters $(\omega, \lambda, \gamma, \mu)$, we do not know when the system converges asymptotically to a fixed value. However, if the solution does converge, then the asymptotic energy with respect to the Hamiltonian in Eq. (3.6) is:

$$\langle \hat{H}_c \rangle_\infty = \frac{\hbar\omega}{2} \left(\frac{\mu\omega}{4\lambda} + \frac{\lambda}{\mu\omega} + \frac{\lambda}{2\gamma} + \frac{\lambda\omega}{\gamma^2\mu} + \frac{\gamma\mu^2}{8\lambda} \right). \quad (3.29)$$

We plot a numerical verification of Eq. (3.29) for $\mu = 2\lambda/\omega$ in Fig. 3.2c.

The position variance can also be obtained from the asymptotic solution, see Eq. (3.A35):

$$\sigma_{x,\infty}^2 = \frac{1}{2} \left(\frac{\mu\omega}{4\lambda} + \frac{\lambda}{\mu\omega} + \frac{\lambda\omega}{\gamma^2\mu} \right). \quad (3.30)$$

We see that this protocol is able to trap the particle (i.e. $\sigma_{x,\infty}^2$ is finite) for all positive values of μ , in contrast with the other two protocols that required $b < 1$ to achieve trapping.

3.3.3.2 Optimal protocol

We can verify from Eq. (3.29) that no choice of parameters produces ground-state cooling. Finding the values of μ , λ , γ and ω that minimize $\langle \hat{H}_c \rangle_\infty$ is difficult, but if we assume $1 \gg \omega/\gamma \gg \lambda/\omega, \mu$ then the value of μ that minimizes the asymptotic energy is

$$\mu^* = 2\lambda/\omega \ll 1, \quad (3.31)$$

leading to

$$\langle \hat{H}_c \rangle_\infty = \frac{\hbar\omega}{2} \left(1 + \frac{\lambda\gamma}{2\omega^2} + \frac{\omega^2}{2\gamma^2} \right) + \mathcal{O}(\lambda/\gamma) \quad (3.32)$$

For small μ , the system's relaxation timescale is $\mu\omega$, to $\mathcal{O}(\mu)$ (see Eq. (3.A27)), which under optimal cooling conditions is given by $\mu^*\omega = 2\lambda$.

As with the other protocols, the optimal condition for cooling is the same as the optimal condition for trapping. Here, using $\mu = 2\lambda/\omega$, we have

$$\sigma_{x,\infty}^2 = \frac{1}{2} \left(1 + \frac{\omega^2}{2\gamma^2} \right) \quad (3.33)$$

in dimensionless units.

3.3.4 Coupling to a thermal bath

The above calculations were performed for a closed quantum system under continuous measurement and feedback. We now consider the case in which the system is open. Specifically, it is coupled to a thermal environment as it simultaneously undergoes measurement and feedback.

The environment's presence is modeled by adding Lindblad jump terms,

$$\Gamma(\bar{n} + 1)\mathcal{D}[\hat{a}_i]\hat{\rho}(\mathbf{D}) + \Gamma\bar{n}\mathcal{D}[\hat{a}_i^\dagger]\hat{\rho}(\mathbf{D}), \quad (3.34)$$

to the QFPME for each protocol. Here Γ denotes the system-bath coupling strength, and $\bar{n} = (e^{\beta\hbar\omega} - 1)^{-1}$ controls the asymptotic average energy the system would relax to, in the absence of feedback control:

$$U_{\text{th}} = \hbar\omega(\bar{n} + 1/2). \quad (3.35)$$

The operators \hat{a}_i (\hat{a}_i^\dagger) with $i = \{x, xp, c\}$ are the annihilation (creation) operators:

$$\hat{a}_x = \sqrt{1/2}(\hat{x} - D_x + i\hat{p}), \quad (3.36)$$

$$\hat{a}_{xp} = \sqrt{1/2}(\hat{x} - D_x + i\hat{p} - iD_p), \quad (3.37)$$

$$\hat{a}_c = \sqrt{1/2}(\hat{x} + i\hat{p} - i\mu D_x). \quad (3.38)$$

Here, we focus on Protocols X and XP when $b = 1$, as the general case $b \neq 1$ is cumbersome and not particularly insightful.

The operators $\{\hat{a}_i\}$ satisfy $[\hat{H}_i, \hat{a}_i] = -\hbar\omega\hat{a}_i$ for $i \in \{x, xp, c\}$, hence the effect of the bath is to create and destroy single quanta of energy in the measurement-outcome-dependent energy basis.

Let us assume the following constraints for each protocol: a) Protocol X, $\omega \gg \gamma, \lambda, \Gamma$; b) Protocol XP, no constraints; c) Protocol C, $\gamma \gg \omega \gg \mu\gamma, \lambda\gamma/\omega, \Gamma\gamma/\omega$. We can then write the

asymptotic energy as a weighted average,

$$\langle \hat{H}_i \rangle_\Gamma = \frac{\Gamma_i \langle \hat{H}_i \rangle_\infty + \Gamma U_{\text{th}}}{\Gamma_i + \Gamma}, \quad (3.39)$$

where $i = \{x, xp, c\}$. The weight factors Γ_i are:

$$\Gamma_x = \gamma, \quad (3.40)$$

$$\Gamma_{xp} = 2\gamma, \quad (3.41)$$

$$\Gamma_c = \mu\omega, \quad (3.42)$$

Equation (3.39) expresses the asymptotic energy as a weighted average of the feedback energy and the thermal energy, where the weights are the protocols' relaxation rates (close to their optimal conditions) and the thermal bath's relaxation rate. This weighted average reflects a competition between the bath, which tries to bring the system to thermal equilibrium, and the measurement and feedback protocol, which tries to minimize the system's energy. In the absence of measurement and feedback, Γ represents the relaxation rate to thermal equilibrium. When measurement and feedback are present, but $\gamma, \lambda, \mu\omega \ll \Gamma$, then the effects of the bath are dominant and the system's asymptotic energy is close to the thermal equilibrium energy. Conversely, if $\gamma, \lambda, \mu\omega \gg \Gamma$, then the system is stabilized near the solution given by the asymptotic average energy of a closed system. Thus, thermal coupling imposes an additional requirement, namely $\gamma, \lambda, \mu\omega \gg \Gamma$, that must be satisfied to maximize cooling.

3.4 Trajectory simulation

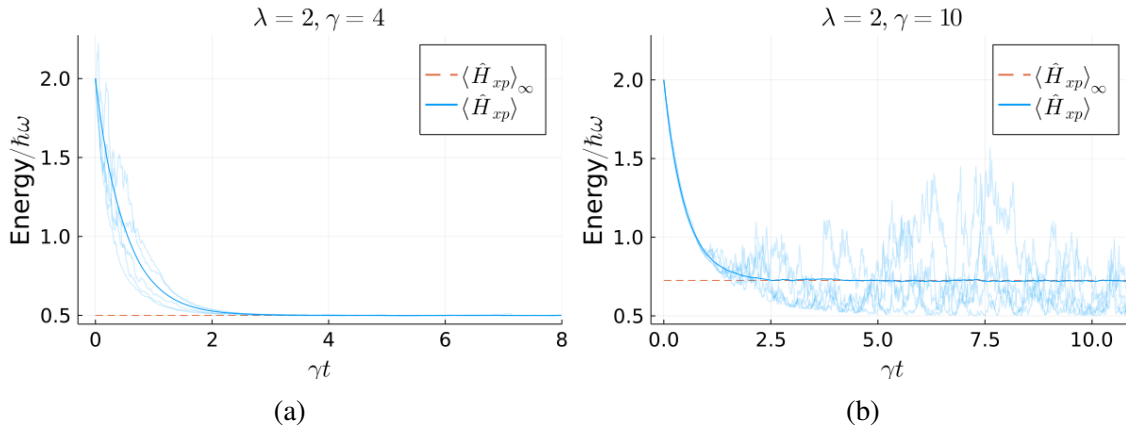


Figure 3.3: Single trajectory simulation for Protocol XP ($b = 1$). Here, we plot 5 trajectories (light blue lines) and the average energy for 2000 trajectories (blue line). The trajectory energy, in general, only converges with the analytical result (dashed line) in the ensemble sense. See Sec. 3.4 for simulation details. (a) Single trajectory simulation for Protocol XP with ground state cooling ($\gamma = 2\lambda$). The energy initially evolves stochastically, but after the variances have decayed to their asymptotic values, the energy evolution becomes deterministic, producing ground-state cooling at the trajectory level. (b) Here, the protocol applied is not at the ground-state condition ($\gamma \neq 2\lambda$). Note that the individual trajectories don't necessarily converge to a fixed energy value, but the ensemble average converges to the analytical result derived in Eq. (3.21).

Here, we describe numerical simulations of stochastic trajectories that were used both to test the analytical results of Sec. 3.3, and to build trajectory-level intuition about the ground state cooling described in Sec. 3.3.2.2. The quantities described in this section are the noisy counterparts of the quantities discussed in previous sections.

Our starting point is the Belavkin Equation (3.7) with $\hat{A}_1 = \hat{x}$ and $\hat{A}_2 = \hat{p}$, coupled with

the evolution of the measurement outcome:

$$d\hat{\rho} = -\frac{i}{\hbar}[\hat{H}(\mathbf{D}), \hat{\rho}]dt + \lambda_x \mathcal{D}[\hat{x}]\hat{\rho}dt + \sqrt{\lambda_x}dW_x\{\hat{x} - \langle\hat{x}\rangle, \hat{\rho}\} \quad (3.43)$$

$$+ \lambda_p \mathcal{D}[\hat{p}]\hat{\rho}dt + \sqrt{\lambda_p}dW_p\{\hat{p} - \langle\hat{p}\rangle, \hat{\rho}\},$$

$$dD_i = \gamma_i(\langle\hat{i}\rangle - D_i) + \frac{\gamma_i}{\sqrt{4\lambda_i}}dW_i, \quad i = x, p. \quad (3.44)$$

Equations (3.43) and (3.44) describe the coupled, stochastic dynamics of the system $\hat{\rho}$ and measurement outcomes D_i . Equation (3.43) is the Belavkin equation, which generalizes the Schrödinger equation to continuously monitored systems. The Belavkin equation relates the infinitesimal stochastic evolution of the density matrix to the unitary evolution, backaction, and random update based on the stochastic outcome of the measurement. Equation (3.44) describes the noisy relaxation of the detector variables D_x and D_p toward the average position and momentum $\langle\hat{x}\rangle$ and $\langle\hat{p}\rangle$.

Together, Eqs. (3.43) and (3.44) are the single-trajectory counterparts of the QFPME, Eq. (3.9), which describes the combined evolution at the ensemble level. Equation (3.43) gives rise to the unitary part and the backaction terms in Eq. (3.9) while Eq. (3.44) generates the Fokker-Planck component of the QFPME.

In Eq. (3.43), the system's Hamiltonian has the general quadratic form

$$\hat{H}(\mathbf{D}) = \frac{\hbar\omega}{2} [(\hat{p} - b_x D_x - b_p D_p)^2 + (\hat{x} - c_x D_x - c_p D_p)^2], \quad (3.45)$$

which can reproduce all the protocols introduced and investigated in Sec. 3.2 and 3.3.

Protocol	Regime	Timescale	Energy	Position Variance
X	$\omega \gg \gamma \gg \lambda$	γb	$\frac{\hbar\omega}{2} \left(\frac{\lambda}{b\gamma} + \frac{b\gamma}{4\lambda} \right)$	$\frac{1}{2} \left(\frac{\lambda}{b\gamma} + \frac{b\gamma}{4(1-b)\lambda} \right)$
XP	$\gamma = 2\lambda, \quad b = 1$	2γ	$\frac{\hbar\omega}{2}$	∞
	$\omega \gg \gamma \gg \lambda$	$2\gamma b$	$\frac{\hbar\omega}{2} \left(\frac{\lambda}{b\gamma} + \frac{b\gamma}{4\lambda} \right)$	$\frac{1}{2} \left(\frac{\lambda}{b\gamma} + \frac{b\gamma}{4(1-b)\lambda} \right)$
C	$\gamma \gg \omega \gg \lambda\gamma/\omega$	$\mu\omega$	$\frac{\hbar\omega}{2} \left(\frac{\mu\omega}{4\lambda} + \frac{\lambda}{\mu\omega} \right)$	$\frac{1}{2} \left(\frac{\mu\omega}{4\lambda} + \frac{\lambda}{\mu\omega} \right)$

Table 3.1: Performance of different protocols under optimal conditions. The column Regime denotes the hierarchy resulting in optimal conditions. The column Timescale shows the relaxation rate to the asymptotic value. The column Energy represents the asymptotic energy achieved. The column Position Variance shows the variance obtained after trapping the particle. Note the special condition for ground-state cooling that can only be achieved by Protocol XP. The optimal choice for parameters to achieve near ground-state cooling are $b = 2\lambda/\gamma$ and $\mu = 2\lambda/\omega$.

Under Eq. (3.43), the evolution of $\langle \hat{x} \rangle$, $\langle \hat{p} \rangle$ and higher cumulants (such as variances) is described by a set of infinitely many coupled equations. As discussed in Appendix 3G, if we assume an initial Gaussian wave function for the state of the system [69, 81, 160], then the system's state remains Gaussian at all times. The system's evolution is then uniquely defined by the evolution of the first two sets of cumulants, allowing us to write a closed set of SDEs for these cumulants and the detector variables D_x and D_p ; see Eq. (3.A41). We have numerically simulated trajectories evolving under these coupled SDEs, and by averaging over these trajectories, we have calculated the asymptotic energy values $\langle H \rangle_\infty$ for various protocols. Figure 3.2 shows good agreement between these numerically obtained values and the analytical results derived in Sec. 3.3.

The trajectory approach also provides insight into how Protocol XP achieves ground-state cooling for $b = 1$ and $\gamma = 2\lambda$ in Eq. (3.21). Using $b_x = c_p = 0$ and $b_p = c_x = 1$ in Eq. (3.45), when we choose $\lambda_x = \lambda_p = \lambda$ the system evolves asymptotically to a symmetric Gaussian with variances (see Eq. (3.A43))

$$(V_x)_\infty = (V_p)_\infty = \frac{1}{2}. \quad (3.46)$$

Note that these quantities differ from the previously discussed position variance. Here, they refer to the actual wave function position variance at the trajectory level. Conversely, the results shown before refer to the ensemble average position variance over many realizations of the experiment.

After the variances decay, the stochastic equation for the average energy $d\langle\hat{H}_{xp}\rangle = d\text{Tr}\left[\hat{H}_{xp}\hat{\rho}\right]$, using Eq. (3.43), can be simplified using $\gamma_x = \gamma_p = \gamma$:

$$\begin{aligned} d\langle\hat{H}_{xp}\rangle = & 2\gamma \left(\langle\hat{H}_{xp}\rangle_{\infty} - \langle\hat{H}_{xp}\rangle \right) dt \\ & + \hbar\omega \left(\langle\hat{x}\rangle - D_x \right) \left(1 - \frac{\gamma}{2\lambda} \right) \sqrt{\lambda} dW_x \\ & + \hbar\omega \left(\langle\hat{p}\rangle - D_p \right) \left(1 - \frac{\gamma}{2\lambda} \right) \sqrt{\lambda} dW_p. \end{aligned} \quad (3.47)$$

When $\gamma = 2\lambda$, the stochastic terms vanish and Eq. (3.47) reduces to exponential cooling to the ground state. See Fig. 3.3 for a comparison of how the energy evolves for a) $\gamma = 2\lambda$ and b) $\gamma \neq 2\lambda$.

It is also instructive to look at the SDE's for $\langle\hat{x}\rangle$, $\langle\hat{p}\rangle$, D_x and D_p (see Eq. (3.A41), with parameters set as in the previous paragraph), which combine to give

$$\begin{aligned} dX &= (-\gamma X + \omega P) dt + \left(\sqrt{\lambda} - \frac{\gamma}{\sqrt{4\lambda}} \right) dW_x, \\ dP &= (-\gamma P - \omega X) dt + \left(\sqrt{\lambda} - \frac{\gamma}{\sqrt{4\lambda}} \right) dW_p, \end{aligned} \quad (3.48)$$

for the quantities $X = \langle\hat{x}\rangle - D_x$ and $P = \langle\hat{p}\rangle - D_p$. The coefficient multiplying the Wiener increments dW_x and dW_p reflects a trade-off between contributions from the noise on the system's dynamics due to measurements, and the noise on the detector outcome. The former is proportional to $\sqrt{\lambda}$ (Eq. (3.43)) reflecting the fact that increased measurement backaction leads to increased noise; the latter is proportional to $\gamma/\sqrt{4\lambda}$ (Eq. (3.44)), reflecting both the detector

bandwidth γ , and the fact that the increased measurement strength λ leads to more precise (less noisy) measurement outcomes. When $\gamma = 2\lambda$ these contributions cancel in Eq. (3.48), and the resulting deterministic equations have the asymptotic solution

$$X_\infty = 0 \quad , \quad P_\infty = 0. \quad (3.49)$$

Eqs. (3.46) and (3.49) describe the ground state of a harmonic oscillator whose minimum is located at the origin.

We emphasize that although in this section we assumed an initial Gaussian state for the system, the derivations in previous sections did not impose this restriction: the asymptotic solutions derived from the QFPME are independent of initial conditions.

3.5 Discussion

The results discussed in previous sections allow us to compare the three protocols on an equal footing. Each protocol has strengths and weaknesses that will affect the protocol choice for particular implementations. The level of control in the experiment plays a vital role in determining the success of this approach; the measurement operators and the range of values of the parameters are the primary factors in deciding which protocol to use.

The optimal protocols discussed in the previous sections are summarized in Table 3.1. All protocols can trap and cool down the particle for suitable choices of parameters. Protocol XP can quickly cool the particle to the ground state if no trapping is necessary. Protocol C can trap the particle close to the minimum uncertainty with a quadratic correction, as opposed to a linear correction from Protocols X and XP (compare Eq. (3.30) to Eq. (3.13) and Eq (3.22), in their

optimal conditions).

The physical implementation and range of parameters are essential to decide which protocol to use. Note that the frequency is the largest parameter for protocols X and XP, while for protocol C, the bandwidth is the largest parameter. This can play an essential role in which protocols can be implemented. For Protocol X, measurement and feedback are performed in the position basis. For Protocol XP, we require both measurement and feedback in both position and momentum, and Protocol C requires measurement in position and feedback in momentum. In experiments, the choice of protocols can also be affected by which observables can be measured.

Overall, if we measure only a single variable (position or momentum), then Protocol C outperforms Protocol X for trapping; however, a larger separation of timescales is necessary $\gamma \gg \omega \gg \lambda\gamma/\omega$. If position and momentum measurements are feasible and there is no need for trapping, then Protocol XP gives the best result for fast ground state cooling. In all protocols, if the system is not isolated from a thermal environment, the cooling rate must be larger than the thermal relaxation rate to mitigate the heating effects of the thermal bath.

3.6 Conclusion

We have studied cooling protocols using a recently derived framework for continuous measurement and feedback. We applied the Quantum Fokker-Planck Master equation [1] to a quantum harmonic oscillator that serves as a simple but relevant system for ground state cooling techniques. Unlike previous studies on measured harmonic oscillators [142, 152], our model includes a finite detector bandwidth, which has proven to be a central ingredient for achieving ground state cooling.

We focused our study on three different measurement schemes: position measurement (X), position and momentum measurement (XP), and the cross-feedback protocol (C) which is related to cold damping. We showed that Protocol XP yields better results for the cooling task, and cooling can be done arbitrarily fast compared to a single measurement in position. Also, no separation of timescale needs to be satisfied (other than $\gamma \gg \Gamma$ to avoid thermal excitation).

Our main results are analytical expressions for the asymptotic energy achieved by these schemes and the emergence of optimum parameters to trap and cool the system. Feedback schemes are usually complex to solve; thus, our framework uncovers some techniques and tools that could be employed to solve more complicated systems. Future work will include an in-depth study of the thermodynamics of the QFPME, more general feedback protocols, and possible experimental verification of results.

Another interesting avenue for investigation is the squeezing effect that can happen due to continuous feedback [156]. Although this question is out of the scope of this chapter, it can help answer the question of which interesting quantum states can be prepared using continuous feedback.

3A Feedback cooling in a classical oscillator

Here, we present details of the analysis of the classical model discussed in Sec. 3.2.1 of the main text.

3A.1 Discrete time feedback

Letting $(x_k, p_k) \equiv (x(k\Delta t), p(k\Delta t))$ denote the particle's state at stroboscopic times $k\Delta t$, $k = 0, 1, 2, \dots$, the evolution from one step to the next is given by the linear map

$$\begin{pmatrix} x_{k+1} \\ p_{k+1} \end{pmatrix} = \begin{pmatrix} b + (1-b)\cos(\omega\Delta t) & \sin(\omega\Delta t)/m\omega \\ -m\omega(1-b)\sin(\omega\Delta t) & \cos(\omega\Delta t) \end{pmatrix} \begin{pmatrix} x_k \\ p_k \end{pmatrix}. \quad (3.A1)$$

We assume Δt is not an integer multiple of π/ω . The particle's long-time evolution is determined by the eigenvalues of the above matrix. When $b < 1$, the magnitudes of both eigenvalues are smaller than unity, and the state vector (x_k, p_k) decays to the unique stationary state $(0, 0)$ as $k \rightarrow \infty$, i.e. the particle is cooled and trapped at the origin. When $b > 1$, one eigenvalue's magnitude exceeds unity, hence for generic initial conditions, both x_k and p_k diverge exponentially with k . Finally, when $b = 1$, the matrix is easily diagonalized, and we obtain

$$x_k \rightarrow x_\infty = x_0 + \frac{\sin(\omega\Delta t)}{1 - \cos(\omega\Delta t)} \frac{p_0}{m\omega}, \quad p_k \rightarrow p_\infty = 0 \quad (3.A2)$$

as $k \rightarrow \infty$, thus the particle is cooled but not trapped at the origin.

3A.2 Continuous feedback

Defining $\zeta \equiv (x, p, D_x)^T$ and writing Eq. (3.2) as $\dot{\zeta} = M\zeta$, we see that the evolution of the particle's state (x, p) and its measured position D_x is governed by the matrix

$$M = \begin{pmatrix} 0 & 1/m & 0 \\ -m\omega^2 & 0 & m\omega^2 b \\ \gamma & 0 & -\gamma \end{pmatrix}. \quad (3.A3)$$

When $b < 1$, all eigenvalues of M have strictly negative real parts, which implies that the system evolves asymptotically to the state $\zeta_\infty = (0, 0, 0)$, corresponding to cooling and trapping at the origin. When $b > 1$, one of M 's eigenvalues has a positive real part, producing exponential divergence away from the origin; in this case, neither cooling nor trapping is achieved.

When $b = 1$, the eigenvalues of M are 0 and $\pm i\Omega$, where $\Omega = \sqrt{\omega^2 - \gamma^2/4}$. The explicit solution of Eq. (3.2), for initial conditions (x_0, p_0, D_{x0}) , is then:

$$p(t) = p_0 e^{-\gamma t/2} \cos(\Omega t) + \frac{1}{\Omega} \left[\frac{\gamma}{2} p_0 - m\omega^2 (x_0 - D_{x0}) \right] e^{-\gamma t/2} \sin(\Omega t), \quad (3.A4)$$

$$x(t) = x_0 + \left[\frac{\gamma p_0}{m\omega^2} - (x_0 - D_{x0}) \right] (1 - e^{-\gamma t/2} \cos(\Omega t)) + \quad (3.A5)$$

$$\left[\frac{p_0}{\Omega m\omega^2} (\Omega^2 - \gamma^2/4) + \frac{\gamma}{2\Omega} (x_0 - D_{x0}) \right] e^{-\gamma t/2} \sin(\Omega t),$$

$$D_x(t) = D_{x0} + \frac{\gamma p_0}{m\omega^2} (1 - e^{-\gamma t/2} \cos(\Omega t)) + \left[-\frac{\gamma p_0}{2m\omega^2} + (x_0 - D_{x0}) \right] \frac{\gamma}{\Omega} e^{-\gamma t/2} \sin(\Omega t).$$

$$(3.A6)$$

Asymptotically with time, $(x(t \rightarrow \infty) = x_\infty, D_x(t \rightarrow \infty) = D_{x,\infty}, p(t \rightarrow \infty) = p_\infty)$, this solu-

tion gives

$$x_\infty, D_{x,\infty} = D_{x0} + \frac{\gamma p_0}{m\omega^2}, \quad p_\infty = 0. \quad (3.A7)$$

Thus, the particle ends at rest at the bottom of the trap, but in general the trap is not located at the origin.

3B QFPME with multiple measurements

Here, we outline the steps used to derive the QFPME for two continuous measurements, Eq. (3.9). Similar steps hold for any finite number of measurements. This derivation is based on the stochastic calculus section of Supplemental Material on Ref. [1] and Appendix B of Ref. [68].

We start with the Belavkin equation for two measurements [69, 88]

$$\begin{aligned} d\hat{\rho}_c = & -\frac{i}{\hbar} [\hat{H}, \hat{\rho}_c] dt + \lambda_1 \mathcal{D}[\hat{A}_1] \hat{\rho}_c dt + \lambda_2 \mathcal{D}[\hat{A}_2] \hat{\rho}_c dt + \\ & \sqrt{\lambda_1} \{\hat{A}_1 - \langle \hat{A}_1 \rangle, \hat{\rho}_c\} dW_1 + \sqrt{\lambda_2} \{\hat{A}_2 - \langle \hat{A}_2 \rangle, \hat{\rho}_c\} dW_2, \end{aligned} \quad (3.A8)$$

where $\hat{\rho}_c$ is the density matrix conditioned on a particular stochastic trajectory for the outcome variables $D'_{1,2}$. The operators $\hat{A}_{1,2}$ are measurement operators, $\lambda_{1,2}$ are the corresponding measurement strengths, and $\langle \hat{A}_{1,2} \rangle = \text{Tr}(\hat{A}_{1,2} \hat{\rho}_c)$ are conditioned expected values. The stochastic variables $dW_{1,2}$ are Wiener processes that satisfy $dW_i dW_j = \delta_{ij} dt$ and $E[dW_{1,2}] = 0$. For brevity, we have suppressed the dependence of the Hamiltonian on the measurement outcomes $\hat{H} = \hat{H}(D'_1, D'_2)$ for the sake of notation. This equation is coupled to the evolution of the filtered measurement outcomes

$$dD'_i = \gamma_i \left(\langle \hat{A}_i \rangle - D'_i \right) dt + \frac{\gamma_i}{\sqrt{4\lambda_i}} dW_i, \quad i = 1, 2, \quad (3.A9)$$

where $\gamma_{1,2}$ are the detector bandwidths.

We are interested in the joint distribution of the system density matrix and detector outcomes $\hat{\rho}(D_1, D_2) = E_{W_1, W_2}[\hat{\rho}_c \delta(D_1 - D'_1) \delta(D_2 - D'_2)]$, where the average $E_{W_1, W_2}[\cdot]$ is taken over the noisy variables $W_{1,2}$. To obtain the equation of motion for this object, we use Ito's rules discussed in Sec. 1.5.3. Using these rules, we find that

$$\begin{aligned}
d[\hat{\rho}_c \delta(D_1 - D'_1) \delta(D_2 - D'_2)] &= d\hat{\rho}_c \delta(D'_1 - D_1) \delta(D'_2 - D_2) \\
&\quad + \hat{\rho}_c d\delta(D'_1 - D_1) \delta(D'_2 - D_2) + \hat{\rho}_c \delta(D'_1 - D_1) d\delta(D'_2 - D_2) \\
&\quad + d\hat{\rho}_c d\delta(D'_1 - D_1) \delta(D'_2 - D_2) + d\hat{\rho}_c \delta(D'_1 - D_1) d\delta(D'_2 - D_2).
\end{aligned} \tag{3.A10}$$

Note that the term $\hat{\rho}_c d\delta(D'_1 - D_1) d\delta(D'_2 - D_2)$ can be suppressed as it gives no contribution $\mathcal{O}(dt)$ because $E[dW_1 dW_2] = 0$. Now, one can use the identities in Eq. (2.29). Combining all these equations and taking the ensemble average of measurement outcomes, we obtain the QFPME with multiple measurements appearing in Eq. (3.9).

3C Protocol X: Position Measurement

To solve for the asymptotic expectation value of $\hat{H}_x(\mathbf{D})$, we first use Eq. (3.11) to write a set of coupled differential equations. In matrix form, these equations are:

$$\partial_t \begin{pmatrix} \nu_1 \\ \nu_2 \\ \nu_3 \\ \nu_4 \\ \nu_5 \\ \nu_6 \end{pmatrix} = \begin{pmatrix} -2\gamma b & 0 & \frac{\omega}{2} & -\gamma b(b-1) & 0 & 0 \\ 0 & 0 & -\frac{\omega}{2} & 0 & 0 & 0 \\ -4\omega & 4\omega & -\gamma b & 0 & 2\gamma b(1-b) & 0 \\ 2\gamma & 0 & 0 & -\gamma & \omega & \gamma b(1-b) \\ 0 & 0 & \frac{\gamma}{2} & -\omega & -\gamma(1-b) & 0 \\ 0 & 0 & 0 & 2\gamma & 0 & -2\gamma(1-b) \end{pmatrix} \begin{pmatrix} \nu_1 \\ \nu_2 \\ \nu_3 \\ \nu_4 \\ \nu_5 \\ \nu_6 \end{pmatrix} + \begin{pmatrix} \frac{b^2\gamma^2}{8\lambda} \\ \frac{\lambda}{2} \\ 0 \\ -\frac{b\gamma^2}{4\lambda} \\ 0 \\ \frac{\gamma^2}{4\lambda} \end{pmatrix}, \quad (3.A11)$$

where

$$\begin{pmatrix} \nu_1 \\ \nu_2 \\ \nu_3 \\ \nu_4 \\ \nu_5 \\ \nu_6 \end{pmatrix} \equiv \begin{pmatrix} \langle \frac{1}{2}(\hat{x} - bD_x)^2 \rangle \\ \langle \frac{1}{2}\hat{p}^2 \rangle \\ \langle \hat{p}(\hat{x} - bD_x) + (\hat{x} - bD_x)\hat{p} \rangle \\ \langle (\hat{x} - bD_x)D_x \rangle \\ \langle \hat{p}D_x \rangle \\ \langle D_x^2 \rangle \end{pmatrix}. \quad (3.A12)$$

Note that, for $b = 1$, the quantities (ν_1, ν_2, ν_3) evolve under a closed system of equations. Later, this is used to calculate the asymptotic energy when the system is connected to a thermal bath, see Eq. (3.A36).

The matrix appearing in Eq. (3.A17) has six eigenvalues, but no closed-form solution for arbitrary values of the parameters was obtained. However, in the limit $b \rightarrow 1$, the six eigenvalues can be obtained, to first order in $(1 - b)$:

$$\begin{pmatrix} -2\gamma(1 - b), -\gamma \pm \sqrt{\gamma^2 - 4\omega^2} - \frac{4\gamma\omega^2(1 - b)}{\gamma^2 - 4\omega^2 \mp \gamma\sqrt{\gamma^2 - 4\omega^2}}, \\ -b\gamma, -\frac{\gamma}{2} \pm \sqrt{\frac{\gamma^2}{4} - \omega^2} + \frac{2\gamma\omega^2(1 - b)}{\gamma^2 - 4\omega^2 \pm \sqrt{\gamma^2 - 4\omega^2}} \end{pmatrix}. \quad (3.A13)$$

We also have the approximate solution for these six eigenvalues in the limit $b \rightarrow 0$:

$$\left(-2\gamma + \frac{2\gamma\omega^2 b}{\gamma^2 + \omega^2}, \pm 2i\omega \mp \frac{i\gamma\omega b}{\gamma \pm i\omega}, -\frac{\gamma\omega^2 b}{\gamma^2 + \omega^2}, -\gamma \pm i\omega \mp \frac{i\gamma\omega b}{2(\gamma \mp i\omega)} \right). \quad (3.A14)$$

Note that all eigenvalues have negative real parts for $b \lesssim 1$ and $b \gtrsim 0$; thus, the system converges.

We assume the system will converge for all values in the range $0 < b \leq 1$, similar to Protocol XP.

Even though we don't have a closed-form solution for the eigenvalues of the matrix in the most general case, we can still find the analytical results for the fixed point of the dynamics,

$$\vec{\nu}_\infty = \left(\frac{b\gamma}{16\lambda} - \frac{\gamma\lambda}{4\omega^2} + \frac{\lambda(\gamma^2 + \omega^2)}{4b\gamma\omega^2}, \frac{b\gamma}{16\lambda} + \frac{\lambda(\gamma^2 + \omega^2)}{4b\gamma\omega^2}, \frac{\lambda}{2\omega}, \frac{\gamma\lambda}{2b\omega^2}, -\frac{\lambda}{2b\omega}, \frac{4\gamma\lambda^2 + b\gamma\omega^2}{8b(1-b)\lambda\omega^2} \right)^T. \quad (3.A15)$$

The asymptotic energy and position variance results can be calculated directly from Eq. (3.A15),

$$\langle \hat{H}_x \rangle_\infty = \hbar\omega (\nu_{1,\infty} + \nu_{2,\infty}), \quad (3.A16a)$$

$$\langle \hat{x}^2 \rangle_\infty = 2\nu_{1,\infty} + 2b\nu_{2,\infty} + b^2\nu_{4,\infty}. \quad (3.A16b)$$

Here, $\nu_{i,\infty}$ for $i = 1, \dots, 6$, denotes the fixed point of the dynamics. Note that $\langle \hat{x}^2 \rangle_\infty$ is equal to the variance of position since these dynamics give $\langle \hat{x} \rangle_\infty = 0$ (for $b < 1$).

3D Protocol XP: Position and Momentum Measurements

To solve for the asymptotic expectation value of $\hat{H}_{xp}(\mathbf{D})$, we first use Eq. (3.20) to write a set of evolution equations for $\langle \hat{H}_{xp}(\mathbf{D}) \rangle$ and quantities that couple to it. In matrix form, these

equations are:

$$\partial_t \begin{pmatrix} \nu_1 \\ \nu_2 \\ \nu_3 \\ \nu_4 \end{pmatrix} = \begin{pmatrix} -2\gamma b & -\gamma b(b-1) & 0 & 0 \\ 2\gamma & -\gamma & \omega & -\gamma b(b-1) \\ 0 & -\omega & -\gamma & 0 \\ 0 & 2\gamma & 0 & 2\gamma(b-1) \end{pmatrix} \begin{pmatrix} \nu_1 \\ \nu_2 \\ \nu_3 \\ \nu_4 \end{pmatrix} + \begin{pmatrix} b^2 \frac{\gamma^2}{4\lambda} \\ -b \frac{\gamma^2}{2\lambda} \\ 0 \\ \frac{\gamma^2}{2\lambda} \end{pmatrix}, \quad (3.A17)$$

where

$$\begin{pmatrix} \nu_1 \\ \nu_2 \\ \nu_3 \\ \nu_4 \end{pmatrix} \equiv \begin{pmatrix} \frac{1}{2} [\langle (\hat{p} - D_p)^2 \rangle + \langle (\hat{x} - D_x)^2 \rangle] \\ \langle (\hat{x} - bD_x)D_x + (\hat{p} - bD_p)D_p \rangle \\ \langle (\hat{p} - bD_p)D_x - (\hat{x} - bD_x)D_p \rangle \\ \langle D_x^2 + D_p^2 \rangle \end{pmatrix}. \quad (3.A18)$$

Note that if $b = 1$, the evolution of the average energy, described by ν_1 , follows a first-order ODE. Thus, the average energy decays exponentially to its asymptotic value. The relaxation rate in this case is given by 2γ .

The matrix appearing in Eq. (3.A17) has four eigenvalues:

$$-\gamma \pm \frac{\Delta_{\pm}}{\sqrt{2}}, \quad (3.A19)$$

where $\Delta_{\pm} = \sqrt{-\omega^2 + \gamma^2 \pm \Omega}$ and $\Omega = \sqrt{\omega^4 + 2(1 - 8b + 8b^2)\omega^2\gamma^2 + \gamma^4}$. These eigen-

values, which determine relaxation rates, must be negative for the solution of Eq. (3.A17) to converge. This condition sets the bounds $0 < b \leq 1$, as expected. The asymptotic solution for the system can be found from the fixed point of the dynamics,

$$\vec{\nu}_\infty = \left(\frac{b\gamma}{8\lambda} - \frac{\gamma\lambda}{2\omega^2} + \frac{\lambda(\gamma^2 + \omega^2)}{2b\gamma\omega^2}, \frac{\gamma\lambda}{b\omega^2}, -\frac{\lambda}{b\omega}, \frac{4\gamma\lambda^2 + b\gamma\omega^2}{4b(1-b)\lambda\omega^2} \right)^T. \quad (3.A20)$$

The asymptotic energy and position variance results can be calculated directly from Eq. (3.A20),

$$\langle \hat{H}_{xp} \rangle_\infty = \hbar\omega\nu_{1,\infty}, \quad (3.A21a)$$

$$\langle \hat{x}^2 \rangle_\infty = \nu_{1,\infty} + b\nu_{2,\infty} + \frac{b^2}{2}\nu_{4,\infty}. \quad (3.A21b)$$

Here, $\nu_{i,\infty}$ for $i = 1, \dots, 4$, denotes the fixed point of the dynamics.

Note that, to derive the equation for $\langle \hat{x}^2 \rangle_\infty$, we explicitly assumed that $\langle \hat{x}^2 \rangle_\infty = \langle \hat{p}^2 \rangle_\infty$ due to the $x \leftrightarrow p$ symmetry in the system. Also, recall that this protocol has a fixed point $\langle \hat{x} \rangle_\infty = 0$ (for $b < 1$), thus we can write $\sigma_{x,\infty}^2 \equiv \langle \hat{x}^2 \rangle_\infty - \langle \hat{x} \rangle_\infty^2 = \langle \hat{x}^2 \rangle_\infty$.

3E Protocol C: Cross Feedback

To derive the results presented in Sec. (3.3.3) we first define a six-dimensional vector $\vec{\nu}_c = (\frac{\omega}{2}\langle \hat{x}^2 \rangle, \frac{\omega}{2}\langle \hat{p}^2 \rangle, \frac{\omega}{2}\langle (\hat{x}\hat{p} + \hat{p}\hat{x}) \rangle, \langle D_x \hat{x} \rangle, \langle D_x \hat{p} \rangle, \langle D_x^2 \rangle)$ to describe the dynamics of average quantities of interest, as follows:

$$\partial_t \vec{\nu}_c(\omega, \gamma, \lambda, \Gamma, t) = \mathbf{M}_c(\omega, \gamma, \mu, \Gamma) \vec{\nu}_c(\omega, \gamma, \lambda, \Gamma, t) + \vec{\nu}_{s,c}(\omega, \gamma, \lambda, \Gamma), \quad (3.A22)$$

where

$$\vec{v}_{s,c}(\omega, \gamma, \lambda, \Gamma) = \left(\frac{\Gamma\omega(\bar{n} + 1/2)}{2}, \frac{\omega\lambda}{2} + \frac{\Gamma\omega(\bar{n} + 1/2)}{2}, 0, 0, 0, \frac{\gamma^2}{4\lambda} \right)^T, \quad (3.A23)$$

and

$$\mathbf{M}_c(\omega, \gamma, \mu, \Gamma) = \begin{pmatrix} -\Gamma & 0 & \omega & -\mu\omega^2 & 0 & 0 \\ 0 & -\Gamma & -\omega & 0 & \frac{\Gamma\omega\mu}{2} & 0 \\ -2\omega & 2\omega & -\Gamma & \frac{\Gamma\omega\mu}{2} & -\mu\omega^2 & 0 \\ \frac{2\gamma}{\omega} & 0 & 0 & -\gamma - \frac{\Gamma}{2} & \omega & -\mu\omega \\ 0 & 0 & \frac{\gamma}{\omega} & -\omega & -\gamma - \frac{\Gamma}{2} & \frac{\Gamma\mu}{2} \\ 0 & 0 & 0 & 2\gamma & 0 & -2\gamma \end{pmatrix}. \quad (3.A24)$$

It is generally complicated to solve Eq. (3.A22) for an arbitrary set of parameters. However, one can obtain the asymptotic average energy in the case $\Gamma = 0$ by considering $\partial_t \vec{v}_c(\omega, \gamma, \lambda, t \rightarrow \infty) = 0$. We then have

$$\vec{v}_c(\omega, \gamma, \lambda, 0, t \rightarrow \infty) = \left(\frac{\mu\omega^2}{16\lambda} + \frac{\lambda(\gamma^2 + \omega^2)}{4\gamma^2\mu}, \frac{\mu\omega^2}{16\lambda} + \frac{\lambda(\gamma^2(1 + \mu^2) - \gamma\mu\omega + \omega^2)}{4\gamma^2\mu}, \frac{\lambda}{2}, \frac{\lambda}{2\mu\omega}, \frac{\lambda}{2} \left(-\frac{1}{\gamma\mu} + \frac{1}{\omega} \right), \frac{\gamma}{8\lambda} + \frac{\lambda}{2\mu\omega} \right)^T. \quad (3.A25)$$

Using Eq. (3.A25), the asymptotic value for the average internal energy can be calculated using the Hamiltonian in Eq. (3.6):

$$\langle \hat{H}_c \rangle_\infty = \frac{\hbar\omega}{2} \left[\frac{\mu\omega}{4\lambda} + \frac{\lambda}{\mu\omega} + \frac{\lambda}{2\gamma} + \frac{\lambda\omega}{\gamma^2\mu} + \frac{\gamma\mu^2}{8\lambda} \right] \quad (3.A26)$$

To get the timescale of the process, we need to solve for the eigenvalues of Eq. (3.A24). That cannot be done analytically for arbitrary values of $(\omega, \gamma, \lambda, \mu)$, but one can find the eigenvalues when $\mu \rightarrow 0$, which is the condition for ground state cooling. The six eigenvalues, up to $\mathcal{O}(\mu)$, are

$$\left(-\frac{\gamma^2\omega\mu}{\gamma^2 + \omega^2}, -\gamma - i\omega + \frac{\gamma\omega\mu}{2(\gamma + i\omega)}, -\gamma + i\omega + \frac{\gamma\omega\mu}{2(\gamma - i\omega)}, \right. \\ \left. -2\gamma + \frac{2\gamma^2\omega\mu}{\gamma^2 + \omega^2}, -2i\omega - \frac{\gamma\omega\mu}{\gamma - i\omega}, 2i\omega - \frac{\gamma\omega\mu}{\gamma + i\omega} \right). \quad (3.A27)$$

If we assume $\gamma \gg \omega \gg \lambda$, then the slowest timescale is $\omega\mu$, which in the optimal condition is $\omega\mu^* = 2\lambda$.

When the bath coupling is non-zero $\Gamma \neq 0$, one can solve the same set of equations to find the asymptotic average energy

$$\langle \hat{H}_c \rangle_\infty = \frac{\hbar \left(\begin{array}{l} 2\mu^3\omega^2\gamma^3 + \mu^2\omega\gamma^2 [4\omega^2 + \Gamma(2\gamma + \Gamma)] + \\ 8\mu\omega^2\gamma\lambda^2 + 4\omega\lambda^2 [4\omega^2 + (2\gamma + \Gamma)^2] + \\ 8\Gamma [4\omega^2 + 4\mu\omega\gamma + \gamma^2(4 + \mu^2) + 4\gamma\Gamma + \Gamma^2] \lambda U_{\text{th}}/\hbar \end{array} \right)}{32\mu\omega\gamma\lambda(\gamma + \Gamma) + 8\lambda\Gamma [4\omega^2 + (2\gamma + \Gamma)^2]}. \quad (3.A28)$$

Let's assume that $\gamma \gg \omega \gg \lambda\gamma/\omega, \mu\gamma, \Gamma\gamma/\omega$. In this case, Eq. (3.A28) becomes

$$\langle \hat{H}_c \rangle_\infty = \frac{\mu\omega \left\{ \frac{\hbar\omega}{2} \left[\frac{\lambda}{\mu\omega} + \frac{\mu\omega}{4\lambda} \right] \right\} + \Gamma U_{\text{th}}}{\mu\omega + \Gamma}. \quad (3.A29)$$

3E.1 Position spreading

To investigate the motion and trapping caused by the cross-feedback protocol, we need to calculate the asymptotic position variance, $\sigma_{x,\infty}^2 \equiv \langle \hat{x}^2 \rangle_\infty - \langle \hat{x} \rangle_\infty^2$. From Eq. (3.A25) we have

$$\langle \hat{x}^2 \rangle_\infty = \frac{\mu\omega}{8\lambda} + \frac{\lambda(\gamma^2 + \omega^2)}{2\gamma^2\mu\omega}. \quad (3.A30)$$

We can determine $\langle \hat{x} \rangle_\infty$ by solving the system of equations

$$\partial_t \langle \hat{x} \rangle = \omega (\langle \hat{p} \rangle - \mu \langle D_x \rangle), \quad (3.A31)$$

$$\partial_t \langle \hat{p} \rangle = -\omega \langle \hat{x} \rangle, \quad (3.A32)$$

$$\partial_t \langle D_x \rangle = \gamma (\langle \hat{x} \rangle - \langle D_x \rangle). \quad (3.A33)$$

The asymptotic solution of this system of equations is:

$$\langle \hat{x} \rangle_\infty = 0, \quad \langle \hat{p} \rangle_\infty = 0, \quad \langle D_x \rangle_\infty = 0. \quad (3.A34)$$

Combining both solutions, we conclude the asymptotic variance of the particle is

$$\sigma_{x,\infty}^2 = \frac{\mu\omega}{8\lambda} + \frac{\lambda(\gamma^2 + \omega^2)}{2\gamma^2\mu\omega}. \quad (3.A35)$$

3F Thermal coupling

Here, we present the results for the asymptotic average energy for Protocols X and XP in the simplest case of $b = 1$. Using this simplification, the equations for the asymptotic energy are more symmetrical and easier to solve. We will re-derive the equations as they differ from the previous sections.

When focusing on cooling, the average energy for Protocol X evolves under the following system of linearly coupled differential equations:

$$\partial_t \langle \hat{V} \rangle = \frac{\hbar\omega^2}{2} \langle \hat{G} \rangle - 2\gamma \langle \hat{V} \rangle + \frac{\hbar\omega\gamma^2}{8\lambda} - \Gamma \langle \hat{V} \rangle + \Gamma \frac{\hbar\omega}{2} (\bar{n} + 1/2), \quad (3.A36a)$$

$$\partial_t \langle \hat{K} \rangle = -\frac{\hbar\omega^2}{2} \langle \hat{G} \rangle + \frac{\hbar\omega\lambda}{2} - \Gamma \langle \hat{K} \rangle + \Gamma \frac{\hbar\omega}{2} (\bar{n} + 1/2), \quad (3.A36b)$$

$$\partial_t \langle \hat{G} \rangle = \frac{4}{\hbar} \langle \hat{K} \rangle - \frac{4}{\hbar} \langle \hat{V} \rangle - \gamma \langle \hat{G} \rangle - \Gamma \langle \hat{G} \rangle, \quad (3.A36c)$$

$$\partial_t \langle \hat{H}_x \rangle = \frac{\hbar\omega\lambda}{2} + \frac{\hbar\omega\gamma^2}{8\lambda} - 2\gamma \langle \hat{V} \rangle - \Gamma \langle \hat{H}_x \rangle + \Gamma \hbar\omega (\bar{n} + 1/2), \quad (3.A36d)$$

where $\hat{V} = \hbar\omega(\hat{x} - D_x)^2/2$, $\hat{K} = \hbar\omega\hat{p}^2/2$ and $\hat{G} = (\hat{x} - D_x)\hat{p} + \hat{p}(\hat{x} - D_x)$. This system can be obtained from Eqs. (3.10), (3.11) and (3.36).

When $\Gamma \neq 0$, the asymptotic energy relaxes to

$$\langle \hat{H}_x \rangle_\Gamma = \frac{\langle \hat{H}_x \rangle_\infty [4\omega^2\gamma + \gamma\Gamma(\gamma + \Gamma)] + U_{\text{th}} [4\omega^2\Gamma + \Gamma(\gamma + \Gamma)^2] + \hbar\omega\lambda\gamma\Gamma \left[1 - \frac{\gamma(\gamma + \Gamma)}{4\omega^2} \right]}{4\omega^2(\gamma + \Gamma) + (\gamma + \Gamma)(2\gamma + \Gamma)\Gamma}, \quad (3.A37)$$

with U_{th} given by (3.35), and $\langle \hat{H}_x \rangle_\infty$ given by Eq. (3.12) with $b = 1$.

We can proceed similarly for Protocol XP. One can use Eqs. (3.20) and (3.37) to write down a system of linearly coupled ODEs for relevant expectation values. For simplicity, we set $b = 1$,

$\lambda_x = \lambda_p = \lambda$ and $\gamma_x = \gamma_p = \gamma$, obtaining

$$\partial_t \langle \hat{V} \rangle = \frac{\hbar\omega^2}{2} \langle \hat{G} \rangle - 2\gamma \langle \hat{V} \rangle + \frac{\hbar\omega\lambda}{2} + \frac{\hbar\omega\gamma^2}{8\lambda} + \Gamma \left(U_{\text{th}}/2 - \langle \hat{V} \rangle \right), \quad (3.A38a)$$

$$\partial_t \langle \hat{K} \rangle = -\frac{\hbar\omega^2}{2} \langle \hat{G} \rangle - 2\gamma \langle \hat{K} \rangle + \frac{\hbar\omega\lambda}{2} + \frac{\hbar\omega\gamma^2}{8\lambda} + \Gamma \left(U_{\text{th}}/2 - \langle \hat{K} \rangle \right), \quad (3.A38b)$$

$$\partial_t \langle \hat{G} \rangle = \frac{4}{\hbar} \langle \hat{K} \rangle - \frac{4}{\hbar} \langle \hat{V} \rangle - 2\gamma \langle \hat{G} \rangle - \Gamma \langle \hat{G} \rangle, \quad (3.A38c)$$

$$\partial_t \langle \hat{H}_{xp} \rangle = (2\gamma + \Gamma) \left[\frac{2\gamma \langle \hat{H}_{xp} \rangle_{\infty} + \Gamma U_{\text{th}}}{2\gamma + \Gamma} - \langle \hat{H}_{xp} \rangle \right]. \quad (3.A38d)$$

Here, $\langle \hat{H}_{xp} \rangle_{xp}$ is given by Eq. (3.21) with $b = 1$, U_{th} is the thermal energy the system would relax to in the absence of measurement and feedback, see Eq. (3.35); $\langle \hat{K} \rangle = (\hbar\omega/2) \langle (\hat{p} - D_p)^2 \rangle$; $\langle \hat{V} \rangle = (\hbar\omega/2) \langle (\hat{x} - D_x)^2 \rangle$; and $\langle \hat{G} \rangle = \langle (\hat{x} - D_x)(\hat{p} - D_p) + (\hat{p} - D_p)(\hat{x} - D_x) \rangle$. From Eq. (3.A38), we obtain the asymptotic value of the average energy:

$$\langle \hat{H}_{xp} \rangle_{\Gamma} = \frac{2\gamma \langle \hat{H}_{xp} \rangle_{\infty} + \Gamma U_{\text{th}}}{2\gamma + \Gamma}. \quad (3.A39)$$

3G Trajectory simulation

Suppose one starts from the Belavkin equation in Eq. (3.43) and writes the time evolution of the expectation value of powers of position or momentum ($\langle \hat{x} \rangle$, $\langle \hat{x}^2 \rangle$, $\langle \hat{p} \rangle$, $\langle \hat{p}^2 \rangle$, etc). These equations form a non-closing system because the evolution of the n -th power depends on the $(n + 1)$ -th power. However, using the Gaussian wave packet assumption [69, 81, 160] one can

derive the following relations:

$$\langle \hat{x}^3 \rangle = \langle \hat{x} \rangle^3 + 3\langle \hat{x} \rangle V_x, \quad (3.A40a)$$

$$\langle \hat{p}^3 \rangle = \langle \hat{p} \rangle^3 + 3\langle \hat{p} \rangle V_p, \quad (3.A40b)$$

$$\langle \hat{x} \hat{p}^2 + \hat{p}^2 \hat{x} \rangle = 2\langle \hat{x} \rangle \langle \hat{p}^2 \rangle + 2\langle p \rangle C, \quad (3.A40c)$$

$$\langle \hat{x}^2 \hat{p} + \hat{p} \hat{x}^2 \rangle = 2\langle \hat{x}^2 \rangle \langle \hat{p} \rangle + 2\langle \hat{x} \rangle C. \quad (3.A40d)$$

Here $V_x = \langle \hat{x}^2 \rangle - \langle \hat{x} \rangle^2$, $V_p = \langle \hat{p}^2 \rangle - \langle \hat{p} \rangle^2$ and $C = \langle \hat{x} \hat{p} + \hat{p} \hat{x} \rangle - 2\langle \hat{x} \rangle \langle \hat{p} \rangle$. Using this assumption, one can close the system of equations and arrive at the following coupled ordinary stochastic differential system of equations [131]:

$$d\langle \hat{x} \rangle = \omega (\langle \hat{p} \rangle - b_x D_x - b_p D_p) dt + 2\sqrt{\lambda_x} V_x dW_x + \sqrt{\lambda_p} C dW_p, \quad (3.A41a)$$

$$d\langle \hat{p} \rangle = -\omega (\langle \hat{x} \rangle - c_x D_x - c_p D_p) dt + \sqrt{\lambda_x} C dW_x + 2\sqrt{\lambda_p} V_p dW_p, \quad (3.A41b)$$

$$dV_x = (\omega C + \lambda_p - 4\lambda_x V_x^2 - \lambda_p C^2) dt, \quad (3.A41c)$$

$$dV_p = (-\omega C + \lambda_x - 4\lambda_p V_p^2 - \lambda_x C^2) dt, \quad (3.A41d)$$

$$dC = [2\omega V_p - 2\omega V_x - 4(\lambda_x V_x + \lambda_p V_p) C] dt, \quad (3.A41e)$$

$$dD_x = \gamma_x (\langle \hat{x} \rangle - D_x) dt + \frac{\gamma_x}{\sqrt{4\lambda_x}} dW_x, \quad (3.A41f)$$

$$dD_p = \gamma_p (\langle \hat{p} \rangle - D_p) dt + \frac{\gamma_p}{\sqrt{4\lambda_x}} dW_p. \quad (3.A41g)$$

The equation for dD_x and dD_p follows from the exponential filtering described in Eq. (3.A9).

This system can be solved numerically using standard algorithms for solving stochastic differential equations. From this solution we can calculate the energy at all times along the trajectory

using Eq. (3.45):

$$\langle \hat{H} \rangle = \frac{\hbar\omega}{2} [V_x + (\langle \hat{x} \rangle - c_x D_x - c_p D_p)^2 + V_p + (\langle \hat{p} \rangle - b_x D_x - b_p D_p)^2]. \quad (3.A42)$$

Note that Eqs. (3.A41c, 3.A41d, 3.A41e) are deterministic, and if $\lambda_x = \lambda_p = \lambda$ they reach symmetric asymptotic values

$$(V_x)_\infty = \frac{1}{2}, \quad (V_p)_\infty = \frac{1}{2}, \quad C_\infty = 0. \quad (3.A43)$$

Chapter 4: Quantum Fokker-Planck Master Equation with general filtering

This chapter is based on work done in collaboration with Björn Annby-Andersson and Christopher Jarzynski, manuscript currently in preparation [5]. My contribution to this work was to derive the master equations and apply them to the quantum harmonic toy model.

The goal of this chapter is to extend the Quantum Fokker-Planck Master Equation (QF-PME) [1–3] to the case where the experiment has a generic filtering spectrum. The results include master equations for a chain of low-pass filters, a band-pass filter, and a generic filter described by an ODE. Finally, the master equations are applied to cooling a quantum harmonic oscillator, similar to the results presented in Chapter 3.

4.1 Introduction

Recent years have seen an increase in interest in quantum feedback systems, quantum measurements, and, more broadly, quantum control [127, 161–163]. Experiments have reached the point where atoms can be trapped and controlled, single photons can be measured, the coherence time for quantum systems has been increasing, and many other advances have been made [19, 164–168]. This advancement has important applications in quantum sensing and quantum computing [37, 96, 169–173].

On the theoretical side, much research has been done to understand feedback systems and

their flux of information, and to design protocols to implement nano-machines [1, 2, 56, 65, 68, 80, 174–176]. The area of quantum thermodynamics has also drawn much attention to extend the questions of classical thermodynamics in the quantum regime [42, 177–180]. The goal is to be able to control and drive quantum systems to produce valuable outcomes [181–185].

In this chapter, I investigate continuous feedback in quantum systems and generalize results of previous works [1, 3] (see Chapter 3) by studying a larger class of filtering protocols. The goal is to develop theoretical models representing realistic experimental conditions, including finite bandwidth effects, lag, and information processing for feedback [186–188].

The results show a promising avenue for the theoretical modeling of continuous feedback. I derived a general formulation of the QFPME [1] with arbitrary signal processing and applied it to the study of cooling a quantum harmonic oscillator [3]. The results indicate that one can describe feedback systems using Markovian dynamics, even when the filters contain complicated frequency dependence. This is due to an increase in the system’s dimensionality, similar to a Markovian embedding [189–192].

The chapter is structured as follows: Sec. 4.2 extends the framework to the case of multiple low-pass filters. Section 4.3 presents the QFPME using a band-pass filter, and Sec. 4.4 generalizes for an arbitrary continuous filter. We apply these different filters to a quantum harmonic oscillator in Sec. 4.5. A discussion and conclusions are presented in Sec. 4.6.

4.2 QFPME with multiple low-pass filters

This section will sketch the steps to derive QFPME with multiple low-pass filters — for a discussion on the original QFPME, see Secs. 2.4 and 3.2.3. The strategy for this derivation

follows the stochastic calculus section of Supplemental Material on Ref.[1] and the Appendix of Ref. [3] (see Chapter 3 Appendix 3B).

We start with the Belavkin equation for a continuous measurement [66, 67, 86–88]

$$d\hat{\rho}_c = \frac{-i}{\hbar}[\hat{H}, \hat{\rho}_c]dt + \lambda \mathcal{D}[\hat{A}]\hat{\rho}_c dt + \sqrt{\lambda} dW \{\hat{A} - \langle \hat{A} \rangle, \hat{\rho}_c\}. \quad (4.1)$$

Here, $\hat{\rho}_c$ denotes the density matrix conditioned to observing the measured signal $z(t)$. The parameter λ characterizes the measurement strength, and controls how much backaction is caused in the system; the superoperator $\mathcal{D}[\hat{c}]\hat{\rho} = \hat{c}\hat{\rho}\hat{c}^\dagger - \frac{1}{2}\hat{c}\hat{c}^\dagger\hat{\rho} - \frac{1}{2}\hat{\rho}\hat{c}\hat{c}^\dagger$ is called dissipator. The last term of the right-hand side of Eq. (4.1) contains the stochastic evolution; dW is the stochastic Weiner increment that satisfies $dW^2 = dt$; $\langle \hat{A} \rangle = \text{tr}[\hat{A}\hat{\rho}_c]$ is the expected value of the measured operator, where $\{\cdot, \cdot\}$ is the anticommutator.

The measurement outcome associated with the evolution of Eq. (4.1) is given by the signal $z(t)$ in Eq. (2.20). Here, we will imagine that the experimental apparatus comprises n filters, where the first one is denoted by D_1 and defined by Eq. (2.24) and the next ones are labeled D_k , where $k = 2, \dots, n$. A low-pass filter models each additional filter

$$D'_k(t) = \gamma_k \int_{-\infty}^t ds e^{-\gamma_k(t-s)} D'_{k-1}(s), \quad k \geq 2 \quad (4.2)$$

$$dD'_k = \gamma_k (D'_{k-1} - D'_k) dt. \quad (4.3)$$

The parameters $\{\gamma_k\}$, represent the experimental bandwidth of the filters. This framework aims to model experiments composed of various pieces of equipment, where the output of a given layer is the input of the next one, see Fig 4.1. After all layers of filtering are taken into account, we can

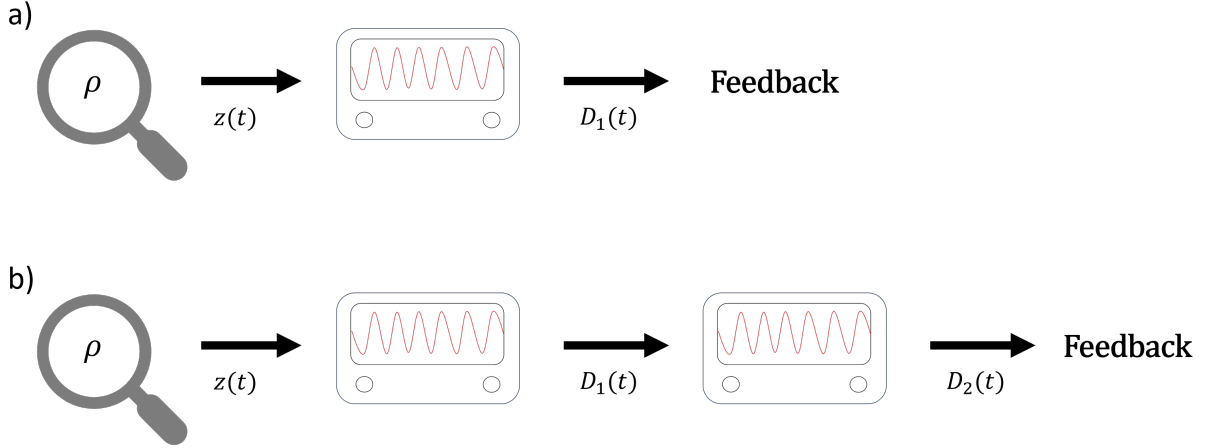


Figure 4.1: a) Single-filter feedback scheme: the outcome of the continuous measurement is processed by a single component. The Hamiltonian directly uses the signal $D_1(t)$ to perform feedback $\hat{H} = \hat{H}(D_1(t))$; b) Multiple-filter feedback scheme: multiple components add finite bandwidths to the system, and the final feedback can use all signals to change the Hamiltonian $\hat{H} = \hat{H}(\mathbf{D}'(t))$.

apply time-dependent feedback by changing the Hamiltonian in terms of these delayed signals

$\hat{H} = \hat{H}(\mathbf{D}'(t))$, where $\mathbf{D}' = (D'_1, \dots, D'_n)$ represents the set of all filters.

The quantity we are interested in is

$$\hat{\rho}(\mathbf{D}) = E_W \left[\hat{\rho}_c \delta \prod_{k=1}^n \delta(D'_k - D_k) \right], \quad (4.4)$$

which is an average over possible trajectories that yields the same measurement outcomes at a given time. The object described by Eq. (4.4) is a joint distribution that contains information about the quantum density matrix and the probability of observing a particular measurement outcome \mathbf{D} at time t .

To derive the master equation for the time evolution of Eq. (4.4), we need to use the stochastic rules of calculus in the Ito formalism [Eqs. (1.43,1.44)]. We can combine Eqs. (1.43,1.44,

2.25, 4.1–4.4) to derive the QFPME with multiple low-pass filters:

$$\begin{aligned} \partial_t \hat{\rho}(\mathbf{D}) = & \frac{-i}{\hbar} \left[\hat{H}(\mathbf{D}), \hat{\rho}(\mathbf{D}) \right] + \lambda \mathcal{D}[\hat{A}] \hat{\rho}(\mathbf{D}) - \frac{\gamma_1}{2} \partial_{D_1} \{ \hat{A} - D_1, \hat{\rho}(\mathbf{D}) \} \\ & - \sum_{k=2}^n \gamma_k \partial_{D_k} [(D_{k-1} - D_k) \hat{\rho}(\mathbf{D})] + \frac{\gamma^2}{8\lambda} \partial_{D_1}^2 \hat{\rho}(\mathbf{D}). \end{aligned} \quad (4.5)$$

Equation (4.5) has a Fokker-Planck-like form, similar to Eq. (2.30). The generalized drift represents the relaxation of the k 'th filter with its characteristic bandwidth γ_k . The only diffusive term in Eq. (4.5) is the signal D_1 . This happens because all the other signals evolve deterministically toward one another. In contrast, the first signal evolves under an OU process towards the measured operator expectation value. In the next section, we will explore the case where the filtering is implemented using a band-pass filter instead of multiple low-pass filters.

4.3 QFPME with Band-pass filtering

We can construct the QFPME with a band-pass filter by changing the form of the filtering operation in Eq. (2.24). There are multiple ways to implement a band-pass filter, i.e. a filter that only allows signals in an intermediate range of frequencies in the spectral domain. Here, we will focus on a particular realization of band-pass that takes the form of a Lorentzian function in the Fourier domain. This filter can be written as a frequency shift of the exponential low-pass filter in Eq. (2.24),

$$E'_1(t) = \gamma \int_{-\infty}^t ds e^{-\gamma(t-s)} \cos(\Omega(t-s)) z(s). \quad (4.6)$$

However, the signal in Eq. (4.6) obeys a second-order equation, so we need to define an auxiliary signal $E_2(t)'$:

$$E_2'(t) = \gamma \int_{-\infty}^t ds e^{-\gamma(t-s)} \sin(\Omega(t-s)) z(s). \quad (4.7)$$

The following system of equations couples the two signals that form the band-pass filter:

$$dE_1' = \gamma(z - E_1') dt - \Omega E_2' dt, \quad (4.8)$$

$$dE_2' = (\Omega E_1' - \gamma E_2') dt. \quad (4.9)$$

Following the same steps we took to derive Eq. (4.5) in Sec. 4.2, we use Eqs. (4.8,4.9) to derive a QFPME with band-pass filter:

$$\begin{aligned} \partial_t \hat{\rho}(\mathbf{E}) &= \frac{-i}{\hbar} [\hat{H}(\mathbf{E}), \hat{\rho}(\mathbf{E})] + \lambda \mathcal{D}[\hat{A}] \hat{\rho}(\mathbf{E}) \\ &- \partial_{E_1} \left[\frac{1}{2} \left\{ \gamma \hat{A} - \gamma E_1 - \Omega E_2, \hat{\rho}(\mathbf{E}) \right\} \right] - \partial_{E_2} [(\Omega E_1 - \gamma E_2) \hat{\rho}(\mathbf{E})] + \frac{\gamma^2}{8\lambda} \partial_{E_1}^2 \hat{\rho}(\mathbf{E}), \end{aligned} \quad (4.10)$$

where $\mathbf{E} = (E_1, E_2)$. The evolution of the signals $(E_1(t), E_2(t))$ is captured by the drift term in Eq. (4.10) and the diffusion is only present in E_1 because it is the one that has a stochastic term from the measurement outcome $z(t)$.

4.4 QFPME with general filtering

4.4.1 General analytical filtering

Motivated by the construction in Sec. 4.3, we can write how the QFPME changes when we use a general filter of the form

$$F'_1(t) = \int_{-\infty}^t ds f(t-s)z(s). \quad (4.11)$$

The function $f(t)$ is the filter kernel. We consider the case where $f(t)$ obeys a finite ODE

$$f^{(n)}(t) + a_{n-1}f^{(n-1)}(t) + \cdots + a_0f(t) = 0. \quad (4.12)$$

The low-pass filter considered in Sec. 2.4 obeys a first-order ODE, and the band-pass filter considered in Sec. 4.3 obeys a second-order ODE.

To solve for the QFPME associated with the filter in Eq. (4.11), we need to define $n - 1$ auxiliary signals

$$F'_{k+1} = \int_{-\infty}^t ds f^{(k)}(t-s)z(s), \quad k \leq n. \quad (4.13)$$

These signals evolve under the following coupled ODE:

$$dF'_1 = f(0)z(t)dt + F'_2dt \quad (4.14a)$$

$$dF'_{k+1} = f^{(k)}(0)z(t)dt + F'_{k+2}dt \quad (4.14b)$$

$$dF'_n = f^{(n-1)}(0)z(t)dt - \sum_{j=1}^n a_{j-1}F'_jdt. \quad (4.14c)$$

Combining Eqs. (4.1,4.14) we have the following QFPME:

$$\begin{aligned}
\partial_t \hat{\rho}(\mathbf{F}) &= \frac{-i}{\hbar} \left[\hat{H}(\mathbf{F}), \hat{\rho}(\mathbf{F}) \right] + \lambda \mathcal{D}[\hat{A}] \hat{\rho}(\mathbf{F}) \\
&- \sum_{j=1}^{n-1} \partial_{F_j} \left[\frac{1}{2} \left\{ f^{(j-1)}(0) \hat{A} + F_{j+1}, \hat{\rho}(\mathbf{F}) \right\} \right] - \partial_{F_n} \left[\frac{1}{2} \left\{ f^{n-1}(0) \hat{A} - \sum_{k=1}^n a_{k-1} F_k, \hat{\rho}(\mathbf{F}) \right\} \right] \\
&+ \sum_{j=1}^n \sum_{k=1}^n \frac{f^{(j-1)}(0) f^{(k-1)}(0)}{8\lambda} \partial_{F_j} \partial_{F_k} \hat{\rho}(\mathbf{F}),
\end{aligned} \tag{4.15}$$

where $\mathbf{F} = (F_1, F_2, \dots, F_n)$. The drift terms describe the deterministic evolution of each signal, where the final signal is given by the ODE that defines the filter. The second derivative can contain cross terms depending on how many signals have stochastic evolution in Eq. (4.14).

The general filtering in Eq. (4.11) can be mapped to the classical PID controller using:

$$\begin{cases} \text{P} : f(t-s) \propto \delta(t-s) \\ \text{I} : f(t-s) \propto 1 \\ \text{D} : f(t-s) \propto \delta'(t-s) \end{cases} \tag{4.16}$$

The low-pass filter used in the original derivation of the QFPME can be translated into the integral gain in the limit where

$$\lim_{\gamma \rightarrow 0} (D/\gamma) \Rightarrow \text{Integral gain.} \tag{4.17}$$

Inspired by the system in Eq. (4.14), we take the final step to generalize the QFPME to an arbitrary system of coupled signals that can describe any general filter or sequence of filters for a single measurement.

4.4.2 General signals

Consider a system of coupled signals that evolve under the following ODE:

$$dG'_k = b_k z(t) dt + \sum_{j=1}^n M_{kj} G'_j dt, \quad k = 1, \dots, n \quad (4.18)$$

The matrix \mathbf{M} and the vector $\mathbf{b} = (b_1, \dots, b_n)$ specify the model and can describe all previous cases (see Appendix 4B). The QFPME corresponding to Eq. (4.18) is

$$\begin{aligned} \partial_t \hat{\rho}(\mathbf{G}) &= \frac{-i}{\hbar} \left[\hat{H}(\mathbf{G}), \hat{\rho}(\mathbf{G}) \right] + \lambda \mathcal{D}[\hat{A}] \hat{\rho}(\mathbf{G}) \\ &- \sum_{k=1}^n \partial_{G_k} \left[\frac{1}{2} \left\{ b_k \hat{A} + \sum_j M_{kj} G_j, \hat{\rho}(\mathbf{G}) \right\} \right] + \sum_{j=1}^n \sum_{k=1}^n \frac{b_j b_k}{8\lambda} \partial_{G_j} \partial_{G_k} \hat{\rho}(\mathbf{G}). \end{aligned} \quad (4.19)$$

See Appendix 4A for a derivation of Eq. (4.19). In the remainder of the chapter, I apply the QFPME with multiple low-pass filters and the QFPME with a band-pass filter to an analytically solvable model.

4.5 Harmonic oscillator

This section focuses on applying the QFPME with multiple filters to the toy model used in Chapter 3. We discuss some of the results derived in Chapter 3 for completeness. See Appendix 4C for details on deriving the results presented in this section.

4.5.1 One layer of filtering

Consider a quantum harmonic oscillator (QHO) of mass m and characteristic frequency ω undergoing continuous measurement and feedback. Introducing dimensionless operators $\hat{p} \rightarrow \hat{p}\sqrt{\hbar m\omega}$ and $\hat{x} \rightarrow \hat{x}\sqrt{\hbar/m\omega}$, the Hamiltonian in the absence of feedback becomes

$$\hat{H}_0 = \frac{\hbar\omega}{2} (\hat{p}^2 + \hat{x}^2). \quad (4.20)$$

$$\hat{H}_1(\mathbf{D}_1) = \frac{\hbar\omega}{2} [(\hat{p} - D_{p,1})^2 + (\hat{x} - D_{x,1})^2], \quad (4.21)$$

where $\mathbf{D}_1 = (D_{x,1}, D_{p,1})$. This protocol can achieve cooling because the signal $D_{i,1}$ with $i = x, p$ represents a guess on the particle's position and momentum. The Hamiltonian is then moved to this position to decrease the particle's potential.

As shown in Eq. (3.21), the average energy evolves by the following equation

$$\partial_t \langle \hat{H}_1 \rangle + 2\gamma \langle \hat{H}_1 \rangle = 2\gamma \langle \hat{H}_1 \rangle_\infty, \quad (4.22)$$

where

$$\langle \hat{H}_1 \rangle_\infty \equiv \lim_{t \rightarrow \infty} \langle \hat{H}_1 \rangle = \frac{\hbar\omega}{2} \left(\frac{\lambda}{\gamma} + \frac{\gamma}{4\lambda} \right). \quad (4.23)$$

This simple protocol can cool down the particle to ground state if we choose the parameters $\gamma = 2\lambda$. In this case, we have

$$\langle \hat{H}_1 \rangle_\infty = \frac{\hbar\omega}{2}. \quad (4.24)$$

4.5.2 Two layers of filtering

Here, we will focus on the feedback Hamiltonian given by

$$\hat{H}_2(\mathbf{D}_2) = \frac{\hbar\omega}{2} [(\hat{p} - D_{p,2})^2 + (\hat{x} - D_{x,2})^2]. \quad (4.25)$$

This means the Hamiltonian is changed instantaneously based on a double filtered signal $D_{x/p,2}$.

The filtering frequencies are γ and Ω , see Eqs. (2.24) and (4.6). For the sake of notation, let's denote $U_2 \equiv \langle \hat{H}_2(\mathbf{D}_2) \rangle$.

Using Eqs. (4.5) and (4.25), we can write a single ordinary differential equation for the average energy of the double-filtered protocol:

$$\begin{aligned} \partial_t^4 U_2 + 4(\Omega + \gamma)\partial_t^3 U_2 + [4\Omega\gamma + 5(\Omega + \gamma)^2 + \omega^2]\partial_t^2 U_2 \\ + 2(\Omega + \gamma)[4\Omega\gamma + (\Omega + \gamma)^2 + \omega^2]\partial_t U_2 + 4\Omega\gamma(\Omega + \gamma)^2[U_2 - U_{2,\infty}] = 0, \end{aligned} \quad (4.26)$$

where

$$U_{2,\infty} = \frac{\hbar\omega}{2} \left[\frac{\lambda}{\tilde{\gamma}} + \frac{\tilde{\gamma}}{4\lambda} + \frac{\lambda}{(\Omega + \gamma)} + \frac{\lambda\omega^2}{\tilde{\gamma}(\Omega + \gamma)^2} \right], \quad (4.27)$$

and

$$\frac{1}{\tilde{\gamma}} = \frac{1}{\gamma} + \frac{1}{\Omega} \quad (4.28)$$

is the effective frequency of the filter. The asymptotic solution for the average energy that evolves under Eq. (4.26) is given by

$$\langle \hat{H}_2 \rangle_\infty = \lim_{t \rightarrow \infty} U_2 = U_{2,\infty}. \quad (4.29)$$

One can recover the results of the single filtered protocol in the limit $\Omega \gg \gamma$. In this regime,

the evolution of the average energy in Eq. (4.26) can be written in the following form:

$$\frac{5}{2\Omega}\partial_t^2 U_2 + \left(1 + \frac{5\gamma}{\Omega}\right)\partial_t U_2 + \left(2\gamma + \frac{4\gamma^2}{\Omega}\right)U_2 = \hbar\omega\left(\lambda + \frac{\gamma^2}{4\lambda}\right) + \frac{\hbar\omega}{\Omega}\left(4\gamma\lambda + \frac{\gamma^3}{4\lambda}\right). \quad (4.30)$$

In this limit, the system will relax to the following asymptotic energy

$$\langle\hat{H}_2\rangle_\infty = \frac{\hbar\omega}{2}\left(\frac{\lambda}{\gamma} + \frac{\gamma}{4\lambda}\right) + \frac{\hbar\omega}{\Omega}\left(\lambda - \frac{\gamma^2}{8\lambda}\right). \quad (4.31)$$

Note that the Eqs. (4.30) and (4.31) are equal to the Eqs. (4.22) and (4.23), respectively, up to zeroth order in $1/\Omega$.

While Eq. (4.27) reveals that no choice of parameters achieves ground state cooling, we can use Eq. (4.31) to cool down the particle to a lower energy than the single layer of filter protocol if our small correction is negative. The first order correction of Eq. (4.31) is negative if

$$\frac{\gamma}{\lambda} > 2\sqrt{2}. \quad (4.32)$$

These results show an interesting feature of this system. We can achieve better cooling by introducing another filtering layer on top of the original noisy signal if the parameters γ and λ satisfy Eq. (4.32). We will discuss the experimental consequences of this result in the next sections.

4.5.3 Three layers of filtering

Here, we will focus on the feedback Hamiltonian given by

$$\hat{H}_3(\mathbf{D}_3) = \frac{\hbar\omega}{2} [(\hat{p} - D_{p,3})^2 + (\hat{x} - D_{x,3})^2]. \quad (4.33)$$

Now, having three layers of filtering, the system of equations necessary to solve for the energy is substantially more complex (see Appendix 4C). We have nine linearly coupled equations to solve, so we will only focus on the asymptotic energy.

The asymptotic energy for cooling protocol with three layers of filtering is given by

$$\langle \hat{H}_3 \rangle_\infty = \frac{\frac{\hbar\omega}{2} \left(\begin{aligned} &8\lambda^2\Omega^3(\omega^2 + \Omega^2)^2 + 8\gamma\lambda^2\Omega^2(3\omega^4 + 7\omega^2\Omega^2 + 8\Omega^4) \\ &+ \gamma^5[\Omega^4 + 4\lambda^2(\omega^2 + 5\Omega^2)] + 2\gamma^4[2\Omega^5 + \lambda^2(9\omega^2\Omega + 48\Omega^3)] \\ &\quad + \gamma^3[5\Omega^6 + 4\lambda^2(\omega^4 + 10\omega^2\Omega^2 + 45\Omega^4)] \\ &\quad + 2\gamma^2[\Omega^7 + \lambda^2(9\omega^4\Omega + 31\omega^2\Omega^3 + 80\Omega^5)] \end{aligned} \right)}{2\gamma\lambda\Omega^2 \left(\begin{aligned} &4\gamma^4\Omega - 4\omega^2\Omega^3 + 4\Omega^5 - 2\gamma^3(\omega^2 - 8\Omega^2) + \gamma^2(-9\omega^2\Omega + 24\Omega^3) \\ &\quad + 4\gamma(-3\omega^2\Omega^2 + 4\Omega^4) \end{aligned} \right)}. \quad (4.34)$$

Because the system is hard to solve analytically, I don't have the exact solution for which choices of parameters $(\omega, \gamma, \lambda, \Omega)$ allow for the system to relax to the solution in Eq. (4.34). However, if we focus in the limit $\Omega \gg \omega, \gamma, \lambda$, we expect the solution to be close to the single-layer protocol.

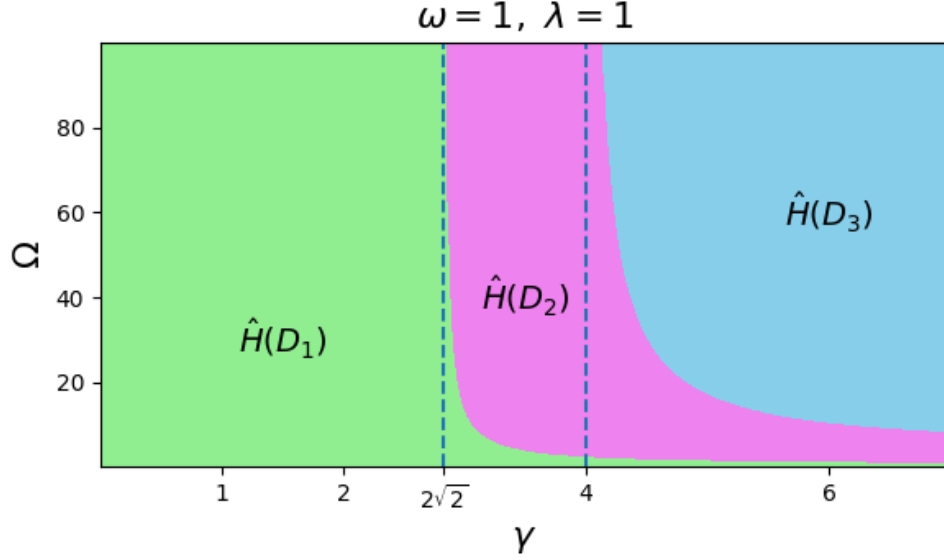


Figure 4.2: Phase diagram indicating which protocol is able to cool down the particle to the lowest energy for a given value of (γ, Ω) . Each region indicates which protocol yields the lowest energy using Eqs. (4.23,4.27,4.34). The vertical dashed lines indicate the transition regions where the second protocol is the coldest for $2\sqrt{2} < \gamma/\lambda < 4$, and where the third protocol is the coldest for $\gamma/\lambda > 4$ [see Eq. (4.37)].

In the limit $\Omega \rightarrow \infty$ we get

$$\langle \hat{H}_3 \rangle_\infty = \frac{\hbar\omega}{2} \left(\frac{\lambda}{\gamma} + \frac{\gamma}{4\lambda} \right) + \frac{\hbar\omega}{\Omega} \left(2\lambda - \frac{3\gamma^2}{16\lambda} \right). \quad (4.35)$$

Note that this protocol yields lower asymptotic energy than the single-layer protocol in Eq. (4.23),

if

$$\frac{\gamma}{\lambda} > 2\sqrt{\frac{8}{3}}\lambda. \quad (4.36)$$

When we combine Eqs. (4.31) and (4.35), we can solve for which regions of the parameter

space (γ, λ) we get better cooling with each of the three protocols:

$$\Omega \rightarrow \infty : \begin{cases} \gamma/\lambda \leq 2\sqrt{2} : & \min(\langle \hat{H}_{1,2,3} \rangle_\infty) = \langle \hat{H}_1 \rangle_\infty \\ 2\sqrt{2} < \gamma/\lambda \leq 4 : & \min(\langle \hat{H}_{1,2,3} \rangle_\infty) = \langle \hat{H}_2 \rangle_\infty \\ \gamma/\lambda > 4 : & \min(\langle \hat{H}_{1,2,3} \rangle_\infty) = \langle \hat{H}_3 \rangle_\infty \end{cases} \quad (4.37)$$

Using the table in Eq. (4.37), one can design the experiment to artificially filter the measurement signal and apply feedback based on a n -filtered signal. This cleaner signal can yield better cooling if the parameters γ/λ cannot be controlled easily.

4.5.4 Multiple layers of filtering

As we can see from the analytical results in Eq. (4.27) and Eq. (4.34), the complexity of the equations increases as we add more layers of signal filter to apply feedback. For $n > 3$, we don't have analytical results for the asymptotic energy after cooling. However, using trajectory simulations, we can probe the asymptotic energy in the limit of $\Omega \rightarrow \infty$. Define the separation of the timescale correction function

$$\alpha_n(\gamma, \lambda) \equiv \frac{\Omega}{\lambda} \lim_{\Omega \rightarrow \infty} \left(\frac{\langle \hat{H}_n \rangle_\infty - \langle \hat{H}_1 \rangle_\infty}{\hbar\omega} \right). \quad (4.38)$$

We have the exact form of these functions for $n = 2, 3$:

$$\alpha_2(\gamma, \lambda) = 1 - \frac{\gamma^2}{8\lambda^2}, \quad (4.39)$$

$$\alpha_3(\gamma, \lambda) = 2 - \frac{3\gamma^2}{16\lambda^2}. \quad (4.40)$$

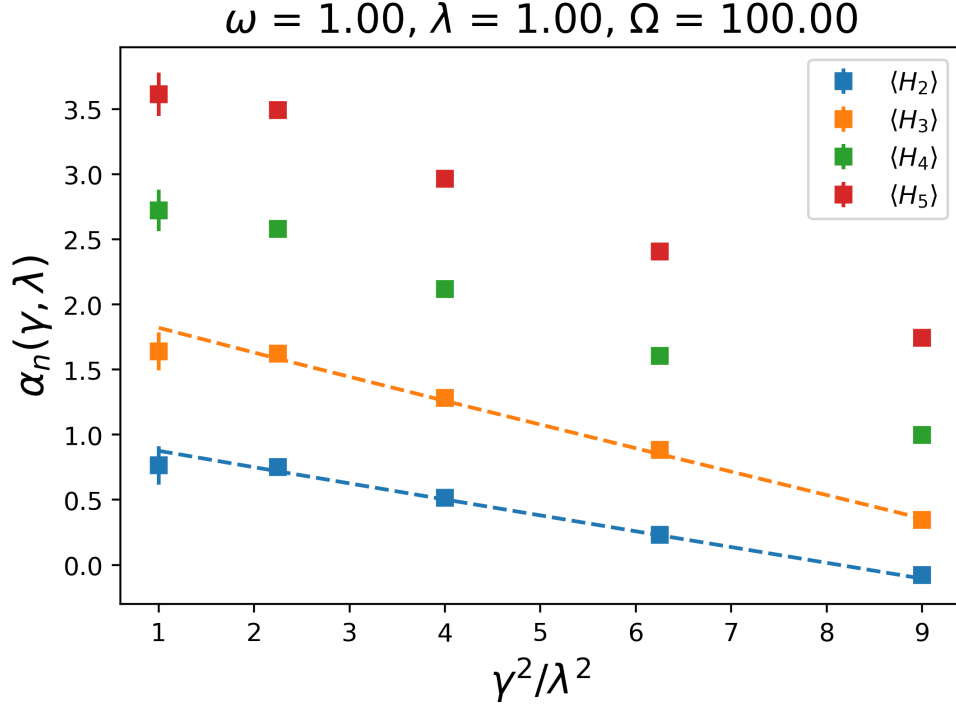


Figure 4.3: Separation of timescale correction function α_n plotted for various values of γ^2/λ^2 . The mean value of the correction function for $N = 5000$ trajectories agrees with the analytical expressions in Eqs. (4.39,4.40) within statistical error (Standard Error of the Mean).

In Fig. 4.3, we show the result of the ensemble of stochastic trajectories simulation. Note that the numerical solution for $\alpha_n(\gamma, \lambda)$ matches Eqs. (4.39) and (4.40). For $n > 3$, the functions obey the same pattern: a linear decreasing function in γ^2/λ^2 . This numerical result extends Eq. (4.37), and experimentalists can use it to design artificial filters that can improve the overall cooling efficiency of the protocol.

4.5.5 Band-pass filter

A similar analysis can be done using the band-pass filter master equation in (4.10) with a protocol given by

$$\hat{H}(\mathbf{E}_1) = \frac{\hbar\omega}{2} [(\hat{p} - E_{p,1})^2 + (\hat{x} - E_{x,1})^2]. \quad (4.41)$$

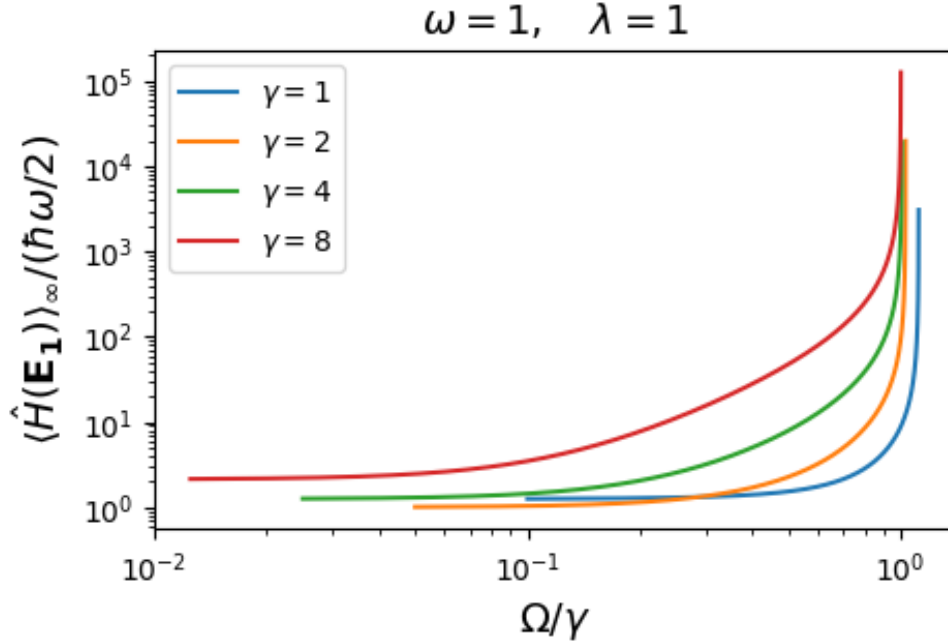


Figure 4.4: Asymptotic normalized energy for cooling a quantum harmonic oscillator using a band-pass filtering process. Equation (4.41) is plotted as a function of Ω/γ . For larger values of Ω/γ , the energy diverges and then takes unphysical values (not shown).

The lack of symmetries in the equations of motion for this system (see Appendix 4C) makes its solution hard to interpret. The asymptotic ensemble energy for the cooling of a quantum harmonic oscillator with band-pass filtering is

$$\langle \hat{H}(\mathbf{E}_1) \rangle_\infty = \frac{\hbar\omega}{2} \left(\frac{\lambda}{\gamma} + \frac{\gamma}{4\lambda} \right) \left[1 + \frac{\Omega^2 (4\gamma^2 - \omega^2 + 4\Omega^2)}{\omega^2 (4\gamma^2 + \omega^2 - 4\Omega^2)} \right] + \frac{\hbar\omega}{2} \frac{\gamma\Omega^2 (3\omega^2 - 4\gamma^2 - 4\Omega^2)}{4\lambda\omega^2 (4\gamma^2 + \omega^2 - 4\Omega^2)}. \quad (4.42)$$

It is intuitive to see that the lowest order of contribution is Ω^2 when $\Omega \rightarrow 0$, because $\cos \Omega(t-s) \approx 1 - \Omega^2(t-s)^2/2$ in Eq. (4.6). I couldn't solve for the conditions on the parameters $(\omega, \gamma, \lambda, \Omega)$ for the system of equations to converge. However, it is not hard to check that for very large values of Ω , Eq. (4.41) can yield unphysical values, namely $\langle \hat{H}(\mathbf{E}_1) \rangle_\infty \leq \hbar\omega/2$. In Figure 4.4, one can check that all curves diverge for $\Omega/\gamma \approx 1$, and for larger values of Ω/γ , the

energy has negative values (not included in the plot).

4.6 Discussion and concluding remarks

In this chapter, we extended the results derived by Annby-Andersson in [1] by considering general filtering of the measurement outcome signal. The special cases of low-pass and band-pass filters are considered and applied to the same toy model used in Chapter 3. Analytical results were derived and discussed in detail.

The results presented in Sec. 4.5 show a promising avenue for experiment design. The analytical results show that adding a low-pass filter can have a non-trivial influence on the system's cooling capacity. The amount of cooling is controlled by the ratio γ/λ . This parameter represents the ratio of how fast information can be processed divided by how much information is collected. The optimal condition happens at $\gamma/\lambda = 2$, and the single-layer protocol can yield ground-state cooling. As we increase the ratio γ/λ , the stochastic term in Eq. (2.25) increases in magnitude, and less noise is filtered. Thus, adding another low-pass filter, or more generally, modifying the spectral properties of the filter, can yield a more precise application of the protocol.

By increasing the parameter space of the model, here done by adding more layers of filtering to the QFPME, I showed that one can derive interesting phase diagrams that represent situations where the protocol is applied with better cooling results. This parameter-space increase can be a powerful tool for experimentalists who can use the analytical/numerical solution of the QFPME to choose regimes of operations and parameters to enhance the performance of quantum feedback protocols.

Finally, this chapter also derives a general form of the QFPME that can be used to model

more precisely the complex structure of an experiment's information processing and measurement protocol. The aim is to have ways for experimentalists to describe the exact spectral properties of their signals using the QFPME with general filters and, in doing so, have a powerful theoretical tool to simulate the evolution of their feedback system. The analytical strategies used in this chapter can also help derive exact results for asymptotic solutions for the expectation values of important quantities of the system. For quadratic Hamiltonians, it is possible to close the equations of motion and get a simple set of equations whose solution describes the quantum system's energy, position, and momentum.

I hope the results presented here motivate using master equations to study experimental implementations of continuous quantum feedback systems. These systems were historically studied using stochastic equations. Here, I present the general theory and particular examples that illustrate how much information can be gained by focusing on ensemble averages over many trajectories of the experiment. In some cases, it is possible to use the ensemble picture to optimize the experiment's parameters and obtain non-trivial conditions where the protocol is enhanced.

4A Deriving the general QFPME

Here, I will derive the most general form of the QFPME in Eq. (4.19). The setup is similar to the previous derivation outlined in Sec. 2.4. The stochastic equations that one needs to consider are the Belavkin equation and the general SDE for the filters:

$$d\hat{\rho} = \frac{-i}{\hbar} \left[\hat{H}(\mathbf{G}), \hat{\rho} \right] dt + \lambda \mathcal{D}[\hat{A}] \hat{\rho} dt + \sqrt{\lambda} dW \{ \hat{A} - \langle \hat{A} \rangle, \hat{\rho} \} \quad (4.A1)$$

$$dG'_k = b_k \left(\langle \hat{A} \rangle + \frac{1}{\sqrt{4\lambda}} \frac{dW}{dt} \right) dt + \sum_{j=1}^n M_{kj} G'_j dt, \quad k = 1, \dots, n. \quad (4.A2)$$

Here, the matrix \mathbf{M} and the vector \mathbf{b} fully specify the model of the filter. See Appendix 4B for a discussion on how to model the low-pass and band-pass filters using this convention.

The object one needs to focus on to derive the general QFPME is the joint distribution over the trajectories (realizations of the stochastic variable dW) that are consistent with the measurement outcome $\mathbf{G}(t) = (G_1(t), \dots, G_n(t))$:

$$\hat{\rho}(\mathbf{G}, t) = E_W \left[\hat{\rho}(t) \prod_{k=1}^n \delta(G'_k(t) - G_k) \right]. \quad (4.A3)$$

The infinitesimal evolution of Eq. (4.A3) can be calculated using Ito's rule of stochastic calculus:

$$\begin{aligned}
d\hat{\rho}(\mathbf{G}) = \mathbb{E}_{\mathbf{W}} \left[d\hat{\rho} \prod_{k=1}^n \delta(G'_k(t) - G_k) + \hat{\rho} \sum_k d\delta(G'_k(t) - G_k) \prod_{j \neq k}^n \delta(G'_j(t) - G_j) + \right. \\
\left. d\hat{\rho} \sum_k d\delta(G'_k(t) - G_k) \prod_{j \neq k}^n \delta(G'_j(t) - G_j) + \right. \\
\left. \hat{\rho} \sum_k \sum_{j \neq k} d\delta(G'_k(t) - G_k) d\delta(G'_j(t) - G_j) \prod_{i \neq k, j}^n \delta(G'_i(t) - G_i) \right] \quad (4.A4)
\end{aligned}$$

$$\begin{aligned}
d\hat{\rho}(\mathbf{G}) = \mathbb{E}_{\mathbf{W}} \left[\frac{-i}{\hbar} [\hat{H}(\mathbf{G}), \hat{\rho}(\mathbf{G})] dt + \lambda \mathcal{D}[\hat{A}] \hat{\rho}(\mathbf{G}) dt + \sqrt{\lambda} dW \{ \hat{A} - \langle \hat{A} \rangle, \hat{\rho}(\mathbf{G}) \} + \right. \\
\left. \hat{\rho} \sum_{k=1}^n \delta'(G'_k(t) - G_k) \left(b_k \langle \hat{A} \rangle dt + \frac{b_k dW}{\sqrt{4\lambda}} + \sum_j M_{kj} G'_j dt \right) \prod_{i \neq k} \delta(G'_i(t) - G_i) \right. \\
\left. + \hat{\rho} \sum_{k=1}^n \frac{1}{2} \delta''(G'_k(t) - G_k) \frac{b_k^2}{4\lambda} dt \prod_{i \neq k} \delta(G'_i(t) - G_i) + \right. \\
\left. \sqrt{\lambda} \{ \hat{A} - \langle \hat{A} \rangle, \hat{\rho} \} \sum_{k=1}^n \delta'(G'_k(t) - G_k) \frac{b_k}{\sqrt{4\lambda}} \prod_{j \neq k} \delta(G'_j(t) - G_j) dt + \right. \\
\left. \hat{\rho} \sum_k \sum_{j \neq k} \delta'(G'_k(t) - G_k) \delta'(G'_j(t) - G_j) \frac{b_k b_j}{4\lambda} dt \prod_{i \neq k, j}^n \delta(G'_i(t) - G_i) \right] \quad (4.A5)
\end{aligned}$$

The stochastic terms can be neglected using $\mathbb{E}_{\mathbf{W}}[dW] = 0$:

$$\begin{aligned}
d\hat{\rho}(\mathbf{G}) = \mathbb{E}_{\mathbf{W}} \left[\frac{-i}{\hbar} [\hat{H}(\mathbf{G}), \hat{\rho}(\mathbf{G})] dt + \lambda \mathcal{D}[\hat{A}] \hat{\rho}(\mathbf{G}) dt + \right. \\
\left. \sum_{k=1}^n \delta'(G'_k(t) - G_k) \frac{1}{2} \left\{ b_k \hat{A} dt + \sum_j M_{kj} G'_j dt, \hat{\rho} \right\} \prod_{i \neq k} \delta(G'_i(t) - G_i) \right. \\
\left. + \hat{\rho} \sum_{k=1}^n \frac{1}{2} \delta''(G'_k(t) - G_k) \frac{b_k^2}{4\lambda} dt \prod_{i \neq k} \delta(G'_i(t) - G_i) + \right. \\
\left. \hat{\rho} \sum_k \sum_{j \neq k} \delta'(G'_k(t) - G_k) \delta'(G'_j(t) - G_j) \frac{b_k b_j}{4\lambda} dt \prod_{i \neq k, j}^n \delta(G'_i(t) - G_i) \right] \quad (4.A6)
\end{aligned}$$

The final step is to use the following properties of the delta function [68]:

$$\frac{\partial}{\partial G'} \delta(G' - G) = -\frac{\partial}{\partial G} \delta(G' - G), \quad (4.A7)$$

$$\left[\frac{\partial}{\partial G'} \delta(G' - G) \right] f(G') = \frac{\partial}{\partial G'} [\delta(G' - G) f(G)]. \quad (4.A8)$$

And the master equation derived can be rearranged as in Eq. (4.19):

$$\begin{aligned} \partial_t \hat{\rho}(\mathbf{G}) = & \frac{-i}{\hbar} \left[\hat{H}(\mathbf{G}), \hat{\rho}(\mathbf{G}) \right] + \lambda \mathcal{D}[\hat{A}] \hat{\rho}(\mathbf{G}) - \frac{1}{2} \sum_{k=1}^n \partial_{G_k} \left\{ b_k \hat{A} + \sum_j M_{kj} G'_j, \hat{\rho}(\mathbf{G}) \right\} \\ & + \sum_k \sum_j \frac{b_k b_j}{8\lambda} \frac{\partial^2}{\partial G_k \partial G_j} \hat{\rho}(\mathbf{G}). \end{aligned} \quad (4.A9)$$

Note that I gather the second derivative terms using the property of the cross-second derivative being symmetric.

4B Filtering for specific QFPMEs

All filters used in this Chapter can be written using the generic master equation in Eq. (4.19).

For a sequence of low-pass filters, one can use

$$\mathbf{M} = \begin{pmatrix} -\gamma_1 & 0 & 0 & \dots & 0 \\ \gamma_2 & -\gamma_2 & 0 & \dots & 0 \\ 0 & \gamma_3 & -\gamma_3 & \dots & 0 \\ \vdots & \vdots & & \ddots & \vdots \\ 0 & & \dots & \gamma_n & -\gamma_n \end{pmatrix} \quad \vec{b} = \begin{pmatrix} \gamma_1 \\ 0 \\ \vdots \\ 0 \\ 0 \end{pmatrix}, \quad (4.A10)$$

to recover the master equation in Eq. (4.5).

The QFPME with band-pass filter in Eq. (4.10) can be written using:

$$\mathbf{M} = \begin{pmatrix} -\gamma & -\Omega \\ \Omega & -\gamma \end{pmatrix} \quad \vec{b} = \begin{pmatrix} \gamma \\ 0 \end{pmatrix}. \quad (4.A11)$$

Finally, the master equation (4.15) of a generic analytical filter (4.11) can be written using:

$$\mathbf{M} = \begin{pmatrix} 0 & 1 & 0 & \dots & 0 \\ 0 & 0 & 1 & \dots & 0 \\ \vdots & \vdots & & \ddots & \vdots \\ -a_0 & -a_1 & -a_2 & \dots & -a_{n-1} \end{pmatrix} \quad \vec{b} = \begin{pmatrix} f(0) \\ f^{(1)}(0) \\ \vdots \\ f^{(n-1)} \end{pmatrix}. \quad (4.A12)$$

4C Cooling a quantum harmonic oscillator

In this section, I describe the equations of motion used to derive the results in Sec. 4.5. All results were derived by solving for the asymptotic solution for the system of coupled differential equations that describe the system's energy and all other relevant expected values.

Two-layers of filtering

The asymptotic ensemble energy for the system that evolves under the protocol defined by Eq. (4.21) is calculated by solving for the steady state of the following system:

$$\partial_t \begin{pmatrix} R_1 \\ R_2 \\ R_3 \\ R_4 \end{pmatrix} = \begin{pmatrix} 0 & -\Omega & 0 & 0 \\ 2\gamma & -(\Omega + \gamma) & -\Omega & -\omega \\ 0 & 2\gamma & -2(\Omega + \gamma) & 0 \\ 0 & \omega & 0 & -(\Omega + \gamma) \end{pmatrix} \begin{pmatrix} R_1 \\ R_2 \\ R_3 \\ R_4 \end{pmatrix} + \begin{pmatrix} \lambda \\ 0 \\ \frac{\gamma^2}{2\lambda} \\ 0 \end{pmatrix} \quad (4.A13)$$

Each element of the vector $\vec{R} = (R_1, \dots, R_4)^T$ is given by a expected value:

$$\begin{pmatrix} R_1 \\ R_2 \\ R_3 \\ R_4 \end{pmatrix} = \begin{pmatrix} \langle \hat{H}_2 \rangle / \hbar\omega \\ \langle (\hat{x} - D_{x,2})(D_{x,1} - D_{x,2}) \rangle + \langle (\hat{p} - D_{p,2})(D_{p,1} - D_{p,2}) \rangle \\ \langle (D_{x,1} - D_{x,2})^2 \rangle + \langle (D_{p,1} - D_{p,2})^2 \rangle \\ \langle (\hat{x} - D_{x,2})(D_{p,1} - D_{p,2}) \rangle - \langle (\hat{p} - D_{p,2})(D_{x,1} - D_{x,2}) \rangle \end{pmatrix}. \quad (4.A14)$$

One can solve for $\langle \hat{H}_2 \rangle_\infty$ by setting $\partial_t \vec{R} = 0$ to get Eq. (4.27). Equation (4.26) can be calculated by taking higher order derivatives of this system of equations to isolate the equation for the internal energy.

Three-layers of filtering

The asymptotic energy in Eq. (4.34) can be calculated by setting $\partial_t \vec{S} = 0$, in the following

system of equations:

$$\partial_t \vec{S} = \begin{pmatrix} 0 & -\Omega & 0 & 0 & 0 & 0 & 0 & 0 & 0 \\ 0 & -\Omega & \omega & -\Omega & \Omega & 0 & 0 & 0 & 0 \\ 0 & -\omega & -\Omega & 0 & 0 & \Omega & 0 & 0 & 0 \\ 0 & 0 & 0 & -2\Omega & 0 & 0 & 2\Omega & 0 & 0 \\ 2\gamma & -\gamma & 0 & 0 & -(\gamma + \Omega) & \omega & -\Omega & 0 & 0 \\ 0 & 0 & -\gamma & 0 & -\omega & -(\gamma + \Omega) & 0 & -\Omega & 0 \\ 0 & \gamma & 0 & -\gamma & 0 & 0 & -(2\Omega + \gamma) & 0 & \Omega \\ 0 & 0 & -\gamma & 0 & 0 & 0 & 0 & -(2\Omega + \gamma) & 0 \\ 0 & 0 & 0 & 0 & 2\gamma & 0 & -2\gamma & 0 & -2(\Omega + \gamma) \end{pmatrix} \vec{S} + \begin{pmatrix} \lambda \\ 0 \\ 0 \\ 0 \\ 0 \\ 0 \\ 0 \\ 0 \\ \frac{\gamma^2}{2\lambda} \end{pmatrix} \quad (4.A15)$$

$$\begin{pmatrix} S_1 \\ S_2 \\ S_3 \\ S_4 \\ S_5 \\ S_6 \\ S_7 \\ S_8 \\ S_9 \end{pmatrix} = \begin{pmatrix} \langle \hat{H}_3 \rangle / \hbar\omega \\ \langle (\hat{x} - D_{x,3})(D_{x,2} - D_{x,3}) \rangle + \langle (\hat{p} - D_{p,3})(D_{p,2} - D_{p,3}) \rangle \\ \langle (\hat{p} - D_{p,3})(D_{x,2} - D_{x,3}) \rangle - \langle (\hat{x} - D_{x,3})(D_{p,2} - D_{p,3}) \rangle \\ \langle (D_{x,2} - D_{x,3})^2 \rangle + \langle (D_{p,2} - D_{p,3})^2 \rangle \\ \langle (\hat{x} - D_{x,3})(D_{x,1} - D_{x,2}) \rangle + \langle (\hat{p} - D_{p,3})(D_{p,1} - D_{p,2}) \rangle \\ \langle (\hat{p} - D_{p,3})(D_{x,1} - D_{x,2}) \rangle - \langle (\hat{x} - D_{x,3})(D_{p,1} - D_{p,2}) \rangle \\ \langle (D_{x,1} - D_{x,2})(D_{x,2} - D_{x,3}) \rangle + \langle (D_{p,1} - D_{p,2})(D_{p,2} - D_{p,3}) \rangle \\ \langle (D_{p,2} - D_{p,3})(D_{x,1} - D_{x,2}) \rangle - \langle (D_{x,2} - D_{x,3})(D_{p,1} - D_{p,2}) \rangle \\ \langle (D_{x,1} - D_{x,2})^2 \rangle + \langle (D_{p,1} - D_{p,2})^2 \rangle \end{pmatrix}. \quad (4.A16)$$

Band-pass filtering

The asymptotic energy of the band-pass filter system in Eq. (4.42) can be calculated by

solving:

$$\partial_t \begin{pmatrix} T_1 \\ T_2 \\ T_3 \\ T_4 \\ T_5 \\ T_6 \\ T_7 \\ T_8 \\ T_9 \end{pmatrix} = \begin{pmatrix} -2\gamma & \Omega & 0 & 0 & 0 & 0 & 0 & 0 & 0 \\ 0 & -2\gamma & -\omega & \Omega & \Omega & 0 & 0 & 0 & 0 \\ 0 & \omega & -2\gamma & 0 & 0 & \Omega & 0 & 0 & 0 \\ 0 & 0 & 0 & -2\gamma & 0 & 0 & 2\Omega & 0 & 0 \\ 2\gamma & -\Omega & 0 & 0 & -\gamma & -\omega & \Omega & 0 & 0 \\ 0 & 0 & -\Omega & 0 & \omega & -\gamma & 0 & \Omega & 0 \\ 0 & \gamma & 0 & -\Omega & 0 & 0 & -\gamma & 0 & \Omega \\ 0 & 0 & -\gamma & 0 & 0 & 0 & 0 & -\gamma & 0 \\ 0 & 0 & 0 & 0 & 2\gamma & 0 & -2\Omega & 0 & 0 \end{pmatrix} \vec{T} + \begin{pmatrix} \frac{1}{2} \left(\frac{\lambda}{\gamma} + \frac{\gamma}{4\lambda} \right) \\ 0 \\ 0 \\ 0 \\ -\frac{\gamma^2}{2\lambda} \\ 0 \\ 0 \\ 0 \\ \frac{\gamma^2}{2\lambda} \end{pmatrix} \quad (4.A17)$$

$$\begin{pmatrix} T_1 \\ T_2 \\ T_3 \\ T_4 \\ T_5 \\ T_6 \\ T_7 \\ T_8 \\ T_9 \end{pmatrix} = \begin{pmatrix} \langle \hat{H}(\mathbf{E}_1) \rangle / \hbar\omega \\ \langle (\hat{x} - E_{x,1})E_{x,2} \rangle + \langle (\hat{p} - E_{p,1})E_{p,2} \rangle \\ \langle (\hat{x} - E_{x,1})E_{p,2} \rangle - \langle (\hat{p} - E_{p,1})E_{x,2} \rangle \\ \langle E_{x,2}^2 + E_{p,2}^2 \rangle \\ \langle (\hat{x} - E_{x,1})E_{x,1} \rangle + \langle (\hat{p} - E_{p,1})E_{p,1} \rangle \\ \langle (\hat{x} - E_{x,1})E_{p,1} \rangle - \langle (\hat{p} - E_{p,1})E_{x,1} \rangle \\ \langle E_{x,1}E_{x,2} + E_{p,1}E_{p,2} \rangle \\ \langle E_{x,2}E_{p,1} - E_{p,2}E_{x,1} \rangle \\ \langle E_{x,1}^2 + E_{p,1}^2 \rangle \end{pmatrix} \cdot \quad (4.A18)$$

Chapter 5: Predicting temperature and atom number using machine learning

This chapter is based on collaborative work with Brady Egleston, Dario D'Amato, Michael Doris, Justyna Zwolak, and Ian Spielman [4]. This work was done at Minilab, part of Spielman's group at NIST Gaithersburg. This project aims to use machine learning to predict the temperature and number of atoms of an ensemble of cooled potassium-39 atoms. In this project, we collected experimental data, developed a numerical analysis pipeline to extract physical parameters from the experiment, and trained various models to learn those physical parameters. We show that it is possible to learn the temperature and the number of atoms from fluorescence images with good precision. My contribution to this project was on the numerical analysis to estimate the number of atoms and the temperature of the cold cloud of atoms. I also contributed to the machine learning component of the study by training all models and testing different architectures to predict the physical parameters.

So far, this thesis has focused on quantum control and feedback. Here, the focus is on the measurement and estimation. Using machine learning, we demonstrate that the properties of an atomic cloud system can be calculated in real-time. Extracting these parameters from fluorescence images without invasive measurements opens the door to closed-loop control strategies. Real-time estimation of system's properties is a crucial step towards implementing advanced quantum feedback control schemes. Precise knowledge of atom number and temperature enables

dynamic adjustments of cooling parameters, potentially improving the efficiency and stability of the trapping process.

5.1 Introduction

In recent years, many ground-breaking discoveries have been made in laser physics [21, 22], the cooling of neutral atoms [19, 20], Bose-Einstein condensates (BEC) [23, 24], and the precise control of quantum systems [163, 193, 194]. Many of these studies started novel research areas and motivated the development of new technologies. In particular, the cooling, trapping, and control of neutral atoms are essential for some quantum computing platforms [32–34] and atomic clock technology [25, 26].

The semiclassical theory [195, 196] for cooling neutral particles with light is described in terms of the atom’s absorption and emission of photons. The simplified idea is that when the atom absorbs a photon, it gets “kicked” in momentum space by an amount $\hbar\mathbf{k}$, see Fig. 5.1. After some characteristic time, the photon will be re-emitted in a random direction, causing the average effect to be the change in momentum in the laser propagation direction.

However, because the atom is moving with respect to the laser, it feels a different frequency in its rest frame (Doppler shift). This causes the absorption probability to be dependent on the velocity. If two counterpropagating lasers are used, the net effect is that the radiation force depends linearly on the velocity [196]. This dependence creates an effective friction or “viscous” media for the atoms to move in, causing the desired cooling effect. This stochastic process leads to a Brownian motion in momentum space that describes the momentum relaxation towards cooling [197, 198]. The theoretical cooling limit in this model is given by the Doppler limit,

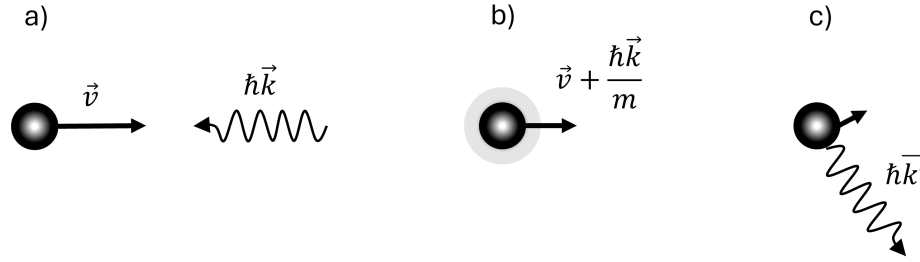


Figure 5.1: Atom absorbing and re-emitting a photon. a) The atom has initial velocity \vec{v} and the photon carries momentum $\hbar\vec{k}$. b) the atom absorbs the photon and goes to an excited state while changing its velocity by $\hbar\vec{k}/m$. c) after a decaying timescale, the atom re-emits the photon in a random direction and gets a new kick in momentum.

which is the amount of recoil the atom experiences after absorbing the photon [199].

The Doppler shift poses another limitation on the cooling effect: the atoms are effectively transparent to the laser if their velocities cause a large detuning between the resonance frequency and the laser frequency. This problem motivated the development of laser-chirping techniques and the Zeeman slower [200–205]. The latter uses magnetic fields to change the resonance frequency of the atoms to keep them close to the laser frequency as their velocity changes in the cooling process.

The cooling technique that employs the velocity-dependent force using counter-propagating lasers, as described, is referred to as *Optical molasses*, as it creates a viscous medium for the atoms and dissipates kinetic energy [196, 206]. To trap the atoms, one needs to create a position-dependent force, which is typically done using magnetic fields. Using a similar idea to the Zeeman slower, it is possible to create a magnetic field gradient that increases the likelihood of absorption towards the trap's center. Now, one needs to consider the polarization of the lasers to induce the correct transition if the atom is on one side of the trap or the other. The combination of radiation pressure from the laser and the position-dependent energy splitting configures the standard technique for cooling and trapping, typically referred to as magneto-optical trap (MOT)

[206–208].

Surprisingly, temperatures much lower than the Doppler limit were reported for sodium atoms trapped in a MOT configuration [209]. This unexpected result was later explained by a new sub-Doppler cooling mechanism. The laser polarization and the internal atomic structure give rise to a “Sisyphus” cooling (or polarization-gradient cooling), where atoms repeatedly climb potential energy hills, losing kinetic energy in the process [210–212]. Today, the standard MOT cooling techniques can create clouds with typical temperatures of a few millikelvins containing around 10^9 atoms in a region of a few millimeters. Over the years, new approaches have been developed, and some systems can be cooled down to the order of nanokelvin or below.

The last century was also marked by the development of computation theory [213]. In the 1950s, the concept of artificial intelligence (AI) emerged as a system capable of performing tasks that typically require human intelligence, such as reasoning, problem-solving, perception, and learning. In a subset of this broad definition, we have machine learning (ML) that focuses on developing algorithms that allow computers to learn patterns and make predictions or decisions based on data. Throughout this work, I will focus on a particular tool called a neural network (NN). The building blocks for NNs are the perceptrons, which were developed as an information model of biological neurons [214, 215]. A combination of perceptrons creates layers, and the layers can be stacked to create NNs. In principle, a wide and deep enough NN can approximate any function [216, 217]. This property enables NNs to learn patterns from data and approximate unknown functions, mapping inputs to outputs.

The connection between ML and physics dates back to the 1980s [218] with work from Hopfield connecting NNs with statistical physics. Nowadays, with the increase in computational power and the development of modern numerical techniques, the use of ML in sciences is

widespread [219]. Recent applications can be found from the control of quantum devices [220] to the study of black holes [221], and everything in between. The general goal is to obtain hidden information and to learn patterns that can sometimes be unexpected for human intuition [222]. Our focus is similar: to estimate the physical parameters of laser-cooled atoms from non-destructive fluorescence imaging, which only captures scattered light during the cooling process. These images are typically only used to study the spatial structure of the clouds and reveal no direct access to properties like temperature. Here, we demonstrate that ML can extract the hidden physical properties of clouds generated from real experimental data.

During the cooling and trapping stages of a MOT, the atoms constantly scatter light from the lasers. Imaging this fluorescence allows for a noninvasive mechanism of monitoring the trapped cloud. In the low-density limit of the cloud, the overall fluorescence is expected to be proportional to the atom number [223]. However, there is no obvious correlation between the properties of the fluorescence imaging and the temperature of the cloud. This parameter is usually determined from time-of-flight (TOF) imaging, in which the atoms are freed from the MOT and allowed to ballistically expand for a set time. The evolution correlates the spatial distribution with the velocity distribution, from which the temperature is estimated.

In this chapter, I focus on calculating the properties of neutral potassium-39 atoms trapped in a MOT configuration. These properties are first determined using standard techniques and later estimated using ML. I show that one can recover the temperature and the number of atoms of atomic clouds using NNs. This chapter is organized as follows: in Sec. 5.2, I describe the theoretical methods to reconstruct the velocity distribution and estimate the temperature of the atomic cloud. Section 5.3 describes the pipeline from the data collection to the model training. In Sec. 5.4, I briefly describe the experimental setup to generate the atomic clouds. Then, Sec. 5.5

describes the data acquisition and labeling process. Section 5.6 shows the regression models used to infer the physical parameters. In Sec. 5.7, I present the results of the ML training. Finally, Sec. 5.8 discusses the results and Sec. 5.9 concludes.

5.2 Methods to estimate the velocity distribution of cold atoms

In this section, I focus on developing robust methods to estimate the temperature of a cold atomic cloud. Assigning a temperature to an atomic cloud assumes that the velocity distribution is uncorrelated with the position distribution and follows Maxwell's thermal distribution. This hypothesis may not be guaranteed, as the preparation stage of a trapped cloud of atoms may leave the particles in a non-thermal equilibrium configuration. Here, I present various methods with increasing complexity that aim to answer the question of how good the thermal assumption is for the data we collected and how to approach this problem using statistical physics.

The present analysis starts by considering that we have access to images representing the position distribution of atoms in a particular cloud. Each cloud is considered to be trapped at $t = 0$ and then released. After some time, τ , we take a picture and repeat the process N times by varying how much time τ we wait in each iteration. Thus, the measured object is a set $\{\rho_{\text{meas},k}, \tau_k\}$ describing the position distribution of atoms $\rho_{\text{meas},k}$ at time τ_k . The goal is to calculate the temperature (or a temperature-like parameter) that best describes the atomic cloud.

Consider the cloud to be composed of non-interacting classical particles. This assumption allows us to write a ballistic expansion for the atoms. The position distribution at any time τ_n can

be related to the initial position distribution and the general velocity distribution

$$\rho_n(x, y) = \int dx_0 dy_0 dv_x dv_y \rho_0(x_0, y_0) \sigma(v_x, v_y | x_0, y_0) \times \delta[x - (x_0 + v_x \tau_n)] \delta[y - (y_0 + v_y \tau_n)]. \quad (5.1)$$

Here, ρ_0 denotes the initial position distribution, and $\sigma(v_x, v_y | x, y)$ denotes the velocity distribution, which can be correlated with position. This evolution can be simplified by integrating the delta functions

$$\rho_n(x, y) = \int dx_0 dy_0 \rho_0(x_0, y_0) \frac{1}{\tau_n^2} \sigma\left(\frac{x - x_0}{\tau_n}, \frac{y - y_0}{\tau_n} \middle| x_0, y_0\right), \quad (5.2)$$

$$\rho_n(x, y) = \int dx_0 dy_0 \rho_0(x_0, y_0) \mathcal{K}_n(x - x_0, y - y_0 | x_0, y_0). \quad (5.3)$$

Here,

$$\mathcal{K}_n(x, y | x_0, y_0) = \frac{1}{\tau_n^2} \sigma\left(\frac{x - x_0}{\tau_n}, \frac{y - y_0}{\tau_n} \middle| x_0, y_0\right), \quad (5.4)$$

defines the physical model and can include correlations and interactions. The Fourier transform of Eq. (5.3) can be written as:

$$\mathcal{F}\{\rho_n\} = \int dx_0 dy_0 \rho_0(x_0, y_0) \int dx dy e^{-ik_x x - ik_y y} \mathcal{K}_n(x - x_0, y - y_0 | x_0, y_0), \quad (5.5)$$

$$= \int dx_0 dy_0 \rho_0(x_0, y_0) e^{-ik_x x_0 - ik_y y_0} \mathcal{F}\{\mathcal{K}_n[x_0, y_0]\}, \quad (5.6)$$

$$= \mathcal{F}\{\rho_0 \mathcal{F}\{\mathcal{K}_n[x_0, y_0]\}\}, \quad (5.7)$$

where the notation $\mathcal{K}_n[x_0, y_0]$ denotes that the kernel \mathcal{K}_n is parametrized by the value (x_0, y_0) .

Note that all results here are derived in terms of continuous functions and integrals over

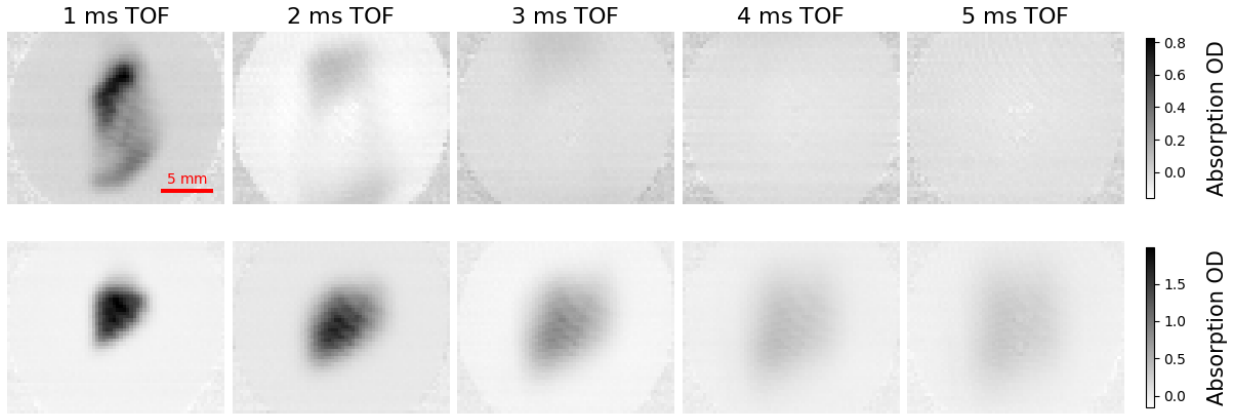


Figure 5.2: Comparison of non-Gaussian and Gaussian shaped clouds. The absorption images are taken after 1 ms – 5 ms of expansion. In the first row, we have the files 2024-02-05 group 0527; in the second row, we have the files 2024-02-04 group 0616. Non-ideal MOTs can expand as two (or more) separate clouds or retain their initial shape for longer times.

real space. For experimental data, the images have a finite resolution, thus everything is extended to the discrete case. Integrals become sums, distributions become probabilities, and so on.

5.2.1 Formal solution using a thermal velocity distribution

In this section, I write the exact solution for the ballistic evolution of an initial ensemble of atoms. The starting point is to consider the initial $t = 0$ distribution of atoms in the Gauss-Hermite basis expansion:

$$\rho_0(x, y) = \left(\frac{1}{2\pi\sigma_{x,0}\sigma_{y,0}} \right) e^{-x^2/2\sigma_{x,0}^2 - y^2/2\sigma_{y,0}^2} \sum_{n,m} \frac{c_{nm}^{(0)}}{2^{n+m}n!m!} H_n \left(\frac{x}{\sqrt{2}\sigma_{x,0}} \right) H_m \left(\frac{y}{\sqrt{2}\sigma_{y,0}} \right), \quad (5.8)$$

$$\int dx dy \rho_0(x, y) H_n \left(\frac{x}{\sqrt{2}\sigma_{x,0}} \right) H_m \left(\frac{y}{\sqrt{2}\sigma_{y,0}} \right) = c_{nm}^{(0)}. \quad (5.9)$$

Note that the Gauss-Hermite functions form a complete basis, so in principle, any well-behaved function can be described by Eq. (5.8). See Fig. 5.2 for two examples of typical cloud distri-

butions. These images represent absorption optical depth measurements of the cloud of atoms; more details on the measurements and the experiment are left for Sec. 5.3.

If the system is in thermal equilibrium, we expect the velocity distribution to be described by the Maxwell's velocity function. In this scenario, the evolution kernel can be written as:

$$\mathcal{K}_n(x, y) = \left(\frac{m}{2\pi k_B \tau_n^2 \sqrt{T_x T_y}} \right) e^{-\frac{m}{2k_B \tau_n^2} (x^2/T_x + y^2/T_y)}. \quad (5.10)$$

The generic evolution of the distribution at time $t = 0$ to a later time $t = \tau$ can be written in terms of the Fourier transformation, as in Eq. (5.7):

$$\mathcal{F}\{\rho_\tau\} = \mathcal{F}\{\rho_0\} e^{-\frac{k_B \tau^2}{2m} (T_x k_x^2 + T_y k_y^2)}. \quad (5.11)$$

To calculate the Fourier transform of the initial distribution, I use the following equation [224, 18.17.21.2]:

$$\frac{1}{\sqrt{\pi}} \int du e^{-u^2} H_n(u) e^{iuy} = (+i)^n e^{-\frac{y^2}{4}} y^n. \quad (5.12)$$

Thus,

$$\mathcal{F}\{\rho_0\} = \frac{1}{2\pi} e^{-\frac{1}{2}k_x^2 \sigma_{x,0}^2 - \frac{1}{2}k_y^2 \sigma_{y,0}^2} \sum_{nm} \frac{c_{nm}^{(0)}}{2^{n+m} n! m!} (-i)^{n+m} \left(\sqrt{2} k_x \sigma_{x,0} \right)^n \left(\sqrt{2} k_y \sigma_{y,0} \right)^m \quad (5.13)$$

Combining both equations, we get:

$$\mathcal{F}\{\rho_\tau\} = \frac{1}{2\pi} e^{-\frac{1}{2}k_x^2 \sigma_{x,\tau}^2 - \frac{1}{2}k_y^2 \sigma_{y,\tau}^2} \sum_{nm} \frac{c_{nm}^{(0)}}{2^{n+m} n! m!} (-i)^{n+m} \left(\sqrt{2} k_x \sigma_{x,0} \right)^n \left(\sqrt{2} k_y \sigma_{y,0} \right)^m, \quad (5.14)$$

using the definition

$$\sigma_{i,\tau}^2 = \sigma_{i,0}^2 + \frac{k_B T_i}{m} \tau^2 \quad i = x, y. \quad (5.15)$$

Now, to take the inverse Fourier transform, we need to use the following (see [224, (18.17.21_21)]):

$$\begin{aligned} \frac{1}{\sqrt{2\pi}} \int dk \left(\sqrt{2}k\sigma \right)^n e^{-\frac{1}{2}k^2\sigma^2} e^{ikx} &= \\ &= \frac{(\sqrt{2}\sigma)^n}{\sigma_\tau} \frac{1}{\sigma_\tau^n} \frac{1}{\sqrt{2\pi}} \int du u^n e^{-\frac{1}{2}u^2} e^{iux/\sigma_\tau} \\ &= \frac{(\sqrt{2}\sigma)^n}{\sigma_\tau} \frac{\sigma_\tau^n}{\sigma_\tau^n} (-i)^n \frac{d^n}{dx^n} \frac{1}{\sqrt{2\pi}} \int du e^{-\frac{1}{2}u^2} e^{iux/\sigma_\tau} \\ &= \frac{(\sqrt{2}\sigma)^n}{\sigma_\tau} (-i)^n \frac{d^n}{dx^n} e^{-x^2/2\sigma_\tau^2} \\ &= \frac{(\sigma)^n}{\sigma_\tau} \frac{(\sqrt{2}\sigma_\tau)^n}{\sigma_\tau^n} (-i)^n \frac{d^n}{dx^n} e^{-x^2/2\sigma_\tau^2} \\ &= \frac{(\sigma)^n}{\sigma_\tau} \frac{(+i)^n}{\sigma_\tau^n} \frac{d^n}{du^n} \left[(-1)^n e^{-u^2} \right] \Big|_{u=x/\sqrt{2}\sigma_\tau} \\ &= \frac{(\sigma)^n}{\sigma_\tau} \frac{(+i)^n}{\sigma_\tau^n} \left[e^{-u^2} H_n(u) \right] \Big|_{u=x/\sqrt{2}\sigma_\tau} \\ &= \frac{(+i)^n}{\sigma_\tau} \left(\frac{\sigma}{\sigma_\tau} \right)^n e^{-x^2/2\sigma_\tau^2} H_n \left(\frac{x}{\sqrt{2}\sigma_\tau} \right). \end{aligned} \quad (5.16)$$

Finally, we get the evolution of a generic atomic distribution to be

$$\begin{aligned} \rho_\tau &= \left(\frac{1}{2\pi \sqrt{\sigma_{x,0}^2 + \frac{k_B \tau^2 T_x}{m}} \sqrt{\sigma_{y,0}^2 + \frac{k_B \tau^2 T_y}{m}}} \right) e^{-\frac{1}{2} \frac{x^2}{\sigma_{x,0}^2 + \frac{k_B \tau^2 T_x}{m}} - \frac{1}{2} \frac{y^2}{\sigma_{y,0}^2 + \frac{k_B \tau^2 T_y}{m}}} \times \\ &\sum_{nm} \frac{c_{nm}^{(0)}}{2^{n+m} n! m!} \left(\sqrt{\frac{\sigma_{x,0}^2}{\sigma_{x,0}^2 + \frac{k_B \tau^2 T_x}{m}}} \right)^n \left(\sqrt{\frac{\sigma_{y,0}^2}{\sigma_{y,0}^2 + \frac{k_B \tau^2 T_y}{m}}} \right)^m \times \\ &H_n \left(\frac{x}{\sqrt{2} \sqrt{\sigma_{x,0}^2 + \frac{k_B \tau^2 T_x}{m}}} \right) H_m \left(\frac{y}{\sqrt{2} \sqrt{\sigma_{y,0}^2 + \frac{k_B \tau^2 T_y}{m}}} \right) \end{aligned} \quad (5.17)$$

The usefulness of this analytical equation is that now we can use it to obtain the unknown

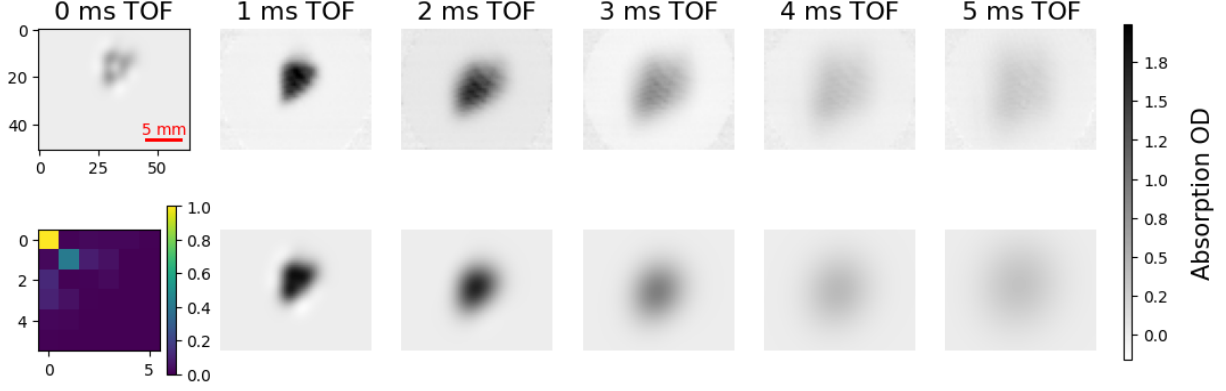


Figure 5.3: Gauss-Hermite fitting of the cloud expansion of the files 2024-02-05 group 0616. The first row contains the original cloud from 1 ms – 5 ms. The second row represents the reconstructed clouds based on the fitted parameters. The first column contains the predicted cloud at $t = 0$ and a heatmap with the absolute values of the Hermite coefficients, as defined in Eq. (5.17).

distribution at time $t = 0$ and the anisotropic temperatures. By fitting all cloud images using this function, one can determine the parameters $(\sigma_{x,0}, \sigma_{y,0}, \{c_{nm}^0\}, T_x, T_y)$ and reconstruct the initial image. So, instead of fitting each MOT image with its own Gauss-Hermite function, we can constraint it to obtain a single Gauss-Hermite expansion that describes all images. The formal solution for the $t = 0$ and the temperature of the cloud can be written as:

$$(\sigma_{x,0}, \sigma_{y,0}, \{c_{nm}^0\}, T_x, T_y)^* = \min_{(\sigma_{x,0}, \sigma_{y,0}, \{c_{nm}^0\}, T_x, T_y)} \sum_k \|\rho_{\text{meas},k} - \rho_{\tau_k}\|^2. \quad (5.18)$$

This general result shows that as $\tau \rightarrow \infty$, all higher order terms in the Gauss-Hermite expansion vanish because of the terms $(\sigma/\sigma_\tau)^n$, which is intuitive as we expect the cloud to look more and more Gaussian as it expands. Equation (5.17) also recovers the typical Gaussian fitting expansion method as a particular case when $c_{nm}^{(0)} = \delta_{n,0}\delta_{m,0}$, or for large values of τ , which explains the use of more straightforward methods that don't account for higher order Hermite coefficients.

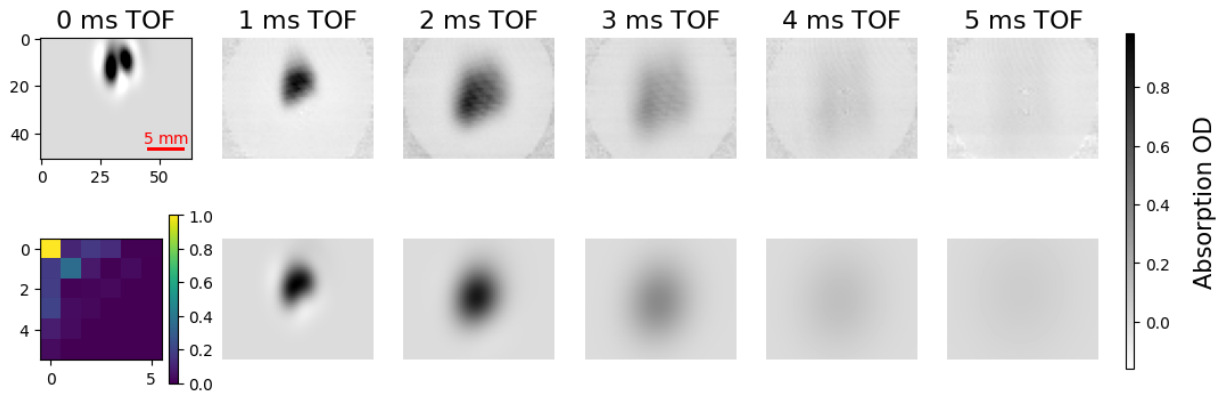


Figure 5.4: Gauss-Hermite fitting of the cloud expansion of the files 2024-02-03 group 1201. The first row contains the original cloud from 1 ms – 5 ms. The second row represents the reconstructed clouds based on the fitted parameters. The fitting was done with maximum degree of 5 for Hermite polynomials.

Figures 5.3 and 5.4 show two distinct examples of the application of Eq. (5.17). Using a minimization routine in Python, it is possible to fit the five input images to determine the temperature, sizes, and Hermite coefficients for the cloud expansion. Those quantities are then used to reconstruct the cloud at $t = 0$, which is inaccessible directly from the experiment. Clouds with an initial Gaussian-like shape (Fig. 5.3) are easier to fit and have a reasonable reconstruction. In the second example, shown in Fig. 5.4, the reconstruction cloud seems good, but the predicted cloud at $t = 0$ contains patterns that are not realistic. Problems like this can be common in fitting routines similar to the ones I use for these results. The non-linear minimizers used in numerical packages do not always yield the best optimal solution.

One explanation for the cloud’s poor reconstruction can be the truncation of the Hermite coefficients in Eq. (5.17). The theoretical approach should be able to define any well-behaved distribution in two dimensions. However, to make the problem numerically tractable, it is necessary to truncate the number of Hermite coefficients (here, I use five as the highest degree). For arbitrary clouds, the minimization routines are often very sensitive to initial conditions.

5.2.2 Velocity kernel using deconvolution

In this section, I use Eq. (5.7), assuming that the velocity and the position are not correlated:

$$\mathcal{F}\{\rho_n\} = \mathcal{F}\{\rho_0\}\mathcal{F}\{\mathcal{K}_n\}. \quad (5.19)$$

However, the form of the velocity kernel is arbitrary, not necessarily a Gaussian distribution with anisotropic temperatures. The idea is to solve a deconvolution problem and obtain the best velocity kernel that evolves the cloud in time [225–227].

Naively, the formal solution is given by

$$\mathcal{K}_n = \mathcal{F}^{-1} \left\{ \frac{\mathcal{F}\{\rho_n\}}{\mathcal{F}\{\rho_0\}} \right\}. \quad (5.20)$$

However, the presence of noise in the convolution problem of Eq. (5.3) can make the denominator in Eq. (5.20) ill-defined. Thus, one needs to use a more sophisticated method called Wiener deconvolution (WD) or Wiener filtering [228, 229].

Before applying it, let's review the basic steps of deriving the WD method. Consider a target image y that satisfy

$$y = h \star x + \epsilon, \quad (5.21)$$

where h is the input image, and x is the convolution kernel for which one wants to solve. Here, ϵ is the noise. Now, considers a deconvolution kernel W that satisfies

$$x = W \star y. \quad (5.22)$$

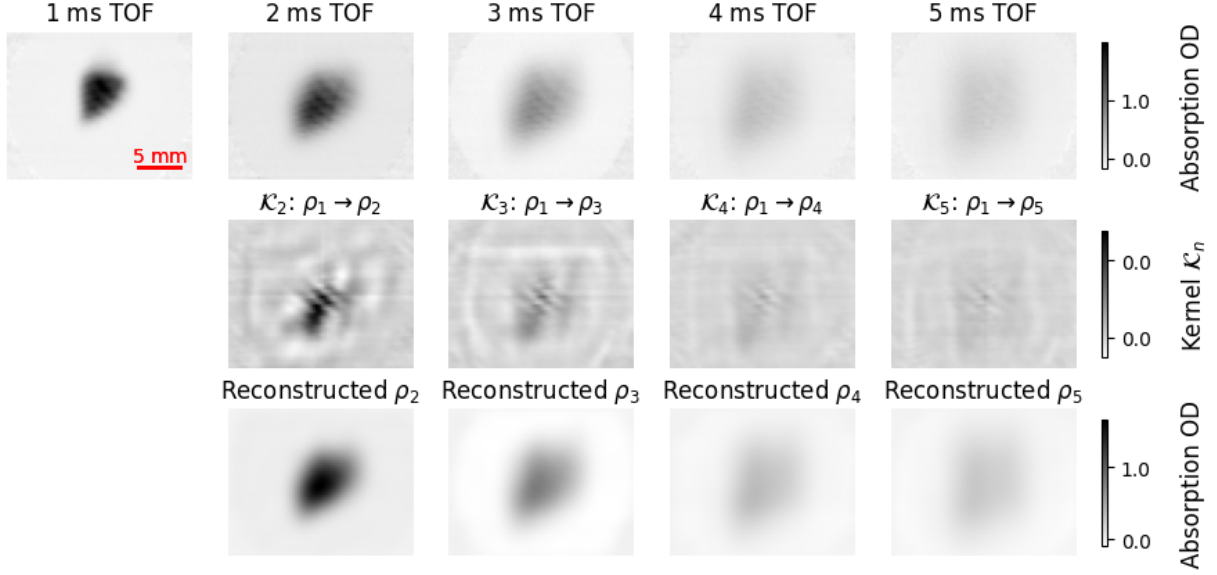


Figure 5.5: Evolution kernel for the clouds defined by the files 2024-02-05 group 0616. The first row is the input images of the cloud’s expansion. The second row contains the kernels calculated using Eq. (5.25), and the third row is the reconstructed image calculated by convolving the initial distribution with the respective kernel.

One can obtain the optimal solution for W by solving the following quadratic minimization problem:

$$\min_W \|\mathcal{F}\{W\}\mathcal{F}\{y\} - \mathcal{F}\{x\}\|^2. \quad (5.23)$$

The solution for the WD kernel is given by

$$x_{\text{WD}} = \mathcal{F}^{-1} \{ \mathcal{F}\{W\}\mathcal{F}\{y\} \}, \quad \mathcal{F}\{W\} = \frac{\mathcal{F}\{h\}^* S}{\|\mathcal{F}\{h\}\|^2 S + 1}, \quad (5.24)$$

where $S = \|\mathcal{F}\{x\}\|^2 / \|\mathcal{F}\{\epsilon\}\|^2$ denotes the Signal-to-Noise ratio (SNR) for convolution kernel. The SNR depends on the unknown kernel x , making the solution in Eq. (5.24) underdefined. Typically, one treats S as a parameter that can be tuned to minimize the prediction error. Conversely, prior knowledge about the statistical properties of the system’s noise can be used. The solution in Eq. (5.24) recovers the naive solution in Eq. (5.20) for the case of $S \rightarrow \infty$, as expected.

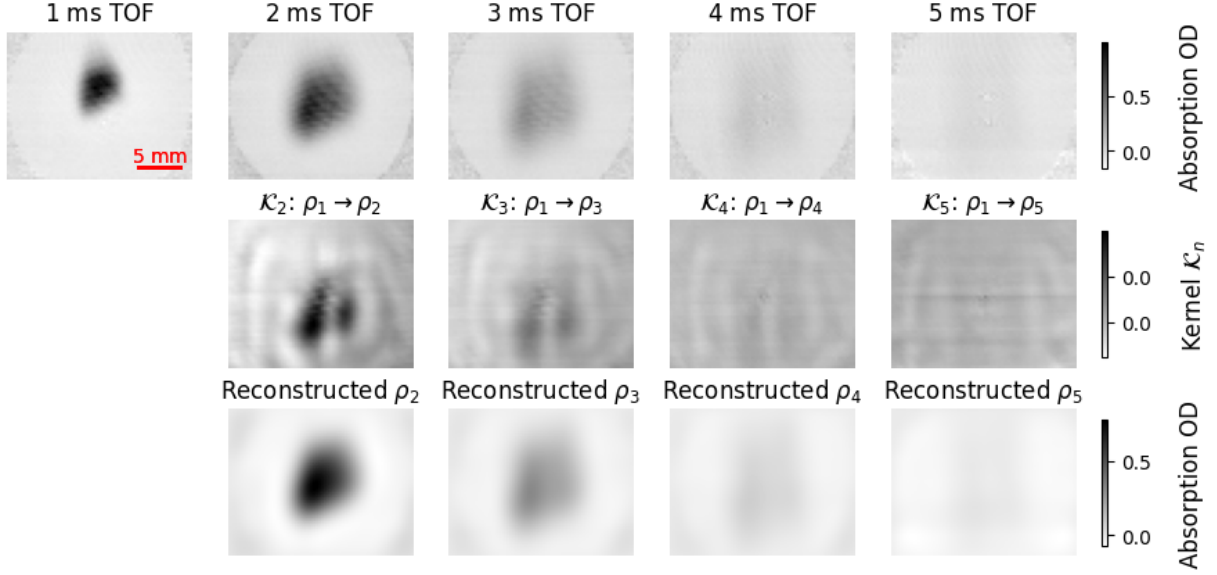


Figure 5.6: Evolution kernel for the clouds defined by the files 2024-02-03 group 1201. The first row is the input images of the cloud's expansion. The second row contains the kernels calculated using Eq. (5.25), and the third row is the reconstructed image calculated by convolving the initial distribution with the respective kernel.

Now, the solutions for the transformed velocity kernels are

$$\mathcal{K}_n = \mathcal{F}^{-1} \left\{ \frac{\mathcal{F}\{\rho_1\} * \mathcal{F}\{\rho_n\} S_n}{\|\mathcal{F}\{\rho_1\}\|^2 S_n + 1} \right\}, \quad n = 2, \dots, N. \quad (5.25)$$

Note that, in this method, we don't have access to the initial $t = 0$ distribution. Thus, we have to assume that all distributions are written in terms of the expansion of the first distribution. This assumption is valid if the cloud hasn't expanded much from $t = 0$ to $t = \tau_1$. In the limit of $S_n \rightarrow 0$ the kernels converge to

$$\mathcal{K}_n \rightarrow S_n \rho_1 * \rho_n. \quad (5.26)$$

Despite this solution being very different from the naive solution in Eq. (5.20), Eq. (5.26) is intuitive because the kernels look smoother as time progresses (as they are a simple convolution between larger distributions). In the opposite limit $S_n \rightarrow \infty$, the kernels look noisy and

don't behave as expected for longer times. The trade-off is the interplay between a reasonable reconstruction of the input images and a smoother or noisy kernel.

Here, I applied this model to the two sets of images depicted in the previous subsection: see Figs. 5.5 and 5.6. The kernels in the second rows are calculated using Eq. (5.25) with $S = 10^{-2}$. For this value of SNR, we can see both the smoother part of the solution at the center and the noisy distributions at the boundaries of the velocity kernel. The first is related to the convolution of the target and the input image, whereas the latter comes from the denominator. For the present results, I don't have a reliable method to assign a temperature for a given kernel. This is due to the dependency on the SNR and how drastically the kernels vary as I change S .

5.2.3 Position dependent temperature distribution

The previous methods assumed that the velocity distribution is independent of the position distribution, and Eq. (5.7) can be written as a product of two Fourier transformations. However, this simplification might not be accurate for all experimental conditions. Here, we aim to describe a numerical method to calculate a first-order correction to this approximation.

We assume that the atoms haven't had much time to expand by the time of the first image. Consequently, the temperature distribution is related to the position distribution at the earliest time. To work with a complicated position-dependent temperature distribution, one needs to assume a particular model for the kernel $\mathcal{K}_n[x_0, y_0]$ in Eq. (5.4). For simplicity, I assume a local

Gaussian distribution with temperature that depends on position $T(x_0, y_0)$

$$\mathcal{F}\{\mathcal{K}_n[x_0, y_0]\} = e^{-\frac{1}{2m}k_B\tau_n^2 T(x_0, y_0)(k_x^2 + k_y^2)} \quad (5.27)$$

$$\mathcal{F}\{\rho_n\} = \mathcal{F}\left\{\rho_1 e^{-\frac{1}{2m}k_B\tau_n^2 T(x_0, y_0)(k_x^2 + k_y^2)}\right\}. \quad (5.28)$$

So far, the model is exact. However, I need to make assumptions to solve for the position-dependent temperature. Let's consider that the velocity distribution is close to the Maxwell-Boltzmann distribution with a single temperature. That means we can write the temperature distribution as an average temperature and a small correction that has a spatial distribution

$$T(x, y) = T_0 + \delta T(x, y). \quad (5.29)$$

Here, T_0 is the 0'th-order temperature, calculated using the fitting method described in Sec. 5.2.1.

I expand Eq. (5.28) using (5.29) up to k 'th-order and solve for the correction using a linear regression approach to minimize the error when considering all the TOF images.

Let's consider the first-order correction. For a given TOF expansion, we can write

$$\mathcal{F}\{\rho_n\} \approx \mathcal{F}\{\rho_1\} e^{-\frac{1}{2m}k_B\tau_n^2 T_0 k_r^2} - \left(\frac{1}{2m}k_B\tau_n^2 k_r^2\right) \mathcal{F}\{\rho_1 \delta T_1\} \mathcal{P}_n e^{-\frac{1}{2m}k_B\tau_n^2 T_0 k_r^2}, \quad (5.30)$$

where $k_r^2 = k_x^2 + k_y^2$ and \mathcal{P}_n is a projection function that satisfies

$$\mathcal{P}_n = \begin{cases} 1, & \frac{1}{2m}k_B\tau_n^2 k_r^2 \leq 1 \\ 0, & \frac{1}{2m}k_B\tau_n^2 k_r^2 > 1 \end{cases}. \quad (5.31)$$

To solve for the first-order correction, one needs to write the error function when considering all TOF images:

$$\epsilon = \sum_n \left| \mathcal{F}\{\rho_n\} - \mathcal{F}\{\rho_1\} e^{-\frac{1}{2m} k_B \tau_n^2 T_0 k_r^2} + \left(\frac{1}{2m} k_B \tau_n^2 k_r^2 \right) \mathcal{F}\{\rho_1 \delta T_1\} \mathcal{P}_n e^{-\frac{1}{2m} k_B \tau_n^2 T_0 k_r^2} \right|^2. \quad (5.32)$$

The solution is obtained by considering $d\epsilon/d\delta T_1 = 0$:

$$\mathcal{F}\{\rho_1 \delta T_1\} = \frac{-\sum_n \tau_n^2 e^{-\frac{1}{2m} k_B \tau_n^2 T_0 k_r^2} \left[\mathcal{F}\{\rho_n\} - \mathcal{F}\{\rho_1\} e^{-\frac{1}{2m} k_B \tau_n^2 T_0 k_r^2} \right] \mathcal{P}_n}{\sum_n \tau_n^2 \left[e^{-\frac{1}{2m} k_B \tau_n^2 T_0 k_r^2} \right]^2 \left(\frac{1}{2m} k_B \tau_n^2 k_r^2 \right) \mathcal{P}_n}. \quad (5.33)$$

Note that Eq. (5.33) has a few implementation issues. The first is that the denominator is ill-defined for $k_r = 0$. Thus, one needs to ignore this point or set it to zero. However, as we will take a Fourier inverse of Eq. (5.33), the zero frequency component adds a constant value to the distribution. Ultimately, we will set $\text{mean}(\delta T_1) = 0$, making this problem manageable. The second issue is the zeros in the denominator introduced by the projection operator in Eq. (5.31). To circumvent this problem, instead of using \mathcal{P}_k we will use 1 when k corresponds to the smallest $\tau_k = \min\{\tau_n\}$.

The final ingredient is to enforce that $\text{mean}(\delta T_1) = 0$, and we can do that by calculating δT_1 in Eq. (5.33) and then subtracting its mean. This will cause $\text{mean}(\delta T_1) = 0$ but not $\text{mean}(\rho_1 \delta T_1)$ and this is exactly the quantity we seek as a first-order correction for the temperature calculated using the fitting method.

Numerically, I noticed that the values of $\rho_1 \delta T_1$ are small and somewhat well-behaved. However, because the temperature itself has a dependency $\delta T_1 \sim (1/\rho_1)$ from Eq. (5.33), the range of values of the temperature distribution are very large and break the assumption that $\delta T_1 \ll$

T_0 .

To obtain a better approximation for the temperature distribution, one can seek a second-order solution that approximates the evolution in Eq. (5.28) as:

$$\begin{aligned} \mathcal{F}\{\rho_n\} \approx & \mathcal{F}\{\rho_1\} e^{-\frac{1}{2m} k_B \tau_n^2 T_0 k_r^2} - \left(\frac{1}{2m} k_B \tau_n^2 k_r^2 \right) \mathcal{F}\{\rho_1 \delta T_1\} \mathcal{P}_n e^{-\frac{1}{2m} k_B \tau_n^2 T_0 k_r^2} \\ & - \left(\frac{1}{2m} k_B \tau_n^2 k_r^2 \right) \mathcal{F}\{\rho_1 \delta T_2\} \mathcal{P}_n e^{-\frac{1}{2m} k_B \tau_n^2 T_0 k_r^2} \\ & + \frac{1}{2} \left(\frac{1}{2m} k_B \tau_n^2 k_r^2 \right)^2 \mathcal{F}\{\rho_1 \delta T_1^2\} \mathcal{P}_n e^{-\frac{1}{2m} k_B \tau_n^2 T_0 k_r^2}. \end{aligned} \quad (5.34)$$

If one uses the solution in Eq. (5.33) as a input parameter and solves for δT_2 , the solution is:

$$\mathcal{F}\{\rho_1 \delta T_2\} = \frac{\frac{1}{2} \sum_n \tau_n^4 \left(\frac{1}{2m} k_B \tau_n^2 k_r^2 \right) \left[e^{-\frac{1}{2m} k_B \tau_n^2 T_0 k_r^2} \right]^2 \mathcal{P}_n}{\sum_n \tau_n^4 \left[e^{-\frac{1}{2m} k_B \tau_n^2 T_0 k_r^2} \right]^2 \mathcal{P}_n} \mathcal{F}\{\rho_1 \delta T_1^2\}. \quad (5.35)$$

However, this solution has even larger values for δT_2 , which breaks the assumption that $\delta T_1 + \delta T_2 \ll T_0$.

5.2.4 Discussions and conclusions

The problem of determining the temperature in a cold cloud of atoms is not new, and various methods have been developed in the past decades [196, 209]. In this part of the chapter, I focused on developing and presenting new methods to calculate the velocity distribution and temperature of a cloud of atoms.

All methods are based on the ballistic convolution expansion of the atoms in Eq. (5.1). This model assumes that the atoms have intrinsic velocities and expand ballistically without interaction. As a consequence, if the velocity is described by an uncorrelated thermal distribution,

the evolution of the position distribution can be solved exactly starting from a Gauss-Hermite expansion. This result shows that for later times, the cloud of atoms looks more like a Gaussian distribution, and all signatures of non-Gaussianity vanish. This analytical result can be used to calculate the temperature and the $\tau = 0$ distribution using a constrained Gauss-Hermite fitting.

Later, I study generalizations of these two assumptions: thermal distribution and uncorrelated velocities. In the case of uncorrelated but general velocity distribution, one can derive the kernels that evolve the initial distribution into all other distributions. This method uses an image deconvolution approach and assumes that the initial image isn't much different from the $t = 0$ distribution, which cannot be recovered. The method has one degree of freedom: the SNR of the deconvolution. This parameter controls the quality of the image reconstruction and the amount of noise in the evolution kernel. An in-depth study of the effects of the SNR on the mapping between the kernel and the cloud's temperature is left for future work.

The third method can be used to probe the correlations between the velocity and position distributions. I assume a Maxwell's distribution with a local temperature that depends on position. The method is perturbative, with the 0'th order temperature given by the average temperature that better fits the evolution. The correlations are calculated in the first- and second-order corrections, which depend on position and are assumed to be small. However, the structure of the solutions depends on the inverse of the position distribution, which causes small values to contribute largely and break the assumption of small corrections. A careful study to include noise in the analysis is left for future work.

5.3 Machine learning prediction pipeline

In the remainder of the chapter, I apply the first method developed in Sec. 5.2 to determine the temperature of the atomic clouds. The goal is to use ML to determine the cloud’s temperature and atom number using non-destructive measurements rather than TOF images. Here, I focus on data labeling and ML training with a simplified discussion about the physical implementation. For a detailed discussion about the experiment and the sequence, see the manuscript in preparation [4].

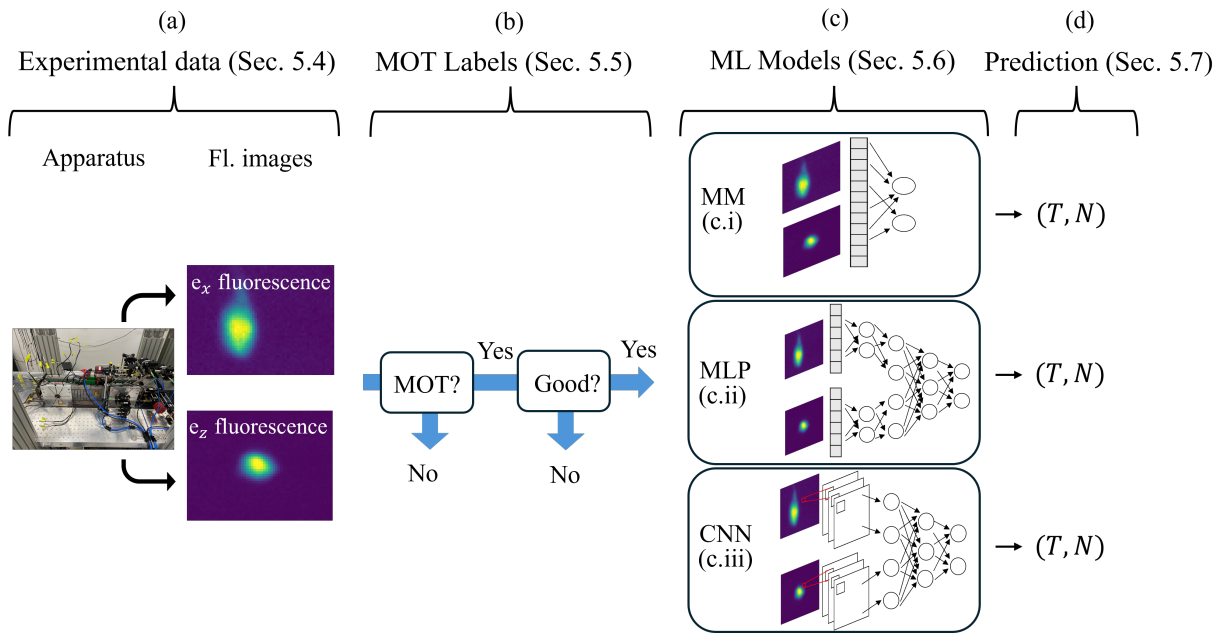


Figure 5.7: Workflow of the work. Data is generated (Sec. 5.4) in the experiment. Labels are calculated, and the images are preprocessed (Sec. 5.5). The models (Sec. 5.6) are trained, and the predictions are compared to the true values (Sec. 5.7).

Our pipeline works by setting the parameters of the experiment and then generating a run that potentially creates an atomic cloud; this process is called a “shot”—this is the first step in Fig. 5.7(a). To calculate the temperature using the method described in Sec. 5.2.1, the shots are collected into “groups” of $M = 5$ shots that differ only by the TOF time.

Table 5.1: Dataset labels. This table contains the labels derived from our classification and fitting processes.

Symbol	Label	Range in dataset	Description
T	TEMP	0.5 mK to 30 mK	Temperature
N	NUM	8×10^6 to 2×10^8	Number of atoms
-	MOT	[true, false]	Indicates whether there is any identifiable signal in fluorescence data.
-	GOOD_MOT	[true, false]	Data for which the process described below was able to assign TEMP, and NUM labels.

For each group, we classify the MOT configuration’s performance by assigning labels, as seen in Table 5.1. These labels are hierarchical, as shown in Fig. 5.7(b), where we first define if the images contain atoms (MOT label). The second category asks whether the MOT performance is good or bad (GOOD_MOT label). The metric used to decide if we have atoms or not is the total fluorescence intensity. The metric used to decide if we have good MOT performance is to check if the physical parameters of temperature (T) and atom number (N) could be determined and are reasonable.

Once we label the dataset, we identify our input data by selecting the fluorescence images. These images are pre-processed into “sets” to study different transformations in the data and test the robustness of the ML models. Using these sets, we train various regression models—ranging in complexity from a simple single-layer linear model (i.e., matrix multiplication, MM) to a multi-layer perceptron (MLP) and a convolution neural network (CNN)—with all of them being able to recover T and N . Figure 5.7 depicts the pipeline used from data generation to labeling and (T, N) prediction.

Once trained, the best regression models can predict (T, N) with an average fractional error ($\mathcal{E}_\%$) of $\approx 3\%$. To put it in perspective, if one assigns the average values for T [$\approx (6 \pm 4) \text{ mK}$]

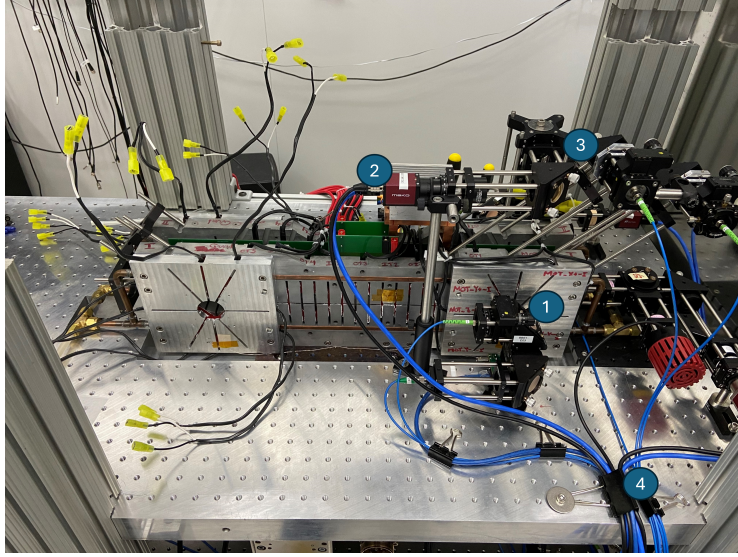


Figure 5.8: Experimental apparatus for MOT preparation and image taking at Minilab (NIST Gaithersburg). 1) shows the science cell where the atomic cloud is prepared, 2) shows one of the cameras used for imaging, 3) shows part of the mirrors and lenses used to focus the laser beams on the MOT cell, and 4) shows the optical fibers that conduct the laser into the experiment.

and $N [\approx (5 \pm 3) \times 10^7]$ for all clouds in our dataset, the average fractional error would be $\mathcal{E}_{\%} \approx 90 \%$. The time necessary to calculate the predictions is typically 0.3 ms to 1 ms.

5.4 Experiment

The experiment prepares and stabilizes an atomic cloud of potassium ^{39}K atoms. We employ a standard vapor-loaded MOT to slow down and trap atoms [206–208]. In our experiment, cooling and trapping rely on radiation pressure from three pairs of counterpropagating laser beams, along with a quadrupole magnetic field. The lasers are red-detuned from the $F = 2 \rightarrow F' = 3$ transition of the atoms. In order to maintain the potassium-39 atoms in the correct hyperfine subspace, we employ a repump laser tuned near the transition $F = 1 \rightarrow F' = 2$.

In our present configuration, as seen in Fig. 5.8, atoms are captured from the low-velocity tail (below $\approx 30 \text{ m/s}$) of dilute room temperature potassium-39 vapor in our vacuum system.

Table 5.2: Experimental parameters varied to create diverse MOT conditions.

Parameter	Range	Description
Cooling AOM Volts	0.1 V to 1.5 V	Voltage of the cooling laser beam's AOM (Acousto-Optical Modulator). Controls the intensity of the cooling laser beam
Repump AOM Volts	0.4 V to 1.5 V	Voltage of the repump laser beam's AOM. Controls the intensity of the repump laser beam.
Cooling Lock Offset	85 MHz to 95 MHz	Controls the frequency offset of the cooling with respect to the repump laser.
Repump AOM Frequency	74 MHz to 94 MHz	Controls the frequency offset of the repump laser beam compared to the repump laser source
MOT Quadrupole Ampere	2 A to 405 A	Current of the MOT quadrupole coils. Affects the strength of the magnetic field.
MOT Loading Time	100 ms to 1800 ms	Duration of the MOT loading time.
TOF Time	1 ms to 5 ms	Group variable: time of flight. Symbol τ

The Doppler cooling achieved by the lasers' radiation pressure can cool the ^{39}K atoms to a typical temperature of $\approx 2 \text{ mK}$. The quadrupole magnetic field configuration can create a stable region of about 5 mm where, usually, around 10^7 atoms are captured. The relevant experimental parameters that are varied to create diverse MOT conditions are the lasers' intensity, the lasers' frequency, the current generating the quadrupole magnetic field, and the duration of the loading phase, as seen in Table 5.2. The lasers' properties are controlled by an acousto-optical modulator (AOM) that provides high bandwidth control of the power and introduces tunable frequency

Table 5.3: Imaging parameters. This table describes the relevant information of our three imaging systems.

Camera name	Resolution	Magnification	Magnified pixel size	Measurement type
e_x -camera	484×644	0.5	$14.8 \mu\text{m}$	fluorescence imaging
e_y -camera	1024×1280	0.333	$15.9 \mu\text{m}$	absorption imaging
e_z -camera	484×644	0.375	$19.7 \mu\text{m}$	fluorescence imaging

shifts.

The atomic clouds are imaged along the three Cartesian axes using independent arrangements of lenses. The data is collected using complementary metal oxide semiconductor (CMOS) cameras that we use to label the imaging axes (e_x , e_y , and e_z). The camera properties are detailed in Table 5.3. During data collection, the e_x - and e_z -cameras are used to collect fluorescence images, while the e_y camera is used for the TOF measurement.

The fluorescence images contain two frames: atoms and background frames. The TOF image contains three frames: atoms, probe, and background frames. The TOF measurement is also called absorption measurement because it images the shadow cast by the atoms on the probe light. The ratio between the probe and atom intensity is used to calculate the optical depth (OD)—a measure of the column atomic density, as described in Appendix 5A.

The fluorescence images capture the scattered light and are taken after the loading, cooling, and trapping stages. The absorption image is the last step of the experiment because the trap is shut down, and the atoms are set free to expand. After a pre-determined expansion time, τ , the atomic absorption is measured. The evolution information obtained from the TOF absorption image is then used to calculate the temperature and atom number, as ground truth labels for the ML models.

5.5 Data collection

We collected data for various experimental conditions to explore the different possibilities for forming an atomic cloud. We use a series of absorption images taken with the same experimental parameters and with increasing TOF τ_n , with $n = 1, \dots, M$, to assign (T, N) label for a given experiment realization. To have a diverse and representative set of images (see Fig. 5.2), we repeated the experiment several times and changed six experimental parameters that control various aspects of the MOT configuration, see Table 5.2. We employed a semi-random strategy to explore the parameter space using a random step around the regions where good atomic clouds are formed. The current dataset consists of 6783 groups, totaling 33915 individual shots.

5.5.1 Labeling strategy

For each shot, we assign the four labels shown in Table 5.1. Here, I describe the strategy for generating these labels in the order they are assigned in our labeling process.

MOT: This label identifies data in which the overall fluorescence counts subtracted from the background noise lie above a certain threshold. This label is either `True` or `False`. Because our data is organized into groups, this label is only assigned `True` if all images surpass the set thresholds.

These thresholds aim to separate the data that don't contain atoms (in which the photon-shot noise governs the total count statistics) from the data that contain detectable fluorescence counts from atoms; as depicted in Fig. 5.9

Atom number. To calculate the number of atoms, we integrate the pixel intensity in the region where the probe laser has light and divide it by the scattering cross-section [230, 231].

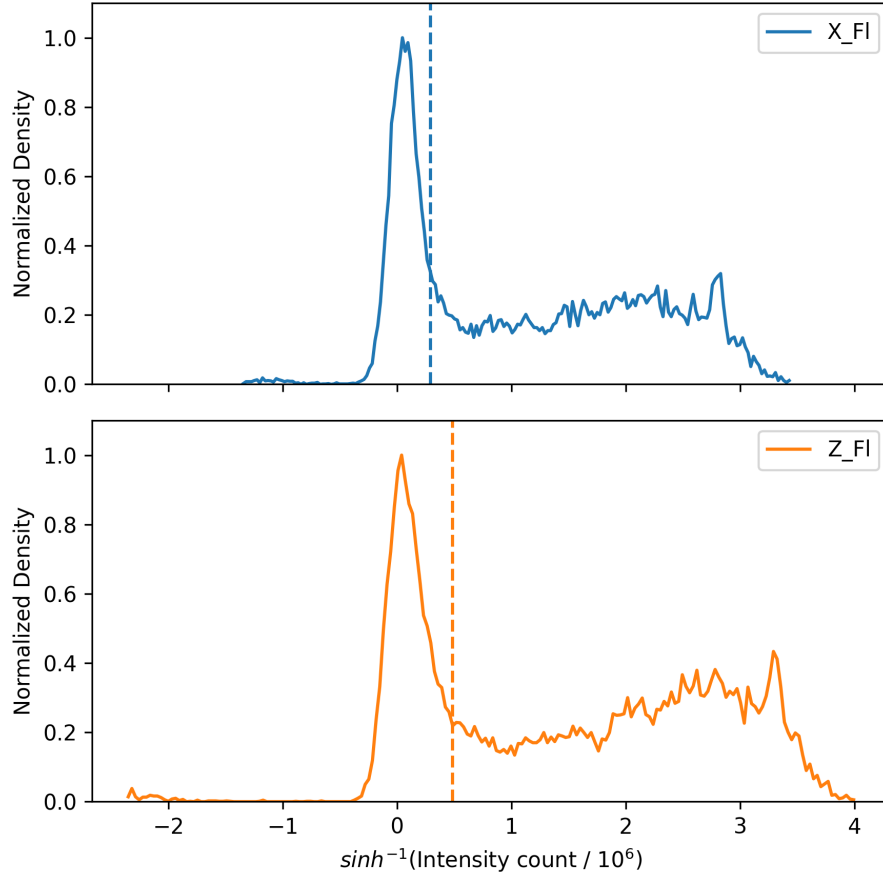


Figure 5.9: Distribution of total fluorescence counts for e_x - (top) and e_z - (bottom) images. The dashed line represents the threshold used in each axis to determine if a group is assigned MOT = True.

Then, we average it over all five images in the set

$$N = \frac{1}{M} \frac{A \sum_{n=1}^M \sum(\rho_{TOF,n})}{\sigma}, \quad (5.36)$$

where $\rho_{TOF,n}$ represents the n 'th column density image ($n = 1, \dots, M$) [see Appendix 5A for details on how to calculate these distributions], $\sigma = 3\lambda^2/2\pi$ is the scattering cross-section, with wavelength of the transition being $\lambda = 766.7$ nm, and A is the effective area of the pixel.

Temperature. For the purpose of calculating the temperature labels to be used in ML

training, we use the convolution method described in Sec. 5.2.1. The group of column density images $\{\rho_{TOF,n}\}$ is fitted using Eqs. (5.17,5.18) using a max degree of Hermite polynomials equal to zero, i.e., using a simple convolved Gaussian fit. One can access the T_x and T_z anisotropic temperatures but not T_y (because the TOF image is taken along the e_y axis). Thus, the temperature label is the average $T = (T_x + T_z)/2$ temperature determined by the fitting.

GOOD_MOT: This label is determined by the quality of the fits used to obtain (T, N) . If a group is assigned MOT label True, then the second binary classification is based on whether the results of the fits yield physical and sensible results. If the fractional error of the fits is larger than 20 %, or the integrated N has a negative value, then all shots in the group are assigned GOOD_MOT label False. Only data with GOOD_MOT label True is used for the regression.

5.5.2 Data preprocessing

Three distinct preprocessing techniques are used to prepare the e_x - and e_z -fluorescence images of all 11500 good MOTs for ML training. The preprocessing functions range from a simple compression, which helps simplify the model and speed up the training, to introducing image flips and translation. The more complex preprocessing functions are essential to quantify the accuracy and robustness of the different NN architectures. Each preprocessing function generates a set to which all architectures are trained and tested.

The sets are:

- *Compressed Set \mathcal{S}_c* : Each original e_x - and e_z -image is compressed to 48×64 pixels [total of 11500 data points].
- *Flip Set \mathcal{S}_f* : Each original e_x - and e_z -image is compressed to 48×64 pixels. Data augmen-

tation generates 770 images from horizontal and vertical flips of the original image [total of 17250 (11500 + 5750) data points].

- *Translation Set \mathcal{S}_t* : Each e_x and e_z -image is compressed to 48×64 pixels, randomly flipped, and translated in a wider frame of 72×96 with zero padding [total of 34500 data points].

The flip and translation sets contain more data because of augmentation. As we introduced more variability to the training, we also need to generate more data so the models can learn from it.

5.6 Machine Learning models

This section focuses on the various models we use to solve the task of predicting the temperature and the number of atoms based on the fluorescence images. Although this work focuses on presenting results for ML models, it is instructive to discuss a linear regression model to build intuition in the prediction task and to have a baseline comparison as we increase the framework's complexity.

Linear regression. The simplest predictor one can build to estimate T and N using the fluorescence images is based on linear regression. We employ linear fitting with six parameters (four angular coefficients and two linear coefficients) to correlate the target parameters (T, N)

with the integrated e_x - and e_z -fluorescence counts (I_x, I_z) (fluorescence total intensity):

$$\begin{pmatrix} T \\ N \end{pmatrix} = \mathbf{L} \begin{pmatrix} I_x \\ I_z \end{pmatrix} + \tilde{\mathbf{b}}. \quad (5.37)$$

Now, we consider three distinct ML architectures for the more sophisticated and robust models, as seen in Fig. 5.7(c).

Matrix multiplication. The simplest model one can consider is a linear transformation. The linearity of the transformation allows us to employ the *early fusion* approach [232] by combining the e_x and e_z -images to form a single image. The resulting image is reshaped into a one-dimensional (1D) input vector. We implement MM with a single fully connected layer and linear activation where the input neurons directly connect to the output, as seen in Fig. 5.7(c.i). The output is two neurons representing the predicted atom number and the temperature.

Effectively, this model is equivalent to multiplying a matrix by the one-dimensional reshape of the images. This model generalizes the linear regression model by considering each pixel of the two images as an independent dimension for linear regression rather than summing the intensities of all pixels.

Multi-Layer Perceptron. For the MLP, we employ the *late fusion* approach [232], which involves treating each input image as a separate entity before concatenating it into a single 1D vector. The MLP model takes as input two 1D vectors representing the reshaped images and independently propagates them through a sequence of fully connected layers using Leaky ReLU for the activation function of the hidden neurons, see MLP in Fig. 5.7(c.ii). After a series of

independent layers, the two outputs are concatenated and passed through a subsequent series of fully connected layers. The final output layer retrieves the pair (T, N) .

Image convolution CNN. The CNN architecture is the most suitable for image analysis as it can learn spatial patterns in the images by convolving the so-called *kernel* (a small matrix) with the image. The convolution introduces a translation invariance that enables learning the critical two-dimensional (2D) features of the images. While CNNs are typically used for image classification, in this work, we combine the pattern recognition power of the CNNs with a fully connected layer to help learn nontrivial correlations between the features extracted from the spatial kernels.

Similar to the MLP model, our CNN also employs the late fusion approach, with the parallel fully connected layers being replaced by two parallel series of convolutional layers. The images undergo convolution, pooling, and activation layers before being flattened and concatenated. The concatenated data then passes through dense and activation layers for regression, see CNN in Fig. 5.7(c.iii).

5.6.1 Optimization and training

For the present results, I used fixed architectures for each model. The particular choices of the number of layers and amount of neurons/kernels in each layer were made using intuition from preliminary tests. This is a sub-optimal solution because it is beneficial to use a hyperparameter optimization to choose the specific details of the architecture. However, to show a proof-of-concept result, the current choice of parameters suffices. For a better choice of architectures, see [4]. Detailed information regarding the architectures for all three models can be found in

Appendix 5B.

During training, all models utilized the Adam optimizer [233]. The training concluded when the validation accuracy or loss showed no improvement for 500 consecutive epochs or after a total of 2000 epochs. The typical training loop takes about 10^3 epochs and finishes in 10^1 minutes to 10^2 minutes with a single GPU. The typical evaluation time for all models ranges from 0.3 ms to 1 ms.

Due to camera digitization, the input images are normalized by 4096 on a pixel level prior to training. The labels are normalized using a min-max function of the log of the target parameters (T, N) . This is done because the range of target values can vary by orders of magnitude.

5.7 Prediction results

For all trained models, two performance metrics are reported: the coefficient of determination (R^2) and the average fractional error [$\mathcal{E}_\% = (\mathcal{E}_{T\%}, \mathcal{E}_{N\%})$]. The R^2 score quantifies the proportion of variance in the data that is explained by the predictors, providing a measure of overall model fit. Meanwhile, the average fractional error captures the relative deviation of predictions from true values, offering a complementary perspective on predictive accuracy that is particularly useful when errors span multiple orders of magnitude. These metrics are computed using ten randomly selected folds for cross-validation. The final reported scores are averaged over all folds, with uncertainties estimated from the standard deviation.

As a baseline performance comparison, the simplest predictor (that always predicts the average value for T and N) has $R^2 = -0.0008 \pm 0.0006$ and $\mathcal{E}_\% = (94 \%, 88 \%) \pm (3 \%, 3 \%)$.

Linear regression. The average linear regression fitting scores are $R^2 = 0.13 \pm 0.03$ and

Table 5.4: Summary table for the results of different architectures tested in different datasets. For brevity, we denote $\mathcal{E}_{T\%}$ as the average fractional error (in percentage) for temperature and $\mathcal{E}_{N\%}$ as the average fractional error (in percentage) for atom number. The numbers in parentheses show the most significant digit of the standard deviation.

	MM				MLP				CNN			
	Parameters	R^2	$\mathcal{E}_{T\%}$	$\mathcal{E}_{N\%}$	Parameters	R^2	$\mathcal{E}_{T\%}$	$\mathcal{E}_{N\%}$	Parameters	R^2	$\mathcal{E}_{T\%}$	$\mathcal{E}_{N\%}$
Set \mathcal{S}_c	12290	0.742(2)	23.5(2)	36.8(4)	7839970	0.991(7)	1.9(1)	3.5(2)	835394	0.991(1)	3.2(3)	3.1(2)
Set \mathcal{S}_f	12290	0.68(1)	27(1)	40(1)	7839970	0.966(7)	3.9(6)	8.0(5)	835394	0.977(6)	4.5(6)	5.2(5)
Set \mathcal{S}_t	27650	0.29(3)	56.0(6)	52.4(6)	15704290	0.733(4)	21.5(4)	42(1)	1228610	0.941(5)	6.9(4)	13.8(6)

$\mathcal{E}_{\%} = (65 \%, 57 \%) \pm (2 \%, 2 \%)$. The positive R^2 indicates that this model can explain slightly better the correlation between the total pixel intensity and the target (T, N). This result represents an improvement from the average predictor and a higher baseline for more complex models.

Matrix Multiplication. The MM is more complex and generalizes the integrated fluorescence linear regression. Each pixel is treated as an independent degree of freedom, rather than summing all pixels. Table 5.4 shows that it can predict the target properties with an accuracy of 23 %, at best. Interestingly, the atom number has worse performance than temperature.

As one increases the complexity of the input data (here, tested by the flip and translation augmentation), the MM model has difficulty keeping up with more general data. The decrease in accuracy is notable, but the results still lay above the warm-up models, as expected, since the number of parameters is much larger.

Multi-Layer Perceptron. The MLP model contains nonlinear activations and is the largest model in the number of parameters. Thus, it is expected to perform better than a linear model. But, surprisingly, it performed better than the CNNs for temperature in sets \mathcal{S}_c and \mathcal{S}_f . This performance can be seen in Table 5.4, with the best accuracy obtained in the order of 2 %. In particular, it is interesting to note that no substantial change in performance occurred when horizontal/vertical flips were introduced in the data. The MLP model seems to be robust to this

type of generalization.

However, for set \mathcal{S}_t , which contains flips and translation, the model has a drastic change in performance. This drop in accuracy can be explained by the fact that MLPs are not designed to treat spatially invariant data.

Convolution Neural Network. Convolution models were designed for image analysis because they can extract information that can be scattered across the image. The results reported in Table 5.4 show the performance of CNN remains robust for the first two datasets (\mathcal{S}_c and \mathcal{S}_f). For set \mathcal{S}_t , temperature accuracy remains robust but the accuracy on atom number prediction drops significantly.

The results show that the CNN model is the most suitable for temperature and atom number prediction of all tested architectures. Although it has fewer parameters than the MLP model, it is the most complex model and takes longer to train. The increase in training complexity compensates for a gain in performance.

5.8 Discussions

All three methods successfully predict the labels using fluorescence images. And for all sets, the prediction scores lie above the average predictor and the linear regression—as expected, because these warm-up models are linear and only contain a small number of parameters. Surprisingly, temperature is one of the parameters that can be accurately estimated using nondestructive images. Without access to expansion information, the NN models can calculate the cloud's temperature using a snapshot of the MOT while still trapped.

For the translation set \mathcal{S}_t , we saw a substantial increase in error prediction, even for CNNs

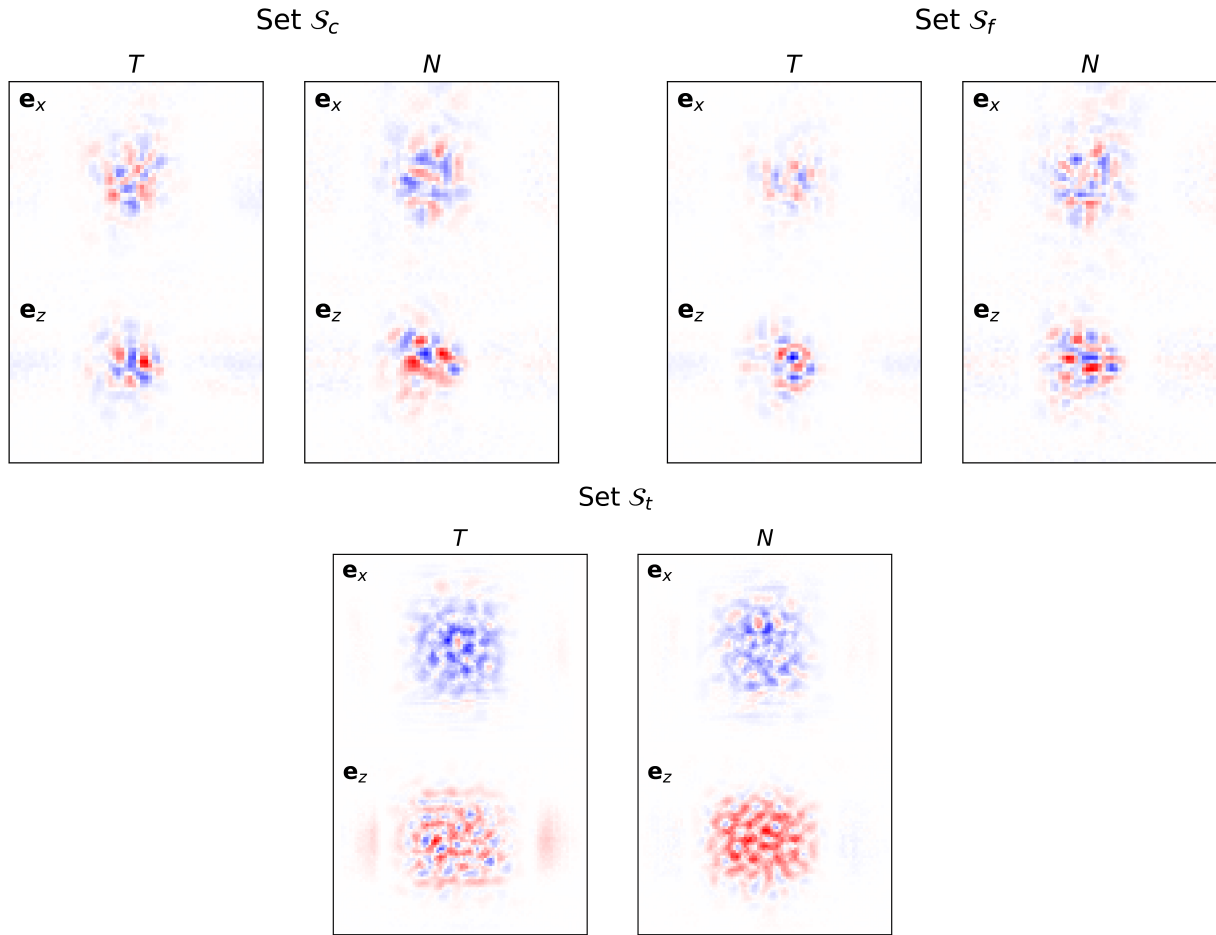


Figure 5.10: Matrix representation of the weights learned by the MM model multiplied by the average fluorescence image on each set $\{\mathcal{S}_c, \mathcal{S}_f, \mathcal{S}_t\}$. For each set, on top, we have the weights times the \mathbf{e}_x -fluorescence image, and on bottom, the weights times the \mathbf{e}_z -fluorescence image. For each set, the plot on the left shows the evaluation capable of estimating temperature, and the plot on the right shows the evaluation that can estimate the number of atoms. Blue pixels correspond to positive values, red pixels to negative values, and white to zero.

(that are designed to work with translated data). This can happen due to many factors, including the sub-optimal design of the architectures and possibly the low number of augmented data points included in the original data set. More training is needed to test these claims and check for improvement in training performance.

Although I cannot offer a physical explanation or intuition for the fact that NNs can predict (T, N) from fluorescence images, one can look at the learned parameters of these models to

gain some insights. For the MM, the training can be explained as obtaining an optimal kernel to perform an integration over the pixel images, as seen in Fig. 5.10. The trained model has a spatial pixel distribution over the central region, where clouds are typically formed. The blue and red colors show the model is summing and subtracting different regions in the image, indicating the atomic ensemble doesn't contribute uniformly to the parameter estimation. Surprisingly, the matrix capable of estimating the number of atoms differs significantly from a simple integration of the pixels (as one would expect from the relationship between fluorescence and atom number [223]). This suggests that different parts of the cloud contribute differently to these estimations. A further investigation into the physical mechanisms that allow temperature information to be extracted from fluorescence images is left for future work.

5.9 Conclusions

In this chapter, we studied three distinct NN models to estimate the physical parameters of an ensemble of cold atoms using solely nondestructive measurements. We implemented a fluorescence imaging system to collect the scattered light of the MOT system and use that information to predict the temperature and the number of atoms in the atomic cloud.

The satisfactory accuracy of the MM and the MLP for sets \mathcal{S}_c and \mathcal{S}_f shows that simpler models can be used if it is known that the input data is “simple” enough. As for more complex data, here represented by the set \mathcal{S}_t , a more sophisticated model, like a CNN, is necessary to capture all the important features of the input data.

In general, ML models like the ones we present here can be used along with physical experiments to estimate parameters and use that information to guide the evolution of the experiment

without the need to employ destructive or invasive measurements. One immediate application of the models of this work is to take fluorescence pictures of the cloud to estimate temperature and check if the cooling techniques are being implemented efficiently during the evolution. After being trained and validated, an ML model can apply real-time feedback in the experiment.

We hope this work can motivate the use of modern machine-learning models and tools to speed up and increase the accuracy of cold atom experiments. The study of quantum phenomena in cold atom systems can also benefit from ML models that learn complex patterns from output signals and images. Further questions to be answered include an in-depth investigation of how temperature information is encoded in the fluorescence images and which other physical parameters can be estimated based on non-destructive measurements.

5A Column density calculation

The absorption image frames are as follows: the atoms frame, the probe frame, and the background frame. The atoms frame is taken immediately after the TOF expansion, and it activates a probe beam on resonance with the atoms when being captured, as well as an imaging repump beam. The probe frame is taken next, and it consists of the same probe and imaging repump beams but is taken when no atoms remain. As such, the atoms frame appears darker than the probe in places where the expanding atoms were present. Finally, a background frame is taken with the probe turned off, but the imaging repump beam remains.

These three frames are used to calculate the OD image for the expanded MOT. The OD image for TOF absorption is defined by [230, 231]

$$\rho_{TOF} = -\log\left(\frac{\text{atom} - \text{background}}{\text{probe} - \text{background}}\right) - \frac{(\text{atom} - \text{probe})}{I_{sat}}, \quad (5.A1)$$

where $I_{sat} = 200$ counts is used to correct for OD saturation. Here, $I_{sat} \simeq (E/\tau_e)/A$, with E corresponding to photon energy, τ_e is the camera exposition time, and A is the pixel area. The saturation intensity is used in units of counts rather than physical units, representing the conversion of photons to digital camera counts.

5B Neural Network architectures

This section presents the exact architectures used for each architecture in each dataset. The values in the cells of the tables represent the dimension of the layer: the number of neurons for a fully connected layer or the number of kernels for a convolution layer.

5B.1 Matrix Multiplication MM

Layer type	Set \mathcal{S}_c	Set \mathcal{S}_f	Set \mathcal{S}_t
Input layer	$2 \times (48 \times 64)$	$2 \times (48 \times 64)$	$2 \times (72 \times 96)$
Dense	2	2	2

5B.2 Multi-layer perception MLP

Here, the notation $2 \times \text{Layer}$ will denote that the input images are being processed in parallel and that the details of the layers are equal for each image. After the flattening step, the processed images are concatenated and passed through the regression's fully connected layers.

Layer type	Set \mathcal{S}_c	Set \mathcal{S}_f	Set \mathcal{S}_t
$2 \times$ Input layer	(48×64)	(48×64)	(72×96)
$2 \times$ Dense + LeakyReLU	1024	1024	1024
$2 \times$ Dense + LeakyReLU	512	512	512
$2 \times$ Dense + LeakyReLU	256	256	256
Flattening + Concat	512	512	512
Dense + LeakyReLU	256	256	256
Dense + LeakyReLU	256	256	256
Dense + LeakyReLU	128	128	128
Dense	2	2	2

5B.3 Convolutional Neural Network CNN

Similarly to the FNN model, $2 \times \text{Layer}$ denotes that the images are being processed in parallel. The number inside the parenthesis of the Conv2D layer indicates the size of the kernel.

Layer type	<i>Set \mathcal{S}_c</i>	<i>Set \mathcal{S}_f</i>	<i>Set \mathcal{S}_t</i>
2× Input layer	(48 × 64)	(48 × 64)	(72 × 96)
2× Conv2D(9) + LeakyReLU	8	8	8
2× BatchNorm + Dropout(0.2) + AvgPooling			
2× Conv2D(9) + LeakyReLU	16	16	16
2× BatchNorm + Dropout(0.2) + AvgPooling			
2× Conv2D(9) + LeakyReLU	32	32	32
2× BatchNorm + Dropout(0.2) + AvgPooling			
2× Conv2D(9) + LeakyReLU	32	32	32
2× BatchNorm + Dropout(0.2) + AvgPooling			
Flattening + Concat	768	768	1536
Dense + LeakyReLU	512	512	512
Dense + LeakyReLU	256	256	256
Dense + LeakyReLU	128	128	128
Dense + LeakyReLU	32	32	32
Dense	2	2	2

Chapter 6: Outlook and future directions

In this thesis, I studied quantum measurements and feedback in various forms. Chapter 2 discusses various formulations of weak measurements and the derivation of the baseline master equation: the QFPME [1]. In Chapter 3, I applied the QFPME to a particular toy model to show how to use this framework to derive non-trivial analytical results. Generalizations of the master equation are discussed in Chapter 4 where I showed how to extend the filtering operation of QFPME to more realistic situations. The cooling protocol was also studied using a bandpass filter. Finally, in Chapter 5, measurement is studied in a real system where I used fluorescence images from potassium atomic cloud to estimate the temperature and atom number using machine learning.

All topics discussed in this dissertation are related to quantum measurements. The increasing interest and applications of quantum measurements make it necessary to develop realistic models to describe experiments. The first chapters of the dissertation do this job by generalizing earlier results and deriving a family of master equations capable of modeling complex experimental frameworks. The ability to translate complicated filtering into the experimental description and still derive analytical results for the evolution of the ensemble of experiments is a significant mark. I hope the results presented in this thesis can be used by experimentalists and motivate the development of more sophisticated measurement processes.

As for future directions, it would be interesting to investigate extensions and applications of the generalized QFPME. Here, I investigated the generalization of the filtering process in Chapter 4, so the next step would be to study a family of master equations whose starting point is a different distribution of weak measurements — here, I used Gaussian measurements. By considering more general distributions, one can ask how the statistics of the measurement affects the ensemble of outcomes.

Master equations can also be applied to existing tasks to improve specific feedback protocols. By solving for the steady state, one can employ a strategy similar to the one described in Chapter 4, to construct phase diagrams that improve experimental results after introducing new parameters. An important field where continuous feedback can be studied is quantum algorithms. Instead of focusing on a measurement at the end of the computation, it would be interesting to investigate the possibility of applying existing algorithms with a continuous measurement. Error correction algorithms, in particular, can benefit from the possibility of correcting a mistake in real-time.

Another avenue to study feedback master equations is their connections with thermodynamics and fluctuation theorems [176]. The ensemble picture of quantum feedback models can make natural connections with calculating moment distribution functions and studying expectation values beyond the first and second moments.

Finally, the generic framework of these master equations and their connection to continuous measurement can be helpful in the study of many-body systems. Experiments like atomic clouds and nuclear magnetic resonance can benefit from a many-body treatment of the measured operator. By investigating systems where nonlocal operators are measured, e.g. total magnetization or fluorescence, one can probe collective behavior for interacting systems.

Bibliography

- [1] Björn Annby-Andersson, Faraj Bakhshinezhad, Debankur Bhattacharyya, Guilherme De Sousa, Christopher Jarzynski, Peter Samuelsson, and Patrick P. Potts. Quantum fokker-planck master equation for continuous feedback control. *Phys. Rev. Lett.*, 129:050401, Jul 2022.
- [2] Björn Annby-Andersson, Debankur Bhattacharyya, Pharnam Bakhshinezhad, Daniel Holst, Guilherme De Sousa, Christopher Jarzynski, Peter Samuelsson, and Patrick P. Potts. Maxwell’s demon across the quantum-to-classical transition. *Phys. Rev. Res.*, 6:043216, Nov 2024.
- [3] Guilherme De Sousa, Pharnam Bakhshinezhad, Björn Annby-Andersson, Peter Samuelsson, Patrick P. Potts, and Christopher Jarzynski. Continuous feedback protocols for cooling and trapping a quantum harmonic oscillator. *Phys. Rev. E*, 111:014152, Jan 2025.
- [4] Guilherme De Sousa, Dario D’Amato, Brady Egleston, Michael Doris, Justyna Zwolak, and Ian Spielman. Predicting temperature of an atomic cloud using machine learning. Manuscript in preparation.
- [5] Guilherme De Sousa and Christopher Jarzynski. Quantum fokker-planck master equation with general filter. Manuscript in preparation.
- [6] Daniel Schug, Sai Yerramreddy, Brady Egleston, Guilherme De Sousa, Rich Caruana, I. B. Spielman, Craig Greenberg, and Justyna P. Zwolak. Explainable machine learning for ultracold atoms image data. Manuscript in preparation.
- [7] Max Planck. *The Theory of Heat Radiation*. P. Blakiston’s Son & Co., Philadelphia, 1914.
- [8] A. Einstein. Zur elektrodynamik bewegter körper. *Annalen der Physik*, 322(10):891–921, 1905.
- [9] N. Bohr. I. on the constitution of atoms and molecules. *The London, Edinburgh, and Dublin Philosophical Magazine and Journal of Science*, 26(151):1–25, 1913.
- [10] E. Schrödinger. An undulatory theory of the mechanics of atoms and molecules. *Phys. Rev.*, 28:1049–1070, Dec 1926.
- [11] Max Born. Zur quantenmechanik der stoßvorgänge. *Zeitschrift für Physik*, 37(12):863–867, Dec 1926.

- [12] W. Heisenberg. Über den anschaulichen inhalt der quantentheoretischen kinematik und mechanik. *Zeitschrift für Physik*, 43(3):172–198, Mar 1927.
- [13] P. A. M. Dirac. The quantum theory of the electron. *Proceedings of the Royal Society of London. Series A, Containing Papers of a Mathematical and Physical Character*, 117(778):610–624, 1928.
- [14] V. Fock. Konfigurationsraum und zweite quantelung. *Zeitschrift für Physik*, 75(9):622–647, Sep 1932.
- [15] Bose. Plancks gesetz und lichtquantenhypothese. *Zeitschrift für Physik*, 26(1):178–181, Dec 1924.
- [16] J. S. Bell. On the einstein podolsky rosen paradox. *Physics Physique Fizika*, 1:195–200, Nov 1964.
- [17] JOHN S. BELL. On the problem of hidden variables in quantum mechanics. *Rev. Mod. Phys.*, 38:447–452, Jul 1966.
- [18] John F. Clauser, Michael A. Horne, Abner Shimony, and Richard A. Holt. Proposed experiment to test local hidden-variable theories. *Phys. Rev. Lett.*, 23:880–884, Oct 1969.
- [19] William D. Phillips. Nobel lecture: Laser cooling and trapping of neutral atoms. *Rev. Mod. Phys.*, 70:721–741, Jul 1998.
- [20] Claude N. Cohen-Tannoudji. Nobel lecture: Manipulating atoms with photons. *Rev. Mod. Phys.*, 70:707–719, Jul 1998.
- [21] Gerard Mourou. Nobel lecture: Extreme light physics and application. *Rev. Mod. Phys.*, 91:030501, Jul 2019.
- [22] Donna Strickland. Nobel lecture: Generating high-intensity ultrashort optical pulses. *Rev. Mod. Phys.*, 91:030502, Jul 2019.
- [23] E. A. Cornell and C. E. Wieman. Nobel lecture: Bose-einstein condensation in a dilute gas, the first 70 years and some recent experiments. *Rev. Mod. Phys.*, 74:875–893, Aug 2002.
- [24] Wolfgang Ketterle. Nobel lecture: When atoms behave as waves: Bose-einstein condensation and the atom laser. *Rev. Mod. Phys.*, 74:1131–1151, Nov 2002.
- [25] Y Sortais, S Bize, M Abgrall, S Zhang, C Nicolas, C Mandache, P Lemonde, P Laurent, G Santarelli, N Dimarcq, P Petit, A Clairon, A Mann, A Luiten, S Chang, and C Salomon. Cold atom clocks. *Physica Scripta*, 2001(T95):50, jan 2001.
- [26] J. Vanier. Atomic clocks based on coherent population trapping: a review. *Applied Physics B*, 81(4):421–442, Aug 2005.

- [27] David R. Scherer, Chad N. Weiler, Tyler W. Neely, and Brian P. Anderson. Vortex formation by merging of multiple trapped bose-einstein condensates. *Phys. Rev. Lett.*, 98:110402, Mar 2007.
- [28] T. W. Neely, E. C. Samson, A. S. Bradley, M. J. Davis, and B. P. Anderson. Observation of vortex dipoles in an oblate bose-einstein condensate. *Phys. Rev. Lett.*, 104:160401, Apr 2010.
- [29] Nathan Goldman, Jean Dalibard, Alexandre Dauphin, Fabrice Gerbier, Maciej Lewenstein, Peter Zoller, and Ian B. Spielman. Direct imaging of topological edge states in cold-atom systems. *Proceedings of the National Academy of Sciences*, 110(17):6736–6741, 2013.
- [30] N. R. Cooper, J. Dalibard, and I. B. Spielman. Topological bands for ultracold atoms. *Rev. Mod. Phys.*, 91:015005, Mar 2019.
- [31] Francesco Tacchino, Alessandro Chiesa, Stefano Carretta, and Dario Gerace. Quantum computers as universal quantum simulators: State-of-the-art and perspectives. *Advanced Quantum Technologies*, 3(3):1900052, 2020.
- [32] M. Saffman, T. G. Walker, and K. Mølmer. Quantum information with rydberg atoms. *Rev. Mod. Phys.*, 82:2313–2363, Aug 2010.
- [33] C S Adams, J D Pritchard, and J P Shaffer. Rydberg atom quantum technologies. *Journal of Physics B: Atomic, Molecular and Optical Physics*, 53(1):012002, dec 2019.
- [34] Kenneth Wang, Conner P. Williams, Lewis R.B. Picard, Norman Y. Yao, and Kang-Kuen Ni. Enriching the quantum toolbox of ultracold molecules with rydberg atoms. *PRX Quantum*, 3:030339, Sep 2022.
- [35] P.W. Shor. Algorithms for quantum computation: discrete logarithms and factoring. In *Proceedings 35th Annual Symposium on Foundations of Computer Science*, pages 124–134, 1994.
- [36] Michael A. Nielsen and Isaac L. Chuang. *Quantum Computation and Quantum Information: 10th Anniversary Edition*. Cambridge University Press, 2010.
- [37] Ashley Montanaro. Quantum algorithms: an overview. *npj Quantum Information*, 2(1):15023, Jan 2016.
- [38] Heinz-Peter Breuer and Francesco Petruccione. *The Theory of Open Quantum Systems*. Oxford University Press, 01 2007.
- [39] Felix Binder, Luis A Correa, Christian Gogolin, Janet Anders, and Gerardo Adesso, editors. *Thermodynamics in the quantum regime*. Fundamental Theories of Physics. Springer International Publishing, Basel, Switzerland, 1 edition, January 2018.
- [40] Sebastian Deffner and Steve Campbell. *Quantum Thermodynamics*. 2053-2571. Morgan & Claypool Publishers, 2019.

- [41] R Alicki. The quantum open system as a model of the heat engine. *Journal of Physics A: Mathematical and General*, 12(5):L103, may 1979.
- [42] Martí Perarnau-Llobet, Elisa Bäumer, Karen V. Hovhannisyanyan, Marcus Huber, and Antonio Acín. No-go theorem for the characterization of work fluctuations in coherent quantum systems. *Phys. Rev. Lett.*, 118:070601, Feb 2017.
- [43] Gabriele De Chiara, Gabriel Landi, Adam Hewgill, Brendan Reid, Alessandro Ferraro, Augusto J Roncaglia, and Mauro Antezza. Reconciliation of quantum local master equations with thermodynamics. *New Journal of Physics*, 20(11):113024, nov 2018.
- [44] Zohreh Davoudi, Christopher Jarzynski, Niklas Mueller, Greeshma Oruganti, Connor Powers, and Nicole Yunger Halpern. Quantum thermodynamics of nonequilibrium processes in lattice gauge theories. *Phys. Rev. Lett.*, 133:250402, Dec 2024.
- [45] A. Einstein, B. Podolsky, and N. Rosen. Can quantum-mechanical description of physical reality be considered complete? *Phys. Rev.*, 47:777–780, May 1935.
- [46] Robert B. Griffiths. The Consistent Histories Approach to Quantum Mechanics. In Edward N. Zalta and Uri Nodelman, editors, *The Stanford Encyclopedia of Philosophy*. Metaphysics Research Lab, Stanford University, Summer 2024 edition, 2024.
- [47] A. J. Leggett. The quantum measurement problem. *Science*, 307(5711):871–872, 2005.
- [48] Maximilian Schlosshauer. Decoherence, the measurement problem, and interpretations of quantum mechanics. *Rev. Mod. Phys.*, 76:1267–1305, Feb 2005.
- [49] Wojciech H. Zurek. Decoherence and the transition from quantum to classical. *Physics Today*, 44(10):36–44, 10 1991.
- [50] Wojciech Hubert Zurek. Decoherence, einselection, and the quantum origins of the classical. *Rev. Mod. Phys.*, 75:715–775, May 2003.
- [51] Anu Venugopalan. Pointer states via decoherence in a quantum measurement. *Phys. Rev. A*, 61:012102, Dec 1999.
- [52] Wojciech Hubert Zurek. Quantum darwinism. *Nature Physics*, 5(3):181–188, Mar 2009.
- [53] Akram Touil, Bin Yan, Davide Girolami, Sebastian Deffner, and Wojciech Hubert Zurek. Eavesdropping on the decohering environment: Quantum darwinism, amplification, and the origin of objective classical reality. *Phys. Rev. Lett.*, 128:010401, Jan 2022.
- [54] Irene Valladares Duque and Philipp Strasberg. Toy model challenging prevailing definitions of classicality, 2024.
- [55] John Bechhoefer. Feedback for physicists: A tutorial essay on control. *Rev. Mod. Phys.*, 77:783–836, Aug 2005.
- [56] Jing Zhang, Yu xi Liu, Re-Bing Wu, Kurt Jacobs, and Franco Nori. Quantum feedback: Theory, experiments, and applications. *Phys. Rep.*, 679:1–60, 2017.

- [57] Debankur Bhattacharyya. *Nonequilibrium Statistical Physics of Feedback-Controlled and Autonomous Information-Thermodynamic Systems*. PhD thesis, University of Maryland, 2024.
- [58] R.P. Feynman, R.B. Leighton, and M. Sands. *The Feynman Lectures on Physics, Vol. I: The New Millennium Edition: Mainly Mechanics, Radiation, and Heat*. Basic Books, 2015.
- [59] Dibyendu Mandal and Christopher Jarzynski. Work and information processing in a solvable model of maxwell’s demon. *Proceedings of the National Academy of Sciences*, 109(29):11641–11645, 2012.
- [60] Debankur Bhattacharyya and Christopher Jarzynski. From a feedback-controlled demon to an information ratchet in a double quantum dot. *Phys. Rev. E*, 106:064101, Dec 2022.
- [61] R. E. Kalman. A new approach to linear filtering and prediction problems. *Journal of Basic Engineering*, 82(1):35–45, 03 1960.
- [62] Andrew Steane. Multiple-particle interference and quantum error correction. *Proceedings of the Royal Society of London A*, 452:2551–2577, 1996.
- [63] Lu-Ming Duan and Guang-Can Guo. Preserving coherence in quantum computation by pairing quantum bits. *Phys. Rev. Lett.*, 79:1953–1956, Sep 1997.
- [64] P. Campagne-Ibarcq, E. Flurin, N. Roch, D. Darson, P. Morfin, M. Mirrahimi, M. H. Devoret, F. Mallet, and B. Huard. Persistent control of a superconducting qubit by stroboscopic measurement feedback. *Phys. Rev. X*, 3:021008, May 2013.
- [65] Toshihiro Yada, Nobuyuki Yoshioka, and Takahiro Sagawa. Quantum fluctuation theorem under quantum jumps with continuous measurement and feedback. *Phys. Rev. Lett.*, 128:170601, Apr 2022.
- [66] Viacheslav P. Belavkin. Nondemolition measurements, nonlinear filtering and dynamic programming of quantum stochastic processes. In Austin Blaquiére, editor, *Modeling and Control of Systems*, pages 245–265, Berlin, Heidelberg, 1989. Springer Berlin Heidelberg.
- [67] V.P. Belavkin. A new wave equation for a continuous nondemolition measurement. *Phys. Lett. A*, 140(7):355–358, 1989.
- [68] Howard M. Wiseman and Gerard J. Milburn. *Quantum Measurement and Control*. Cambridge University Press, 2009.
- [69] Kurt Jacobs and Daniel A. Steck. A straightforward introduction to continuous quantum measurement. *Contemp. Phys.*, 47(5):279–303, 2006.
- [70] John von Neumann. *Mathematical Foundations of Quantum Mechanics*. Princeton University Press, Princeton, 2018.
- [71] J. J. Sakurai and Jim Napolitano. *Modern Quantum Mechanics*. Cambridge University Press, 3 edition, 2020.

- [72] Andrew N. Jordan and Irfan A. Siddiqi. *Weak Measurement*. Cambridge University Press, 2024.
- [73] G. Lindblad. On the generators of quantum dynamical semigroups. *Communications in Mathematical Physics*, 48(2):119–130, Jun 1976.
- [74] Vittorio Gorini, Andrzej Kossakowski, and E. C. G. Sudarshan. Completely positive dynamical semigroups of n-level systems. *Journal of Mathematical Physics*, 17(5):821–825, 05 1976.
- [75] C.W. Gardiner. *Handbook of Stochastic Methods for Physics, Chemistry, and the Natural Sciences*. Proceedings in Life Sciences. Springer-Verlag, Berlin, 1985.
- [76] Bernt K. Øksendal. *Stochastic Differential Equations: An Introduction with Applications*. Universitext. Springer, Berlin, sixth edition, 2003.
- [77] Björn Annby-Andersson. *Continuous measurements of small systems: Feedback control, thermodynamics, entanglement*. PhD thesis, Lund University, 04 2024.
- [78] Holst, Daniel. Continuous Quantum Control of Quantum Dot Systems, 2022. Student Paper.
- [79] Karl Kraus, A. Böhm, J. D. Dollard, and W. H. Wootters. *States and effects*, pages 1–12. Springer Berlin Heidelberg, Berlin, Heidelberg, 1983.
- [80] H. M. Wiseman and G. J. Milburn. Quantum theory of optical feedback via homodyne detection. *Phys. Rev. Lett.*, 70:548–551, Feb 1993.
- [81] A. C. Doherty and K. Jacobs. Feedback control of quantum systems using continuous state estimation. *Phys. Rev. A*, 60:2700–2711, Oct 1999.
- [82] Asa Hopkins, Kurt Jacobs, Salman Habib, and Keith Schwab. Feedback cooling of a nanomechanical resonator. *Phys. Rev. B*, 68:235328, Dec 2003.
- [83] Kurt Jacobs, Hendra I. Nurdin, Frederick W. Strauch, and Matthew James. Comparing resolved-sideband cooling and measurement-based feedback cooling on an equal footing: Analytical results in the regime of ground-state cooling. *Phys. Rev. A*, 91:043812, Apr 2015.
- [84] E. Arthurs and J. L. Kelly. B.s.t.j. briefs: On the simultaneous measurement of a pair of conjugate observables. *The Bell System Technical Journal*, 44(4):725–729, 1965.
- [85] Walther Gerlach and Otto Stern. Der experimentelle nachweis der richtungsquantelung im magnetfeld. *Zeitschrift für Physik*, 9(1):349–352, Dec 1922.
- [86] A Barchielli and V P Belavkin. Measurements continuous in time and a posteriori states in quantum mechanics. *J. Phys. A*, 24(7):1495, apr 1991.
- [87] Viacheslav P Belavkin. Quantum stochastic calculus and quantum nonlinear filtering. *J. Multivar. Anal.*, 42(2):171–201, 1992.

- [88] Jacek Dziarmaga, Diego A. R. Dalvit, and Wojciech H. Zurek. Conditional quantum dynamics with several observers. *Phys. Rev. A*, 69:022109, Feb 2004.
- [89] Philipp Strasberg, Gernot Schaller, Tobias Brandes, and Massimiliano Esposito. Quantum and information thermodynamics: A unifying framework based on repeated interactions. *Phys. Rev. X*, 7:021003, Apr 2017.
- [90] Steve Campbell and Bassano Vacchini. Collision models in open system dynamics: A versatile tool for deeper insights? *Europhysics Letters*, 133(6):60001, may 2021.
- [91] Gabriel T. Landi, Mauro Paternostro, and Alessio Belenchia. Informational steady states and conditional entropy production in continuously monitored systems. *PRX Quantum*, 3:010303, Jan 2022.
- [92] Francesco Ciccarello, Salvatore Lorenzo, Vittorio Giovannetti, and G. Massimo Palma. Quantum collision models: Open system dynamics from repeated interactions. *Physics Reports*, 954:1–70, 2022. Quantum collision models: Open system dynamics from repeated interactions.
- [93] Fernando Casas, Ander Murua, and Mladen Nadinic. Efficient computation of the zassenhaus formula. *Computer Physics Communications*, 183(11):2386–2391, 2012.
- [94] H. Häffner, C.F. Roos, and R. Blatt. Quantum computing with trapped ions. *Phys. Rep.*, 469(4):155–203, 2008.
- [95] M. H. Devoret and R. J. Schoelkopf. Superconducting circuits for quantum information: An outlook. *Science*, 339(6124):1169–1174, 2013.
- [96] C. L. Degen, F. Reinhard, and P. Cappellaro. Quantum sensing. *Rev. Mod. Phys.*, 89:035002, Jul 2017.
- [97] S. Pirandola, B. R. Bardhan, T. Gehring, C. Weedbrook, and S. Lloyd. Advances in photonic quantum sensing. *Nat. Photon.*, 12(12):724–733, Dec 2018.
- [98] William D. Phillips, Phillip L. Gould, and Paul D. Lett. Cooling, stopping, and trapping atoms. *Science*, 239(4842):877–883, 1988.
- [99] Claude N. Cohen-Tannoudji and William D. Phillips. New mechanisms for laser cooling. *Phys. Today*, 43(10):33–40, 1990.
- [100] Steven Chu. Laser manipulation of atoms and particles. *Science*, 253(5022):861–866, 1991.
- [101] Kendall B. Davis, Marc-Oliver Mewes, Michael A. Joffe, Michael R. Andrews, and Wolfgang Ketterle. Evaporative cooling of sodium atoms. *Phys. Rev. Lett.*, 74:5202–5205, Jun 1995.
- [102] K. B. Davis, M.-O. Mewes, and W. Ketterle. An analytical model for evaporative cooling of atoms. *Appl. Phys. B*, 60(2):155–159, Feb 1995.

- [103] Wolfgang Ketterle and N.J. Van Druten. *Evaporative Cooling of Trapped Atoms*, volume 37, pages 181–236. Academic Press, San Diego, Jan 1996.
- [104] Chen-Lung Hung, Xibo Zhang, Nathan Gemelke, and Cheng Chin. Accelerating evaporative cooling of atoms into bose-einstein condensation in optical traps. *Phys. Rev. A*, 78:011604, Jul 2008.
- [105] P. Maunz, T. Puppe, I. Schuster, N. Syassen, P. W. H. Pinkse, and G. Rempe. Cavity cooling of a single atom. *Nature*, 428(6978):50–52, Mar 2004.
- [106] Nikolai Kiesel, Florian Blaser, Uroš Delić, David Grass, Rainer Kaltenbaek, and Markus Aspelmeyer. Cavity cooling of an optically levitated submicron particle. *Proc. Natl. Acad. Sci. USA*, 110(35):14180–14185, 2013.
- [107] Mahdi Hosseini, Yiheng Duan, Kristin M. Beck, Yu-Ting Chen, and Vladan Vuletić. Cavity cooling of many atoms. *Phys. Rev. Lett.*, 118:183601, May 2017.
- [108] B. D’Urso, B. Odom, and G. Gabrielse. Feedback cooling of a one-electron oscillator. *Phys. Rev. Lett.*, 90:043001, Jan 2003.
- [109] Pavel Bushev, Daniel Rotter, Alex Wilson, François Dubin, Christoph Becher, Jürgen Eschner, Rainer Blatt, Viktor Steixner, Peter Rabl, and Peter Zoller. Feedback cooling of a single trapped ion. *Phys. Rev. Lett.*, 96:043003, Feb 2006.
- [110] Clemens Schäfermeier, Hugo Kerdoncuff, Ulrich B. Hoff, Hao Fu, Alexander Huck, Jan Bilek, Glen I. Harris, Warwick P. Bowen, Tobias Gehring, and Ulrik L. Andersen. Quantum enhanced feedback cooling of a mechanical oscillator using nonclassical light. *Nat. Commun.*, 7(1):13628, Nov 2016.
- [111] Hojat Habibi, Emil Zeuthen, Majid Ghanaatshoar, and Klemens Hammerer. Quantum feedback cooling of a mechanical oscillator using variational measurements: tweaking heisenberg’s microscope. *Journal of Optics*, 18(8):084004, jul 2016.
- [112] Jingkun Guo, Richard Norte, and Simon Gröblacher. Feedback cooling of a room temperature mechanical oscillator close to its motional ground state. *Phys. Rev. Lett.*, 123:223602, Nov 2019.
- [113] Lorenzo Buffoni, Andrea Solfanelli, Paola Verrucchi, Alessandro Cuccoli, and Michele Campisi. Quantum measurement cooling. *Phys. Rev. Lett.*, 122:070603, Feb 2019.
- [114] Martin Frimmer, Jan Gieseler, and Lukas Novotny. Cooling mechanical oscillators by coherent control. *Phys. Rev. Lett.*, 117:163601, Oct 2016.
- [115] Sreenath K. Manikandan and Sofia Qvarfort. Optimal quantum parametric feedback cooling. *Phys. Rev. A*, 107:023516, Feb 2023.
- [116] Daniel A. Steck, Kurt Jacobs, Hideo Mabuchi, Salman Habib, and Tanmoy Bhattacharya. Feedback cooling of atomic motion in cavity qed. *Phys. Rev. A*, 74:012322, Jul 2006.

- [117] Jan Gieseler, Bradley Deutsch, Romain Quidant, and Lukas Novotny. Subkelvin parametric feedback cooling of a laser-trapped nanoparticle. *Phys. Rev. Lett.*, 109:103603, Sep 2012.
- [118] Jing Zhang, Yu-xi Liu, and Franco Nori. Cooling and squeezing the fluctuations of a nanomechanical beam by indirect quantum feedback control. *Phys. Rev. A*, 79:052102, May 2009.
- [119] Philip Taranto, Patryk Lipka-Bartosik, Nayeli A. Rodríguez-Briones, Martí Perarnau-Llobet, Nicolai Friis, Marcus Huber, and Pharnam Bakhshinezhad. Efficiently cooling quantum systems with finite resources: Insights from thermodynamic geometry, 2024. arXiv:2404.06649 [quant-ph].
- [120] Philip Taranto, Faraj Bakhshinezhad, Andreas Bluhm, Ralph Silva, Nicolai Friis, Maximilian P. E. Lock, Giuseppe Vitagliano, Felix C. Binder, Tiago Debarba, Emanuel Schwarzthans, Fabien Clivaz, and Marcus Huber. Landauer vs. nernst: What is the true cost of cooling a quantum system?, 2021. arXiv:2106.05151 [quant-ph].
- [121] Philip Taranto, Faraj Bakhshinezhad, Philipp Schüttelkopf, Fabien Clivaz, and Marcus Huber. Exponential improvement for quantum cooling through finite-memory effects. *Phys. Rev. Appl.*, 14:054005, Nov 2020.
- [122] Nahuel Freitas, Rodrigo Gallego, Lluís Masanes, and Juan Pablo Paz. *Cooling to Absolute Zero: The Unattainability Principle*, pages 597–622. Springer International Publishing, Cham, 2018.
- [123] Carlton M. Caves and G. J. Milburn. Quantum-mechanical model for continuous position measurements. *Phys. Rev. A*, 36:5543–5555, Dec 1987.
- [124] L. Diósi. Continuous quantum measurement and itô formalism. *Phys. Lett. A*, 129(8):419–423, 1988.
- [125] S Dyrting and G J Milburn. Quantum chaos in atom optics: using phase noise to model continuous momentum and position measurement. *Quantum and Semiclassical Optics: Journal of the European Optical Society Part B*, 8(3):541–555, jun 1996.
- [126] Andrew C. Doherty, Salman Habib, Kurt Jacobs, Hideo Mabuchi, and Sze M. Tan. Quantum feedback control and classical control theory. *Phys. Rev. A*, 62:012105, Jun 2000.
- [127] JM Geremia, John K. Stockton, and Hideo Mabuchi. Real-time quantum feedback control of atomic spin-squeezing. *Science*, 304(5668):270–273, 2004.
- [128] T. A. Wheatley, D. W. Berry, H. Yonezawa, D. Nakane, H. Arao, D. T. Pope, T. C. Ralph, H. M. Wiseman, A. Furusawa, and E. H. Huntington. Adaptive optical phase estimation using time-symmetric quantum smoothing. *Phys. Rev. Lett.*, 104:093601, Mar 2010.
- [129] Hidehiro Yonezawa, Daisuke Nakane, Trevor A. Wheatley, Kohjiro Iwasawa, Shuntaro Takeda, Hajime Arao, Kentaro Ohki, Koji Tsumura, Dominic W. Berry, Timothy C. Ralph, Howard M. Wiseman, Elanor H. Huntington, and Akira Furusawa. Quantum-enhanced optical-phase tracking. *Science*, 337(6101):1514–1517, 2012.

- [130] Z. K. Mineev, S. O. Mundhada, S. Shankar, P. Reinhold, R. Gutiérrez-Jáuregui, R. J. Schoelkopf, M. Mirrahimi, H. J. Carmichael, and M. H. Devoret. To catch and reverse a quantum jump mid-flight. *Nature*, 570(7760):200–204, Jun 2019.
- [131] Tathagata Karmakar, Philippe Lewalle, and Andrew N. Jordan. Stochastic path-integral analysis of the continuously monitored quantum harmonic oscillator. *PRX Quantum*, 3:010327, Feb 2022.
- [132] Giovanna Morigi, Jürgen Eschner, and Christoph H. Keitel. Ground state laser cooling using electromagnetically induced transparency. *Phys. Rev. Lett.*, 85:4458–4461, Nov 2000.
- [133] I. Wilson-Rae, P. Zoller, and A. Imamoglu. Laser cooling of a nanomechanical resonator mode to its quantum ground state. *Phys. Rev. Lett.*, 92:075507, Feb 2004.
- [134] Yong Li, Lian-Ao Wu, and Z. D. Wang. Fast ground-state cooling of mechanical resonators with time-dependent optical cavities. *Phys. Rev. A*, 83:043804, Apr 2011.
- [135] J. D. Teufel, T. Donner, Dale Li, J. W. Harlow, M. S. Allman, K. Cicak, A. J. Sirois, J. D. Whittaker, K. W. Lehnert, and R. W. Simmonds. Sideband cooling of micromechanical motion to the quantum ground state. *Nature*, 475(7356):359–363, Jul 2011.
- [136] Jasper Chan, T. P. Mayer Alegre, Amir H. Safavi-Naeini, Jeff T. Hill, Alex Krause, Simon Gröblacher, Markus Aspelmeyer, and Oskar Painter. Laser cooling of a nanomechanical oscillator into its quantum ground state. *Nature*, 478(7367):89–92, Oct 2011.
- [137] A. M. Kaufman, B. J. Lester, and C. A. Regal. Cooling a single atom in an optical tweezer to its quantum ground state. *Phys. Rev. X*, 2:041014, Nov 2012.
- [138] Wei Zeng, Wenjie Nie, Ling Li, and Aixi Chen. Ground-state cooling of a mechanical oscillator in a hybrid optomechanical system including an atomic ensemble. *Sci. Rep.*, 7(1):17258, Dec 2017.
- [139] Uroš Delić, Manuel Reisenbauer, Kahan Dare, David Grass, Vladan Vuletić, Nikolai Kiesel, and Markus Aspelmeyer. Cooling of a levitated nanoparticle to the motional quantum ground state. *Science*, 367(6480):892–895, 2020.
- [140] S. Machnes, J. Cerrillo, M. Aspelmeyer, W. Wieczorek, M. B. Plenio, and A. Retzker. Pulsed laser cooling for cavity optomechanical resonators. *Phys. Rev. Lett.*, 108:153601, Apr 2012.
- [141] S. D. Wilson, A. R. R. Carvalho, J. J. Hope, and M. R. James. Effects of measurement backaction in the stabilization of a bose-einstein condensate through feedback. *Phys. Rev. A*, 76:013610, Jul 2007.
- [142] Sreenath K. Manikandan, Cyril Elouard, Kater W. Murch, Alexia Auffèves, and Andrew N. Jordan. Efficiently fueling a quantum engine with incompatible measurements. *Phys. Rev. E*, 105:044137, Apr 2022.

- [143] Amy Rouillard, Anirudh Reddy, Humairah Bassa, Shamik Maharaj, Lajos Diosi, and Thomas Konrad. Measurement-based feedback control of a quantum system in a harmonic potential, 2022. arXiv:2212.12292 [quant-ph].
- [144] Andrew C. Doherty, A. Szorkovszky, G. I. Harris, and W. P. Bowen. The quantum trajectory approach to quantum feedback control of an oscillator revisited. *Philos. Trans. R. Soc. London, Ser. A*, 370(1979):5338–5353, 2012.
- [145] J.-M. Courty, A. Heidmann, and M. Pinard. Quantum limits of cold damping with optomechanical coupling. *Eur. Phys. J. D*, 17(3):399–408, Dec 2001.
- [146] P. F. Cohadon, A. Heidmann, and M. Pinard. Cooling of a mirror by radiation pressure. *Phys. Rev. Lett.*, 83:3174–3177, Oct 1999.
- [147] Felix Tebbenjohanns, Martin Frimmer, Andrei Militaru, Vijay Jain, and Lukas Novotny. Cold damping of an optically levitated nanoparticle to microkelvin temperatures. *Phys. Rev. Lett.*, 122:223601, Jun 2019.
- [148] M. Poggio, C. L. Degen, H. J. Mamin, and D. Rugar. Feedback cooling of a cantilever’s fundamental mode below 5 mk. *Phys. Rev. Lett.*, 99:017201, Jul 2007.
- [149] C. Genes, D. Vitali, P. Tombesi, S. Gigan, and M. Aspelmeyer. Ground-state cooling of a micromechanical oscillator: Comparing cold damping and cavity-assisted cooling schemes. *Phys. Rev. A*, 77:033804, Mar 2008.
- [150] D. J. Wilson, V. Sudhir, N. Piro, R. Schilling, A. Ghadimi, and T. J. Kippenberg. Measurement-based control of a mechanical oscillator at its thermal decoherence rate. *Nature*, 524(7565):325–329, Aug 2015.
- [151] V. Steixner, P. Rabl, and P. Zoller. Quantum feedback cooling of a single trapped ion in front of a mirror. *Phys. Rev. A*, 72:043826, Oct 2005.
- [152] Jordan M. Horowitz. Quantum-trajectory approach to the stochastic thermodynamics of a forced harmonic oscillator. *Phys. Rev. E*, 85:031110, Mar 2012.
- [153] Luca Magazzù, Peter Talkner, and Peter Hänggi. Quantum brownian motion under generalized position measurements: a converse zeno scenario. *New Journal of Physics*, 20(3):033001, mar 2018.
- [154] Sabrina Maniscalco, Jyrki Piilo, and Kalle-Antti Suominen. Zeno and anti-zeno effects for quantum brownian motion. *Phys. Rev. Lett.*, 97:130402, Sep 2006.
- [155] Feng Tang and Nan Zhao. Quantum noise of a harmonic oscillator under classical feedback control*. *Chinese Physics B*, 29(9):090303, aug 2020.
- [156] H. M. Wiseman and G. J. Milburn. Squeezing via feedback. *Phys. Rev. A*, 49:1350–1366, Feb 1994.
- [157] Ryan Hamerly and Hideo Mabuchi. Advantages of coherent feedback for cooling quantum oscillators. *Phys. Rev. Lett.*, 109:173602, Oct 2012.

- [158] Lajos Diósi. Hybrid quantum-classical master equations. *Physica Scripta*, 2014(T163):014004, dec 2014.
- [159] Lajos Diósi. Hybrid completely positive markovian quantum-classical dynamics. *Phys. Rev. A*, 107:062206, Jun 2023.
- [160] K. Jacobs and P. L. Knight. Linear quantum trajectories: Applications to continuous projection measurements. *Phys. Rev. A*, 57:2301–2310, Apr 1998.
- [161] Seth Lloyd. Coherent quantum feedback. *Phys. Rev. A*, 62:022108, Jul 2000.
- [162] Clément Sayrin, Igor Dotsenko, Xingxing Zhou, Bruno Peaudecerf, Théo Rybarczyk, Sébastien Gleyzes, Pierre Rouchon, Mazyar Mirrahimi, Hadis Amini, Michel Brune, Jean-Michel Raimond, and Serge Haroche. Real-time quantum feedback prepares and stabilizes photon number states. *Nature*, 477(7362):73–77, Sep 2011.
- [163] David J. Wineland. Nobel lecture: Superposition, entanglement, and raising schrödinger’s cat. *Rev. Mod. Phys.*, 85:1103–1114, Jul 2013.
- [164] H. J. Metcalf and P. van der Straten. Laser cooling and trapping of atoms. *J. Opt. Soc. Am. B*, 20(5):887–908, May 2003.
- [165] D. Barker, S. Lehmann, L. Namazi, M. Nilsson, C. Thelander, K. A. Dick, and V. F. Maisi. Individually addressable double quantum dots formed with nanowire polytypes and identified by epitaxial markers. *Applied Physics Letters*, 114(18):183502, 05 2019.
- [166] S. Gustavsson, R. Leturcq, B. Simovič, R. Schleser, T. Ihn, P. Studerus, K. Ensslin, D. C. Driscoll, and A. C. Gossard. Counting statistics of single electron transport in a quantum dot. *Phys. Rev. Lett.*, 96:076605, Feb 2006.
- [167] Robert H. Hadfield. Single-photon detectors for optical quantum information applications. *Nature Photonics*, 3(12):696–705, Dec 2009.
- [168] I. Charaev, D. A. Bandurin, A. T. Bollinger, I. Y. Phinney, I. Drozdov, M. Colangelo, B. A. Butters, T. Taniguchi, K. Watanabe, X. He, O. Medeiros, I. Božović, P. Jarillo-Herrero, and K. K. Berggren. Single-photon detection using high-temperature superconductors. *Nature Nanotechnology*, 18(4):343–349, Apr 2023.
- [169] F. Jelezko and J. Wrachtrup. Single defect centres in diamond: A review. *physica status solidi (a)*, 203(13):3207–3225, 2006.
- [170] Nabeel Aslam, Hengyun Zhou, Elana K. Urbach, Matthew J. Turner, Ronald L. Walsworth, Mikhail D. Lukin, and Hongkun Park. Quantum sensors for biomedical applications. *Nature Reviews Physics*, 5(3):157–169, Mar 2023.
- [171] Charlene Ahn, Andrew C. Doherty, and Andrew J. Landahl. Continuous quantum error correction via quantum feedback control. *Phys. Rev. A*, 65:042301, Mar 2002.

- [172] P. Scarlino, J. H. Ungerer, D. J. van Woerkom, M. Mancini, P. Stano, C. Müller, A. J. Landig, J. V. Koski, C. Reichl, W. Wegscheider, T. Ihn, K. Ensslin, and A. Wallraff. In situ tuning of the electric-dipole strength of a double-dot charge qubit: Charge-noise protection and ultrastrong coupling. *Phys. Rev. X*, 12:031004, Jul 2022.
- [173] H. J. Briegel, D. E. Browne, W. Dür, R. Raussendorf, and M. Van den Nest. Measurement-based quantum computation. *Nature Physics*, 5(1):19–26, Jan 2009.
- [174] Sourabh Lahiri, Shubhashis Rana, and A M Jayannavar. Fluctuation theorems in the presence of information gain and feedback. *Journal of Physics A: Mathematical and Theoretical*, 45(6):065002, jan 2012.
- [175] Björn Annby-Andersson, Peter Samuelsson, Ville F. Maisi, and Patrick P. Potts. Maxwell’s demon in a double quantum dot with continuous charge detection. *Phys. Rev. B*, 101:165404, Apr 2020.
- [176] Kacper Prech and Patrick P. Potts. Quantum fluctuation theorem for arbitrary measurement and feedback schemes. *Phys. Rev. Lett.*, 133:140401, Oct 2024.
- [177] Fernando G. S. L. Brandão, Michał Horodecki, Jonathan Oppenheim, Joseph M. Renes, and Robert W. Spekkens. Resource theory of quantum states out of thermal equilibrium. *Phys. Rev. Lett.*, 111:250404, Dec 2013.
- [178] Carlo Sparaciari, Jonathan Oppenheim, and Tobias Fritz. Resource theory for work and heat. *Phys. Rev. A*, 96:052112, Nov 2017.
- [179] Philipp Strasberg and Andreas Winter. First and second law of quantum thermodynamics: A consistent derivation based on a microscopic definition of entropy. *PRX Quantum*, 2:030202, Aug 2021.
- [180] Chaitanya Murthy, Arman Babakhani, Fernando Iniguez, Mark Srednicki, and Nicole Yunger Halpern. Non-abelian eigenstate thermalization hypothesis. *Phys. Rev. Lett.*, 130:140402, Apr 2023.
- [181] Paul Skrzypczyk, Anthony J. Short, and Sandu Popescu. Work extraction and thermodynamics for individual quantum systems. *Nature Communications*, 5(1):4185, Jun 2014.
- [182] Cyril Elouard, David Herrera-Martí, Benjamin Huard, and Alexia Auffèves. Extracting work from quantum measurement in maxwell’s demon engines. *Phys. Rev. Lett.*, 118:260603, Jun 2017.
- [183] Gonzalo Manzano, Francesco Plastina, and Roberta Zambrini. Optimal work extraction and thermodynamics of quantum measurements and correlations. *Phys. Rev. Lett.*, 121:120602, Sep 2018.
- [184] Jennifer Koch, Keerthy Menon, Eloisa Cuestas, Sian Barbosa, Eric Lutz, Thomás Fogarty, Thomas Busch, and Artur Widera. A quantum engine in the bec–bcs crossover. *Nature*, 621(7980):723–727, Sep 2023.

- [185] Maron F. Anka, Thiago R. de Oliveira, and Daniel Jonathan. Work and efficiency fluctuations in a quantum otto cycle with idle levels. *Phys. Rev. E*, 109:064129, Jun 2024.
- [186] Arne L. Grimsmo. Time-delayed quantum feedback control. *Phys. Rev. Lett.*, 115:060402, Aug 2015.
- [187] M. Hirose and P. Cappellaro. Time-optimal control with finite bandwidth. *Quantum Information Processing*, 17(4):88, Feb 2018.
- [188] Kseniia Vodenkova and Hannes Pichler. Continuous coherent quantum feedback with time delays: Tensor network solution. *Phys. Rev. X*, 14:031043, Sep 2024.
- [189] Peter Siegle, Igor Goychuk, Peter Talkner, and Peter Hänggi. Markovian embedding of non-markovian superdiffusion. *Phys. Rev. E*, 81:011136, Jan 2010.
- [190] Steve Campbell, Francesco Ciccarello, G. Massimo Palma, and Bassano Vacchini. System-environment correlations and markovian embedding of quantum non-markovian dynamics. *Phys. Rev. A*, 98:012142, Jul 2018.
- [191] Xiantao Li. Markovian embedding procedures for non-markovian stochastic schrödinger equations. *Physics Letters A*, 387:127036, 2021.
- [192] Hendra I. Nurdin. Markovian embeddings of non-markovian quantum systems: Coupled stochastic and quantum master equations for non-markovian quantum systems. In *2023 62nd IEEE Conference on Decision and Control (CDC)*, pages 5939–5944, 2023.
- [193] Ferenc Krausz. Nobel lecture: Sub-atomic motions. *Rev. Mod. Phys.*, 96:030502, Aug 2024.
- [194] Anne L’Huillier. Nobel lecture: The route to attosecond pulses. *Rev. Mod. Phys.*, 96:030503, Aug 2024.
- [195] Stig Stenholm. The semiclassical theory of laser cooling. *Rev. Mod. Phys.*, 58:699–739, Jul 1986.
- [196] P. D. Lett, W. D. Phillips, S. L. Rolston, C. E. Tanner, R. N. Watts, and C. I. Westbrook. Optical molasses. *J. Opt. Soc. Am. B*, 6(11):2084–2107, Nov 1989.
- [197] Mariusz Gajda and Jan Mostowski. Three-dimensional theory of the magneto-optical trap: Doppler cooling in the low-intensity limit. *Phys. Rev. A*, 49:4864–4875, Jun 1994.
- [198] K Molmer. The optimum fokker-planck equation for laser cooling. *Journal of Physics B: Atomic, Molecular and Optical Physics*, 27(9):1889, may 1994.
- [199] Y. Castin, H. Wallis, and J. Dalibard. Limit of doppler cooling. *J. Opt. Soc. Am. B*, 6(11):2046–2057, Nov 1989.
- [200] V.S. Letokhov, V.G. Minogin, and B.D. Pavlik. Cooling and trapping of atoms and molecules by a resonant laser field. *Optics Communications*, 19(1):72–75, 1976.

- [201] William D. Phillips and John V. Prodanf. Cooling atoms with a frequency chirped laser. In Leonard Mandel and Emil Wolf, editors, *Coherence and Quantum Optics V*, pages 15–22, Boston, MA, 1984. Springer US.
- [202] William D. Phillips and Harold Metcalf. Laser deceleration of an atomic beam. *Phys. Rev. Lett.*, 48:596–599, Mar 1982.
- [203] John V. Prodan, William D. Phillips, and Harold Metcalf. Laser production of a very slow monoenergetic atomic beam. *Phys. Rev. Lett.*, 49:1149–1153, Oct 1982.
- [204] William D. Phillips, John V. Prodan, and Harold J. Metcalf. Laser cooling and electromagnetic trapping of neutral atoms. *J. Opt. Soc. Am. B*, 2(11):1751–1767, Nov 1985.
- [205] W. Ertmer, R. Blatt, J. L. Hall, and M. Zhu. Laser manipulation of atomic beam velocities: Demonstration of stopped atoms and velocity reversal. *Phys. Rev. Lett.*, 54:996–999, Mar 1985.
- [206] Steven Chu, L. Hollberg, J. E. Bjorkholm, Alex Cable, and A. Ashkin. Three-dimensional viscous confinement and cooling of atoms by resonance radiation pressure. *Phys. Rev. Lett.*, 55:48–51, Jul 1985.
- [207] D. E. Pritchard, E. L. Raab, V. Bagnato, C. E. Wieman, and R. N. Watts. Light traps using spontaneous forces. *Phys. Rev. Lett.*, 57:310–313, Jul 1986.
- [208] E. L. Raab, M. Prentiss, Alex Cable, Steven Chu, and D. E. Pritchard. Trapping of neutral sodium atoms with radiation pressure. *Phys. Rev. Lett.*, 59:2631–2634, Dec 1987.
- [209] Paul D. Lett, Richard N. Watts, Christoph I. Westbrook, William D. Phillips, Phillip L. Gould, and Harold J. Metcalf. Observation of atoms laser cooled below the doppler limit. *Phys. Rev. Lett.*, 61:169–172, Jul 1988.
- [210] J. Dalibard and C. Cohen-Tannoudji. Laser cooling below the doppler limit by polarization gradients: simple theoretical models. *J. Opt. Soc. Am. B*, 6(11):2023–2045, Nov 1989.
- [211] P. J. Ungar, D. S. Weiss, E. Riis, and Steven Chu. Optical molasses and multilevel atoms: theory. *J. Opt. Soc. Am. B*, 6(11):2058–2071, Nov 1989.
- [212] C. Salomon, J. Dalibard, W. D. Phillips, A. Clairon, and S. Guellati. Laser cooling of cesium atoms below 3 μk . *Europhysics Letters*, 12(8):683, aug 1990.
- [213] A. M. Turing. On computable numbers, with an application to the entscheidungsproblem. *Proceedings of the London Mathematical Society*, s2-42(1):230–265, 1937.
- [214] Warren S. McCulloch and Walter Pitts. A logical calculus of the ideas immanent in nervous activity. *The bulletin of mathematical biophysics*, 5(4):115–133, Dec 1943.
- [215] Frank Rosenblatt. The perceptron: a probabilistic model for information storage and organization in the brain. *Psychological review*, 65(6):386, 1958.

- [216] G. Cybenko. Approximation by superpositions of a sigmoidal function. *Mathematics of Control, Signals and Systems*, 2(4):303–314, Dec 1989.
- [217] Kurt Hornik, Maxwell Stinchcombe, and Halbert White. Multilayer feedforward networks are universal approximators. *Neural Networks*, 2(5):359–366, 1989.
- [218] J J Hopfield. Neural networks and physical systems with emergent collective computational abilities. *Proceedings of the National Academy of Sciences*, 79(8):2554–2558, 1982.
- [219] Giuseppe Carleo, Ignacio Cirac, Kyle Cranmer, Laurent Daudet, Maria Schuld, Naftali Tishby, Leslie Vogt-Maranto, and Lenka Zdeborová. Machine learning and the physical sciences. *Rev. Mod. Phys.*, 91:045002, Dec 2019.
- [220] Justyna P. Zwolak and Jacob M. Taylor. Colloquium: Advances in automation of quantum dot devices control. *Rev. Mod. Phys.*, 95:011006, February 2023.
- [221] Lia Medeiros, Dimitrios Psaltis, Tod R. Lauer, and Feryal Özel. The image of the m87 black hole reconstructed with primo. *The Astrophysical Journal Letters*, 947(1):L7, apr 2023.
- [222] Ippei Nakamura, Atsunori Kanemura, Takumi Nakaso, Ryuta Yamamoto, and Takeshi Fukuhara. Non-standard trajectories found by machine learning for evaporative cooling of 87rb atoms. *Opt. Express*, 27(15):20435–20443, Jul 2019.
- [223] Harold J. Metcalf and Peter van der Straten. *Laser Cooling and Trapping*. Springer-Verlag, New York, 1999.
- [224] *NIST Digital Library of Mathematical Functions*. <https://dlmf.nist.gov/>, Release 1.2.2 of 2024-09-15. F. W. J. Olver, A. B. Olde Daalhuis, D. W. Lozier, B. I. Schneider, R. F. Boisvert, C. W. Clark, B. R. Miller, B. V. Saunders, H. S. Cohl, and M. A. McClain, eds.
- [225] T. B. Smith, D. A. Herman, A. D. Gallimore, and R. P. Drake. Deconvolution of axial velocity distributions from hall thruster lif spectra. In *27th International Electric Propulsion Conference*, Pasadena, CA, October 15–19 2001. IEPC-01-019.
- [226] I. Yavin, M. Weel, A. Andreyuk, and A. Kumarakrishnan. A calculation of the time-of-flight distribution of trapped atoms. *American Journal of Physics*, 70(2):149–152, 02 2002.
- [227] T. B. Smith. *Deconvolution of Ion Velocity Distributions from Laser-Induced Fluorescence Spectra of Xenon Electrostatic Thruster Plumes*. Ph.d. dissertation, University of Michigan, 2003.
- [228] Norbert Wiener. *Extrapolation, interpolation, and smoothing of stationary time series*. The MIT Press. MIT Press, London, England, March 1964.

- [229] Rafael C Gonzalez, Richard Woods, and Steven L Eddins. *Digital Image Processing Using MATLAB (R)*. Pearson, Upper Saddle River, NJ, December 2003.
- [230] G. Reinaudi, T. Lahaye, Z. Wang, and D. Guéry-Odelin. Strong saturation absorption imaging of dense clouds of ultracold atoms. *Opt. Lett.*, 32(21):3143–3145, Nov 2007.
- [231] Klaus Hueck, Niclas Luick, Lennart Sobirey, Jonas Siegl, Thomas Lompe, Henning Moritz, Logan W. Clark, and Cheng Chin. Calibrating high intensity absorption imaging of ultracold atoms. *Opt. Express*, 25(8):8670–8679, Apr 2017.
- [232] Tadas Baltrušaitis, Chaitanya Ahuja, and Louis-Philippe Morency. Multimodal machine learning: A survey and taxonomy. *IEEE Transactions on Pattern Analysis and Machine Intelligence*, 41(2):423–443, 2019.
- [233] Diederik P. Kingma and Jimmy Ba. Adam: A method for stochastic optimization, 2017.